Alma Mater Studiorum - Università di Bologna

SCUOLA DI SCIENZE
Dipartimento di Chimica Industriale“Toso Montanari”

Corso di Laurea Magistrale in
Chimica Industriale
Classe LM-71 - Scienze e Tecnologie della Chimica Industriale

Accelerated ageing methodologies for the evaluation of particulate matter role in the corrosion of outdoor-exposed bronzes

Tesi di laurea sperimentale

CANDIDATO

Irene Vettori

RELATORE

Chiar.mo Dr. Elena Bernardi

CORRELATORE

Prof. Ivano Vassura

Dr. Francesca Ospitali

Anno Accademico 2017-2018

University of Bologna

Faculty of Science

Industrial Chemistry Department

Funded by the Erasmus+ Programme of the European Union

Erasmus Mundus Joint Master Degree "Advanced Spectroscopy in Chemistry"

MASTER THESIS

by

Irene Vettori

20/07/2018

Accelerated ageing methodologies for the evaluation of particulate matter role in the corrosion of outdoor-exposed bronzes

Research group: Environmental Chemistry and Cultural Heritage

Supervisor(s): Dr. Elena Bernardi

Reviewer(s): Prof. Reinhard Denecke

KEYWORDS:

Particulate Matter, Cultural Heritage Deterioration, Artificial Ageing, Climatic chamber, Corrosion Patinas

ABSTRACT:

Deterioration phenomena occurring on outdoor cultural heritage have been the subject of several studies, but relatively few works investigated the specific role of Particulate Matter (PM) in the corrosion of metals. This topic is really complex and, beside field exposures, accelerated ageing tests are also necessary to isolate and understand deterioration mechanisms due to PM. For this reason, the development of a methodology that allows to reproduce and analyze the effect of PM on alloys through accelerated ageing in climatic chamber has been started. On quaternary bronze specimens, single salts and a mix of them were deposited via two deposition methods: dry (directly depositing the salt on the surface) and wet (dropping a salt solution and drying it), simulating the initial chemical activation of the salts by RH% variations or by raindrops, respectively. Then, to better mimic the composition of real PM, a mixture containing a soluble salts, a mineral, a black carbon and an organic fraction was formulated and spread on the samples. The samples were placed in a climatic chamber and exposed to cyclic variations of T and RH for three weeks. The ageing cycles were set according to predictions on salt deliquescence/recrystallization through E-AIM model and to the evaluation of regional climatic data. The surface evolution was followed by SEM-EDX, Raman, AT-IR and UV-Vis Spectrophotometry. At the end of the test, mass losses were determined and corroded metals removed by pickling were analyzed by AAS. On the basis of the obtained results, the tested procedures seem to be promising in accelerating and mimicking realistic corrosion phenomena, as under the selected conditions, corrosion products typically found at different exposure time (from days to years) on outdoor bronzes were able to progressively form and evolve. Moreover, the two deposition modes simulating different condition of chemical activation of PM deposits allow to obtain complementary information.

CONTENTS

“The purpose of art is washing the dust
of daily life off our souls”.
Pablo Picasso

1 Introduction

The preservation and the conservation of cultural heritage is an internationally recognised issue, which has to deal with deterioration phenomena affecting different materials and promoted by several, intercrossed factors. Among the variety of topics that can be investigated in this field, the corrosion of metallic manufacts is of primary importance for the high reactivity of those substrates against the chemical substances in the environment and for the irreversibility of the corrosion processes once deterioration patinas are formed [1]. In the case of outdoor-exposed manufacts, as for the Mermaid in Copenaghen shown in Fig. 1.1.1, the corrosion rate is particularly enhanced because the manufact is submitted to uncontrolled environmental conditions, that lead to many more physico-chemical changements than indoor-exposed materials, interacting with several deterioration initiators such as relative humidity, raindrops, wind, gas pollutants and particulate matter (PM) [2].

Fig. 1.1.1: The Little Mermaid by Edveard Eriksen, Copenaghen (1913) [3]

Although several studies have focused on water and gases interactions with metallic surfaces, just a very small portion, dealing mainly with stone manufacts and buildings, have investigated the PM deterioration role on cultural heritage [4, 5]. Particulate matter can contribute to different levels of alteration of exposed materials; the two main aspects that are concerned regard, respectively, soiling and corrosion. While soiling induces a damage of the aspect of a material, even hiding completely the visual image of an artwork, but limiting its action to the near surface region, corrosion results in a more aggressive behavior, which can lead to the alteration of deeper layers of an object, until the loss of its outer details and shape [6].

The PM fractions which play a protagonist role on soiling and on corrosion are not necessarily the same, or they can tend to act on both the phenomena at different extent: as an example, insoluble inorganic constituents remain on surfaces virtually unaltered, contributing more to soil the surfaces than to corrode them [7]. However, it is important to not misunderstand this statement and to not consider the PM fractions contributions to soiling and to corrosion as completely independent, because they can influence each other leading to lighter or more aggressive actions in both cases.

So far the role of PM as corrosion initiator for bronzes has not been studied deeply yet, as gases and acid rains are primarily considered in most of the projects concerning the cultural heritage [8-10], and moreover usually related to stone substrates [11]. Therefore, this is a topic that deserves further attention and suitable procedures needs to be set for its investigation. To this regard, there are some crucial aspects to care about when studying PM-promoted corrosion of metallic surfaces, such as the decision if performing ambient and/or accelerated ageing; the choice of the ageing methodology and conditions; the evaluation of the suitability/possibility to use ambient or synthetic PM in accelerated ageing; the set-up of procedures to collect ambient PM or to suitably prepare and deposit the synthetic one.

This thesis aims to focus on the aspects which concern the corrosive behaviour of PM towards bronze specimens, investigating both the interaction of solid PM particles hitting directly bronze surfaces (dry deposition) and the deterioration features of PM particles crossed by raindrops during their trajectories towards

bronze manufacts (wet deposition). In order to reach this goal, studies to formulate suitable PM compositions, starting from the contributions of single components up to complex mixtures, and to set proper methodologies of deposition and aging were performed and will be discussed in the next chapters. In particular, the study of PM role on corrosion requires the setup of accelerated aging methodologies which can be applied to substrates of different nature and which can allow to control operative conditions, so that the accelerated aging extent can be compared to natural aging phases and varied as needed.

2 Basics

2.1 Corrosion

According to the IUPAC definition [12], the term “corrosion” indicates: “An irreversible interfacial reaction of a material (metal, ceramic, polymer) with its environment, which results in consumption of the material or in dissolution into the material of a component of the environment. Often, but not necessarily, corrosion results in effects detrimental to the usage of the material considered. Exclusively physical or mechanical processes such as melting or evaporation, abrasion or mechanical fracture are not included in the term corrosion.”

Atmospheric corrosion is an electrochemical process that happens in the presence of a thin film of humidity produced by dew, raindrops or simply by gaseous water when RH is above 20% [13]; water acts as electrolyte, resulting in a conductive medium for the transfer of electrical charges, allowing the metal to oxidize and to release ions in solution, and the oxygen that is dissolved in the water layer to reduce to hydroxyl ions. The subsequent evaporation of the aqueous layers induces the precipitation of metallic hydroxides or oxides and the formation of a patina of several corrosion products, whom nature determines the safety of the substrate to further corrosion phenomena [14].

Even though the exposure to the rainfall is stated to be one of the main promoters of corrosion [15], combining its mechanical action to the vehiculation of corrosive chemical species, also particulate matter can play a role on it, both mechanically, if considering solid grains of salts hitting on surfaces, and chemically, when the water-soluble fraction undergoes to deliquescence or simply hygroscopic particles prevent water from leaving the surfaces fast, so that the wettability of surfaces is enhanced and ions can trigger corrosive reactions in solution [16].

2.2 Patina on bronzes

Since the Bronze Age, bronze alloys, which consist primarily of copper (virtually 88% for modern bronzes) and in smaller percentages of tin, lead, zinc and other metalloids, have been used to produce manufacts, many of which have been

conserved up to now, even if they do not look exactly like they were originally. In fact, because of the interaction with the environment, patinas of corrosion products develop in time scales that vary locally according to the environmental conditions, ranging in between 20 and hundred years in Europe [6].
The patina on bronzes is a chemically and spatially complex heterogeneous structure, whose composition is dependent on the alloy and on the chemical composition of the atmosphere [17]. If the patina is not porous and adheres well to the bronze surface, it can act as a barrier against humidity and polluting agents; viceversa, the formation of products which are dusty and porous can promote further corrosion processes, up to the complete dissolution of the substrate, if conservation strategies are not applied [6].

It is proved that the phenomenon of outdoor copper corrosion starts with the formation of a cuprite (Cu_2O) layer, which seems to be responsible of the gradual deceleration of the corrosion rate of copper alloys after the first years of exposure: increasing the exposure time, this cuprite layer becomes thicker and compact, leading to a further protection of the metallic substrate. Later on, above the cuprite layer, corrosion products form, mainly constituted by copper salts, with a chemical composition that depends on the exposure environment (urban, marine, industrial one) [18]. In addition to cuprite, common mineralogical phases found on bronze patinas are the result of the interaction between copper and sulphate, chlorine, carbonate and nitrate ions combined with moisture, even though nitrate salts are usually less found because of their high solubility in water. Some of the most recurrent minerals in patinas, mainly consisting in naturally occurring minerals of sulphur and chlorine, as discovered by Vernon around 1930 [19], are listed in Table 1 [20]. It can be noticed that the chemical composition of some of these compounds is quite similar: in fact, it is possible to interconnect their experimental occurrence creating an evolution scheme of copper corrosion products as a function of time (Fig. 2.2.1), as proposed by Krätschmer et al. [21]. Although the corrosion of copper alloys has been assimilated for a long time to that one of copper, the role of the other alloying elements such as tin and lead is crucial for the development of the corrosion stages of bronzes, and therefore not negligible [8].

Table 1: Common copper-containing minerals in bronze patinas [2] [20]

Mineral name	Chemical formula	Description
Brochantite	$Cu_4(SO_4)(OH)_6$	It is virtually the most common component of the green patina that is formed after a long atmospheric exposure, found for example on the Statue of Liberty located in New York Harbour.
Antlerite	$Cu_3(SO_4)(OH)_4$	As antlerite is more stable than brochantite in acidic conditions, in the case of acidic rain exposure brochantite can convert to less protective antlerite, which is more prone to erosion.
Posnjakite	$Cu_4(SO_4)(OH)_6 \cdot H_2O$	Hydrated form of brochantite, which it may co-exist with or transform into.
Chalcanthite	$CuSO_4*5H_2O$	Hydrated copper sulphate form, usually found together with brochantite in archaeological bronze artefacts.
Atacamite	$Cu_2Cl(OH)_3$	It has been found frequently as or more than brochantite in patinas formed near the sea after long exposure times.
Paratacamite	$Cu_{1.5}Zn_{0.5}(OH)_3Cl$	Its presence is transitory and it eventually converts to atacamite; not found on specimens exposed for long times. It consists in an alteration of copper by chloride waters under cold conditions.
Clinoatacamite	$Cu_2(OH)_3Cl$	Well known corrosion product on ancient bronzes buried in soil.
Gerhardite	$Cu_2NO_3(OH)_3$	It is found in bronze specimens that have not been exposed to rainfall, which would wash out the nitrate salts unabling their detection.
Malachite	$Cu_2(CO_3)(OH)_2$	Usually found on archaeological manufacts.

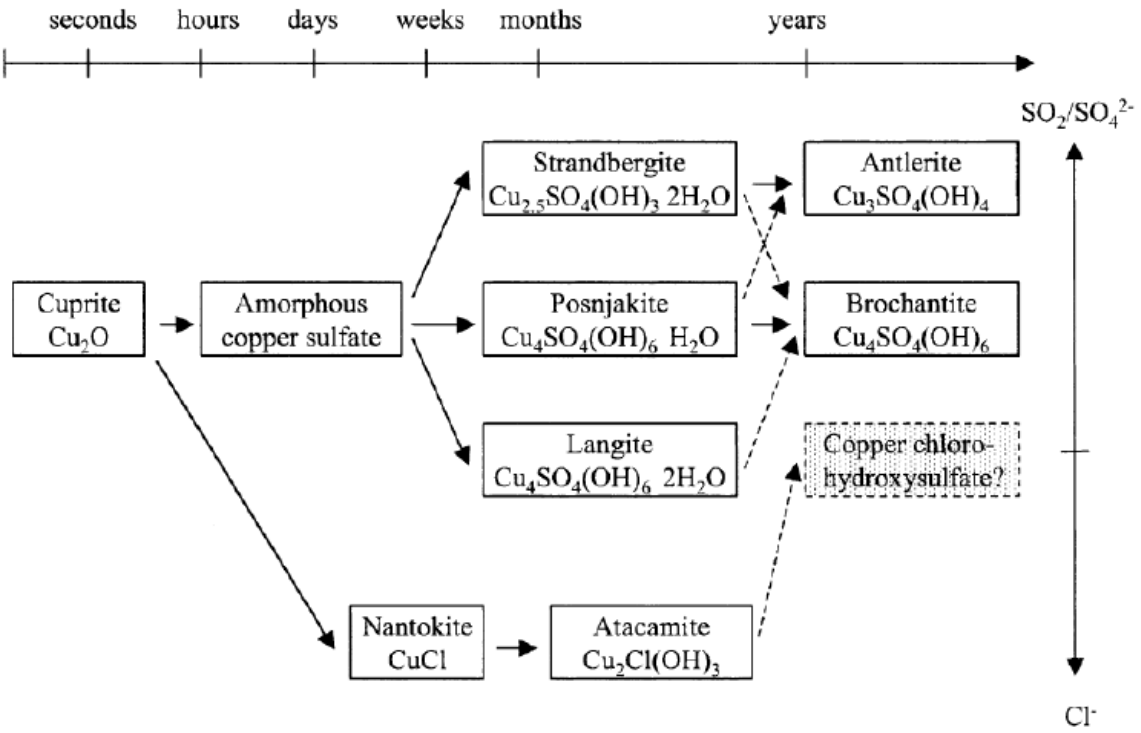

Fig. 2.2.1: Copper patina corrosion products evolution over time [21]

There can be other corrosion products than copper ones occurring in patinas, for example: cerussite ($PbCO_3$), hydrocerussite ($Pb_3(CO_3)_2(OH)_2$), anglesite ($PbSO_4$) [22,23], cassiterite (SnO_2) [24]. According to previous studies by Chiavari et al. [8], on one hand the Pb-based corrosion products occurrence is related to a lead enrichment onto the surface with respect to the bulk during smoothing processes, leading to the formation of lead oxides that slow down the copper dissolution during the first stages of exposition and, later on, that are substituted by further more stable corrosion products, more likely sulphates; on the other hand, the occurrence of tin oxides has been observed as a consequence of decuprification phenomena. Regarding zinc corrosion products, hydrozincite ($Zn_4CO_3(OH)_6 \cdot H_2O$) and simonkolleite ($Zn_5(OH)_8Cl_2$) are reported as the main minerals found in alterated zinc specimens exposed in a marine environment, but in the case of bronzes, in which the Zn amount is low and the solubility of its corrosion products is high, making them prone to dissolve in the presence of humidity, Zn alteration products have not been detected [8,25].

2.3 Particulate matter

2.3.1 Definition

Several definitions can be given of “particulate matter”. In the IUPAC Goldbook [12] it is written that: “It is a general term used to describe airborne solid or liquid particles of all sizes. The term aerosol is recommended for general use in describing airborne particulate matter.”
For the United Stated Environmental Protection Agency (EPA) [26]: “It is a complex mixture of extremely small particles and liquid droplets. Particle pollution is made up of a number of components, including inorganic acids and salts (such as nitrates and sulphates), organic chemicals, metals and soil or dust particles.”
The term PM therefore refers to all the particles that can be suspended in air and transported before they settle somewhere else [27], including both liquid and solid particles, without limitations concerning the particle size and its chemical identity.

2.3.2 Composition, sizes, sources

From the citations in the paragraph 2.3.1, it is possible to notice that the term “particulate matter” does not indicate something with a well-defined chemical composition. The huge variety of components and their ratios is related to the occurrence of certain emission sources, as shown in Table 2, and changes in the climatic conditions, both seasonal and daily ones. In general, tropospheric aerosol contains sulphates, nitrates, chloride, ammonium, sodium, potassium, trace metals, carbonaceous material (consisting both of organic and elemental carbon), crustal elements and water in variable proportions; the relative ratio of PM components that can be found on surfaces changes according to the orientation of specimens, to deposition mechanisms, related to the aerodynamical diameter of the particles, and to the emission sources that are present in the considered area, taking into account that the average transportation distances vary according to the particle size and lifetime [16]. Sulphates, nitrates, organics and soot are mainly found in the fine fraction of PM, while chlorine salts, dust, biological particles and particles from abrasion in the coarse one. This general repartition in size classes “PM_x”, where “x” is the upper

limit of the aerodynamical diameter involved (Fig. 2.3.2), is somehow connected with the origin of those particles: for example, NaCl comes mainly from sea spray as primary particles, while sulphates and nitrates are usually secondary airborne particles, as in the case of NH_4NO_3 and $(NH_4)_2SO_4$, which derive respectively from the reaction of ammonia with HNO_3 and H_2SO_4, acids that are formed by their gaseous precursors NOx and SOx reacting with ozone, hydroxyl radicals, hydrogen peroxide or diatomic oxygen [28].

Table 2: Relations between composition, sizes and sources of PM [28]

	Fine particles	Coarse particles
Formation pathways	Chemical reactions Nucleation Condensation Coagulation Cloud/fog processing	Mechanical disruption Suspension of dusts
Composition	Sulfate Nitrate Ammonium Elemental carbon Organic compounds Water Metals (Pb, Cd, V, Ni, etc.)	Resuspended dust Coal and oil fly ash Crustal element (Si, Al, Ti, Fe) oxides $CaCO_3$, NaCl Pollen, mold, spores Tire wear debris
Sources	Combustion Gas-to-particle conversion of NOx, SOx and VOCs Smelters, millers, etc.	Resuspension of industrial dust and soil Suspension of soil Biological sources Construction/demolition Ocean spray

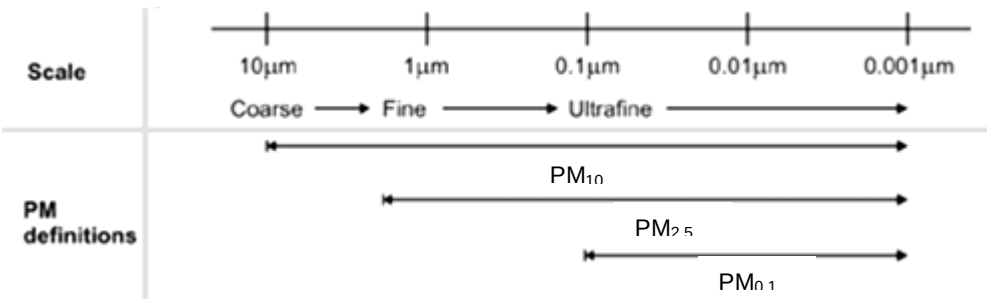

Fig. 2.3.2: PM classification according to the aerodynamical diameter [29]

The atmospheric concentration of certain species depends on the occurrence of emission sources, distinguishable in natural and anthropogenic ones, which influence and eventually characterize an environment. In general, three scenarios that have their own peculiarities are:

- *marine environment*, in which the natural sea spray component is predominant;
- *urban area*, where combustion of fuels by vehicles, domestic heating and industries is enhanced, leading to the production of several fine PM components (see Table 2);
- *rural site*, that consists in a territory where vegetation and agricultural activities are the principal inlet of PM, including pollen, spores and suspended soil particles.

Because of all these differences, when simulating PM and its interactions with materials, it is important to contextualize which environment the study is referred to.

2.3.3 Natural PM collection

Outdoor-exposed metallic manufacts present in a short time deteriorated features for the sum of several contributions to the PM one, such as rain and wind effects [30]; the superimposition and sum of several factors leads to difficulties in the isolation of the PM contribution to alterations. In literature there are several standardized methodologies for the PM sampling, such as filtration, electrostatic and thermal precipitation and inertial separators; this last method is particularly suitable for routine analyses, and is therefore the most widely adopted by regulatory bodies like the European Union (EU) and the Environmental Protection Agency (EPA), which has chosen the high volume method as reference for the determination of total suspended particulate matter (TSP) and PM_{10} if outfitted with a size selective inlet [31-33].
Even though the PM collection has already its reference techniques, just a few methods involve the direct collection onto specimens, for studying the material

response to such exposures. One of the most important contributions concerning air pollution effects on cultural heritage was the MULTI-ASSESS project; in the framework of this project, a passive particle collector was developed [34], in order to analyse deposited PM and to perform corrosion studies on wind-protected and wind-exposed samples both in rain-protected conditions. In wind-exposed conditions, transport over long distances is enhanced and sticking coefficients have to be taken into account in order to relate corrosion products to their effective precursors, because both adhesion and removal mechanisms can be influenced, resulting in a high variability of sampled PM depending on exposure conditions.

For studying dry depositions by excluding the wind variable, deposition boxes can be used [35,36]; thanks to these devices, the experimental PM composition, temperature and relative humidity are the ones available in the surroundings. Removing the wind variable, it is even more striking the evidence of differences in the sampling on horizontally and vertically-placed coupons, as gravity affects mainly the coarse PM fraction, while diffusion works better for fine particles, leading to different relative contents of analytes characteristic of the two fractions [37]. Therefore, deposition boxes allow to perform field exposure of specimens focusing on PM effects by excluding rain or wind effects. Time required for collecting PM and observing deterioration effects is of the same order of magnitude or classical field exposure. So, in case corrosion steps should be monitored on PM collected by deposition boxes, the monitoring should be performed during the exposure into the device on a time scale of months or even years. Anyway, beside necessary field exposures, accelerated ageing tests are also required to better separate and follow specific deterioration mechanisms or to distinguish which species contribute to a certain alteration pathway. To this regard, deposition box is not an ideal devices to simply collect ambient PM on specimens that want to be submitted to accelerated ageing tests, because sampling requires time to gain measurable concentrations of analytes and, during this time, corrosion on reactive surfaces, as bronze ones, goes on and several deterioration products could form.

According to these considerations, deposition boxes result to be suitable to field investigate ambient PM behaviour against materials and, in case, to create

comparisons for the evaluation of strengths and limitations of accelerated methodologies of sampling and aging that, although simplified with respect to the natural processes, are necessary to gain a deeper knowledge of corrosion phenomena.

A faster way for sampling onto specimens is to use an impactor, as investigated by Baietti F., 2018 [38], consisting in a high volume sampler, that is a reference instrument for PM collection, where some modifications were applied. This device allows to collect a uniform, quantitatively significant and compositionally homogeneous PM deposit in relatively short times, permitting the sampling of natural PM and avoiding long exposure times that would let specimens react with airborne particles.

2.3.4 Synthetic PM preparation and deposition methods

Another way to study PM components' role on corrosion is to prepare synthetic PM, adjusting concentrations to the ranges required in the investigation. An interesting example of an artificial synthetic PM recipe is presented in a study regarding soiling of building envelopes by Sleiman et al., 2014 [39]: aqueous solutions to represent respectively the organic fraction, the mineral fraction, the black carbon fraction and the soluble salts one were combined together varying their ratios according to the type of PM composition to represent (hot and humid, hot and dry, polluted atmosphere).

Among the wet deposition methods that can be found in literature, two nice case studies to cite involved the spray of aqueous solutions [39] and the dropping with pipettes of NaCl dissolved in ethanol [40]. The spray method using aqueous solutions has the advantages of dispersing small size droplets and of better representing the interaction of PM with water drops, as in the case of raindrops that cross airborne particles through their path before hitting a surface. On the other hand, the deposition of an ethanol-based drop onto a surface allowed to get a quite uniform distribution of the salt better simulating a dry deposition than a wet one, as the evaporation of the alcohol is so fast that it prevents from the contribution of the solvent to the metallic surface corrosion.

Dry depositions of fine particles have been performed via dry powder aerosol delivery [41], although this methodology has not been tested for PM deposition, but for proteins inhalation.

2.4 Ageing methods

Accelerated ageing can be performed in several ways depending on which phenomena have to be investigated; among all the methodologies used to stress materials, salt spray is a technique that is commonly applied in galvanic industry to check the resistance and performances of specimens according to the norm EN ISO 9227:2017 [42,43]. Another methodology of aging concerns runoff, which is standardized for metals by ISO 17752:2012 [44]; according to this norm, it consists in a system that simulates the rainfall by dropping artificial rain onto an inclined surface [45,46]. One last methodology of aging to cite, which simulates the effects of stagnation, is alternating immersion: this procedure, which is particularly applied in case of porous materials, implies cycles of immersion and emersion of specimens from a salts-containing solution, in order to simulate those deterioration phenomena affecting manufacts which have remained underwater for a long time, as in the case of the Riace Bronzes [47,48].

In order to accelerate the PM-induced corrosion, a suitable methodology to apply is the setting of aging cycles in controlled conditions thanks to climatic chambers; cycles have been drawn in several different ways, showing that nowadays there is not an uniform standardized methodology to follow for the aging of bronze specimens in reliable environmental conditions: in fact, in several cases the set T and RH are far from reality, and stress the samples in ways that are not representative. Three of the most interesting examples of aging cycles for metallic artefacts, together with their advantages and withdrawings, are presented below.

The thermal cycling with humidity based on ISO6270-2CH (condensation atmosphere with constant high humidity) [49], shown in Fig. 2.4.1 (a), varies in a T range from -40°C up to 90°C, keeping ambient RH; then, T stabilises around 40°C and RH is brought up to 100%. This cycle is fine to test materials in very

harsh conditions, trying to simulate also frosting, but the T ranges are definitely not realistic, and therefore not suitable to mimic effective aging.
The ISO11507 UV+Water test [50], depicted in Fig. 2.4.1 (b), sets the T range between 50 and 60°C, conditions that can match only with summer T values during the hottest hours of the day; therefore, no representation of the night conditions is given using this cycle. The RH range is more promising, as it extends between ambient RH when T is high and RH 100% when T decreases, as it happens in the case of natural T and RH oscillations. The cycle is implemented also with light, in order to provide radiation interaction to the specimens, but the lighting steps do not match with realistic T values for night time [51].

Better T and RH ranges for bronzes aging have been used in experiments published by Ferrari A. (2009) [52]: specimens were placed in a climatic chamber where a 24 hours aging cycle was repeated; the steps required 8 hours at T 35°C and RH 65%, 4 hours in a controlled ramp to reach T 5°C and RH 85%, then 8 hours at T 5°C and RH 85% followed by another 4 hours ramp to get back to the initial conditions. The cycle well represents daily fluctuations of T and RH on an overall of 24 hours, including during the controlled ramps; however, no justification of the limit values of T and RH was given.

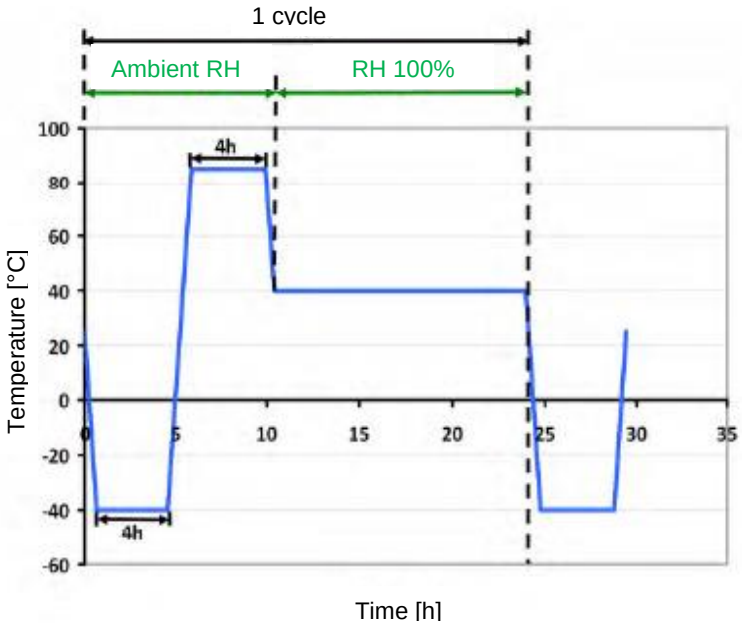

(a)

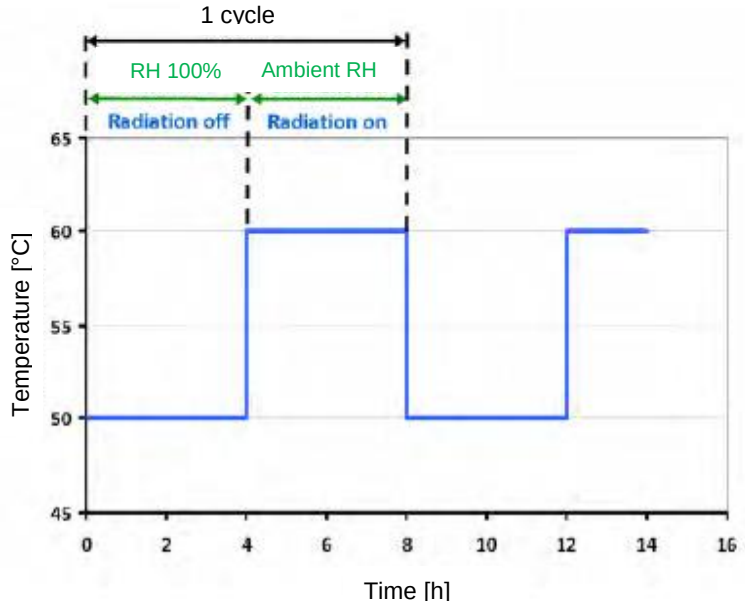

(b)

Fig. 2.4.1: a) Thermal cycling with humidity based on ISO6270-2CH; b) ISO11507 UV+Water test [51]

3 Materials and methods

3.1 Specimens

Samples consisted in quaternary bronzes (Cu 88,76%, Sn 4,4%, Pb 3,9%, Zn 2,4% w/w) [53] containing trace elements below 1% w/w (i. e. Ni and Fe). Clean surfaces were obtained by smoothing the upper layers of the bronzes by using sandpaper of different roughness, from 600 grain up to final refinement with 1000 grain one. Samples were weighted, measured by using a caliper, in order to determine the main face areas, and placed into a dryer.

A set of specimens around 1 cm x 1,5 cm x 0,4 cm was used to perform depositions of artificial PM in wet and dry manners, as described in section 3.2.1. Borders and bottom face of those bronzes were treated with an insulating lacquer (V66-Due Ci Electronics snc) that was applied by using a paintbrush to the surfaces, and then let dry for 2 hours before weighting again the samples. After the application of the lacquer, Teflon tape was overtight around the specimens (Figure 3.1.1), in order to create rised borders and to avoid that the analytes flow out when in a deliquescent or a dissolved state. Then, weight of samples was recorded again. These specimens were analysed by Scanning Electron Microscopy – Energy Dispersive X-rays (SEM-EDX, section 3.7.2) and Raman Spectroscopy (section 3.7.3) before the PM deposition, after the PM deposition, then each week during their aging cycle. At the end of the ageing the “dry” samples were also analysed by Attenuated Total Reflectance – Fourier Transform IR (ATR-FTIR, section 3.7.4) and pickled, while the “wet” ones were pickled (pickling procedure, section 3.6) and the pickling solutions were analysed for the metal content by Atomic Absorption Spectroscopy (AAS, section 3.7.6).
A sacrificial bronze sample (5,15 cm x 2,56 cm x 0,40 cm) was treated depositing single salts in wet manner (see paragraph 3.2.1) as the previous ones and used to perform colorimetric and pH measurement periodically during the aging cycles, without damaging the other samples cited above.
Another sample sized 5,18 cm x 2,54 cm x 0,40 cm was used to collect two spots of natural PM via an impactor obtained appropriately modifying a high volume sampler [38]. This specimen was aged into the climatic chamber in order to see if

corrosion processes promoted by natural PM presented similar features to the simplified systems that were prepared artificially.

Fig. 3.1.1: Bronzes after lacquer and Teflon application

3.2 Synthetic PM

In order to study the effect of single aerosol components and their mixtures, specimens were grouped into three different sets:

1) the first set was constituted by samples where pure single salts (section 3.2.2) were spread respectively via wet and dry deposition, in order to evaluate the relative corrosive power of common anions and cations;
2) the samples belonging to the second set were treated with a ternary salts mixture (section 3.2.3), in wet and dry modality;
3) the third set of samples was soiled with the same soluble salts in addition to an artificial, more complex and realistic matrix (section 3.2.4).

The sets of samples were treated according to both wet and dry modalities, except for the third one, for which just the wet deposition was performed

because of difficulties in grinding and mixing properly the components. Equivalents were the unit that was used to calculate the amount of salts to spread on the samples; in order to establish if moles or equivalents were more suitable to work out calculations, activity plots achieving data from the E-AIM software [54] were drawn preliminarily and are reported in paragraph 4.1.3.

3.2.1 PM deposition modes

"Wet" deposition

The wet deposition mode was tested in order to simulate the phenomena of rain-out, consisting in the inclusion of PM in droplets forming into a cloud, and wash-out, when drops that fall down encounter PM before their impact onto a surface. In order to perform wet depositions, appropriate volumes of solutions containing defined amounts of salts (pure or mixture) were dropped by using a micropipette and spread on the upper face of each sample. Then, the specimens were placed in the climatic chamber at T 80°C and RH 30% for about 4 hours, in order to dry. After this time, samples looked like displayed in Fig. 3.2.1, and the crystallization of the salts was checked by using an Optical Microscope: if no traces of water were observed, samples were ready to undergo to aging cycles; viceversa, the drying procedure was repeated.

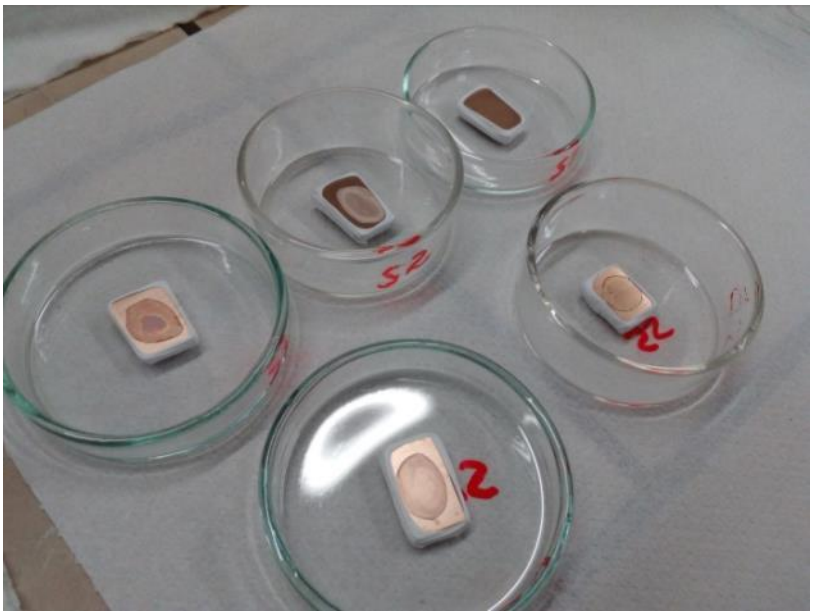

Fig. 3.2.1: Wet depositions and drying of single salts. From the top left, specimens treated with $NaCl$, $NaNO_3$, Na_2SO_4, NH_4NO_3 and $(NH_4)_2SO_4$.

“Dry” deposition

Salts were grinded and then spread directly onto the specimens paying attention to maximize their dispersion (Fig. 3.2.2 (a)), put in climatic chamber at T 21°C and RH 90% in order to make them deliquesce (Fig. 3.2.2 (b)), and then dried at T 80°C and RH 30% (Fig. 3.2.2 (c)).

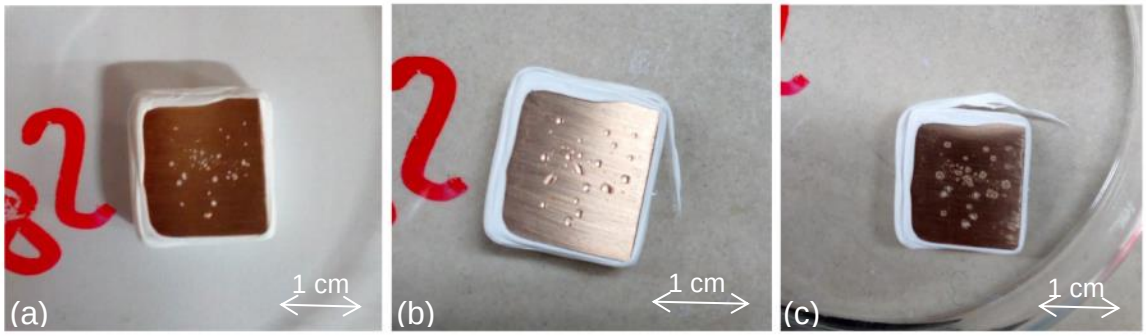

Fig. 3.2.2: Dry deposition of NaCl. From the left, NaCl “dry” (a) just after deposition; (b) in deliquescence; (c) dried.

By solubilizing the salts and depositing them via “wet” deposition, the first recrystallization produces crystals of fine dimensions (below 10 μm), while the grinding of the salts for the “dry” deposition leads to particle sizes belonging to the coarse fraction (20-50 μm), better representing the real dimensions of chlorine salts.

3.2.2 Single salts

Single salts to apply onto the specimens were chosen combining the most common anions (Cl^-, NO_3^-, SO_4^{2-}) and the most occurring associated cations (Na^+ to Cl^- and NH_4^+ to NO_3^- and SO_4^{2-}) found on samples after PM sampling campaigns [36]. Carbonates are not particularly soluble in neutral water, and therefore were not considered at this point, as soluble salts are the main concern because of their deliquescence cycles. The cited anions were combined to both Na^+ and NH_4^+ cations, except for Cl^-, as chlorides are usually found associated as sodium salts. Nitrates and sulphates are often found associated to ammonium, but sodium was chosen as common counterion to all the anions for the comparison of the anions action, as it is considered as not particularly

influencing the corrosion. Conversely, ammonium is reported as a cation that possibly influences corrosive processes by itself; for this reason, the usage of salts displaying a counterion not particularly influencing the corrosion and ammonium containing salts should allow to evaluate its action by comparison. The soluble salts which were therefore chosen are sodium chloride (NaCl, CAS: 7647-14-5), sodium nitrate ($NaNO_3$, CAS: 7631-99-4), sodium sulphate ($NaSO_4$, CAS: 7757-82-6), ammonium nitrate (NH_4NO_3, CAS: 6484-52-2), ammonium sulphate $(NH4)_2SO4$, CAS: 7783-20-2).

The deliquescence conditions for each pure salt were checked in literature and compared to calculated values using the E-AIM software [53], in order to predict when deliquescence would have happened during the aging cycles. E-AIM predictions about the Deliquescence Relative Humidity (DRH) of the salts at different temperatures were validate visually by placing specimens in the climatic chamber and running cycles setting T constant and theoretical DRH ± 3%.

The applied “wet” and “dry” deposition modalities are the ones described in the paragraph 3.2.1. For the “wet” depositions, the amount of salts to weight was determined by the outcomes of a 63 days exposure campaign by using Deposition Boxes in Rimini [36]. Data on masses and moles of collected ions are reported in Table 3; in particular, the amount of ion expressed as µg ion/cm^2 in a 63 days campaign, is the average over all the horizontal filters used in the reference campaign, except for the aluminum ones, as they were found to be very reactive towards some PM components [36].

It was decided to spread onto the specimens amounts of salts simulating 5 years of outdoor exposure in the Rimini environment. In order to compare the corrosive power of the anions, the average of the equivalents of the anions (NO_3^-, SO_4^{2-}, Cl^-) has been calculated equal to 2,0E-08/cm^2 (see data in Table 3). This average has then been set as fixed value for all the anions, and the respective moles have been recalculated. As it can be noticed by values in Table 4, quantities of salts to weight to achieve not concentrated solutions are very small, therefore a larger amount of salts was weighted to formulate 10000 times concentrated solutions (10000x) that were then diluted to 10 times concentrated (10x) and in the end to not concentrated (1x) solutions. From the final solution, 100 µL were withdrawn for each cm^2 of the samples to cover. In addition to the

cited samples, a wet deposition blank specimen was prepared by withdrawing just a distilled water drop (100 µL/cm^2) on it.

Table 3: Quantities related to input ions

	Cl^-	NO_3^-	SO_4^{2-}	Na^+	NH_4^+
Average of µg ion/cm^2 in 63 days on horizontal filters [36]	1,82	2,62	1,21	1,34	0,27
Average of µg ion/cm^2 per month on horizontal filters	0,91	1,31	0,65	0,67	0,135
Moles/cm^2 per month on horizontal filters	2,6E-08	2,1E-08	0,6E-08	2,9E-08	0,7E-08
Equivalents/cm^2 per month on horizontal filters	2,6E-08	2,1E-08	1,3E-08	2,9E-08	7,5E-09

Table 4: Amount of salts to weight for preparing solutions at different concentrations

	g NaCl	g $NaNO_3$	g Na_2SO_4	g NH_4NO_3	g $(NH_4)_2SO_4$
Moles/cm^2 1x	1,157E-06	1,68257E-06	1,406E-06	1,58457E-06	1,308E-06
Moles/cm^2 10x	1,157E-05	1,68257E-05	1,406E-05	1,58457E-05	1,308E-05
Moles/cm^2 10000x	1,157E-02	1,68257E-02	1,406E-02	1,58457E-02	1,308E-02

For the dry depositions, the amounts of salts weighted were corresponding to an estimation of 5 years of deposition as in the case of samples treated in wet modality. The main spots that were observable macroscopically on the samples were mapped and their area monitored by graphical measurements using the

ImageJ software. A dry deposition blank specimen, where nothing was spread on, was placed into the climatic chamber with these samples.

3.2.3 Ternary salt mixture

A mixture of sodium chloride (NaCl, CAS: 7647-14-5), sodium nitrate ($NaNO_3$, CAS: 7631-99-4) and sodium sulphate ($NaSO_4$, CAS: 7757-82-6) was prepared, keeping the same equivalents of each anion that were used onto the single salt specimens. Both wet and dry depositions were performed using the same modalities of the single salts specimens. DRH information was achieved thanks to the Model IV of the E-AIM software [54], in which data regarding this ternary system were input to get hints on DRH variations with respect to single salt systems.

3.2.4 Mixture simulating natural PM

In order to mimic a natural PM that is deposited in wet conditions, a more complex mixture was prepared including other PM fractions (grouped in the so-called “matrix”), not yet considered, than soluble salts.

The “matrix” formulation was done by combining a mineral fraction, a black carbon fraction and an organic fraction in distilled water. The preparation of the black carbon and of the organic fractions were the same as in the recipe proposed by Sleiman et al. (2014) [39], respectively 1,25 g/L of biochar (code: SWP700), representing the black carbon fraction, and 1,4 g/L of humic acids (CAS: 1415-93-6) in distilled water. In order to represent the mineral fraction, 1 g/L of $CaCO_3$ (CAS: 1317-65-3) and 1 g/L of SiO_2 (CAS: 60676-86-0) were dispersed in distilled water. Reagents were mixed together and solubilized in 1 L of distilled water after grinding them.

The “matrix” was spread onto a bronze sample (100 $\mu L/cm^2$) to evaluate the effects of mineral and organic fractions constituting it. Another sample was treated with the complete mixture simulating natural PM, consisting of the same matrix but enriched of a soluble salts fraction.

The soluble salt fraction was constituted by ammonium sulphate ($(NH_4)_2SO_4$, CAS: 7783-20-2), ammonium nitrate (NH_4NO_3, CAS: 6484-52-2), sodium chloride (NaCl, CAS: 7647-14-5), sodium nitrate ($NaNO_3$, CAS: 7631-99-4), sodium sulfate ($NaSO_4$, CAS: 7757-82-6), calcium sulfate diyhdrated ($CaSO_4*2H_2O$, CAS: 10101-41-4) and calcium carbonate ($CaCO_3$, CAS: 471-34-1) mixed together. The concentration of this fraction was kept equal to 1 g/L of distilled water as in the Sleiman et al. (2014) recipe [39], but the amount of single components and their nature were varied according to the data obtained from a 63 days exposure campaign in Rimini using Deposition Boxes [36].

First, the average amounts of the single ions deposited in one month were retrieved. From those data, the relative percentages (w/w) of the cations were calculated. Considering that a solution of 1 g/L of salts had to be prepared, it was estimated that its composition should be 31% of sodium salts, 6% of ammonium salts and 63% of calcium salts. As calcium ions were already introduced in the "matrix" as calcium carbonate, the amount of Ca^{2+} ions could be lowered to 13% and the relative amounts of cations recalculated as follows: 56% Na^+, 21% NH_4^+, 13% Ca^{2+}. Considering the relative percentages of anions, it appeared that chlorides were 32%, nitrates 46% and sulphates 22% of the total amount of anions (carbonates were not considered, as their solubility in neutral water is negligible). According to the salts that were chosen for preparing the salt fraction, anions can be mixed with the different cations in the ratios listed in Table 5. However, in this representation nitrates and sulphates are significantly associated with sodium, while in nature, differently from chlorides that are usually met just with sodium, sulphates and nitrates are mainly associated with ammonium [39]. Therefore, these data have been recalculated by varying the percentages of salts to better fit real associations (Table 6).

Table 5: Preliminary estimation of anions and cations combination

	Cl^-	NO_3^-	SO_4^{2-}
sodium salts (0,56 g tot)	0,1792	0,2576	0,1176
ammonium salts (0,21 g tot)	-	0,1426	0,0651
calcium salts (0,13 g tot)	-	-	0,13
anions sum per species	0,1792	0,4002	0,3127
% anions w/w	20%	45%	35%

Table 6: Correction for realistic combinations of ions

	Cl^-	NO_3^-	SO_4^{2-}	SUM
sodium salts (0,6 g tot)	0,3248	0,1904	0,0448	0,56
ammonium salts (0,3 g tot)	-	0,2697	0,0403	0,31
calcium salts (0,1 g tot)	-	-	0,13	0,13
single anions sum	0,3248	0,4601	0,2151	1
% anions w/w	32%	46%	22%	100%

Thanks to all the considerations discussed up to now, the recipe for the mixture simulating natural PM ("matrix" and soluble salts fraction) was defined and it is reported in Table 7. By withdrawing 100 μL of the solution (containing both the matrix and the soluble salt fraction) for each cm^2 to cover, we spread on each cm^2 the quantity of moles (reported in Table 8) which would be deposited in around 5 years of exposure. Samples with matrices and mixtures were placed in the climatic chamber and let dry at T 80°C and RH 30% for 4 hours, as it was done for single salts dropped samples.

Table 7: Recipe for the mixture with soluble salts and matrix

Substance		g/L
Char		1,25
Humic acids		1,4
Mineral fraction	SiO_2	1
	$CaCO_3$	1
Soluble salts fraction	NaCl	0,3248
	$NaNO_3$	0,1904
	Na_2SO_4	0,0448
	NH_4NO_3	0,2697
	$(NH_4)_2SO_4$	0,0403
	$CaSO_4*2H_2O$	0,13

Table 8: Moles in solution containing the amounts of salts in Table 7

Salt	MM	g/L	moles/L
NaCl	58,44	0,3248	0,005558
$NaNO_3$	84,99	0,1904	0,00224
Na_2SO_4	142,04	0,0448	0,000315
NH_4NO_3	80,04	0,2697	0,00337
$(NH_4)_2SO_4$	132,14	0,0403	0,000305
$CaSO_4*2H_2O$	172,17	0,13	0,000755

3.3 Natural PM

The collection of natural PM on a bronze specimen was carried out as described in the following. Using a high volume sampler Echo HiVol (TCR Tecora), where all the nozzles were blocked except for two couples of adjacent holes, a bronze specimen was hit perpendicularly onto the impact disk by an air flow passing through the open accelerating nozzles, achieving a high concentration of PM in two 9 mm diameter spots. PM was collected through inertial impact, which

happens when a particle proceeds along its tangent, unable to follow the direction variations of the flux near the impact surface, until it hits the substrate. Taking into account that the probability of inertial impact enhances proportionally to the flux velocity, to the raising size of the particles and in the presence of a high density impact surface, $^2/_3$ of the nozzles were plugged and the impact surface approached to the open ones, in order to get a sampling flow of 400 L/min that could sample also PM fractions below PM_{10}. The sampling was performed in the framework of Baietti's thesis [38] and lasted 22 hours; then, before the ageing, the residues were characterized by SEM-EDX and Raman analyses.

1) Programming and motor apparatus
2) Sampled air discharge
3)Temperature sensor
4) Casing for polyurethane foam (PUF)
5) Filter holder cone
6) Perforated net
7) Nylon ring
8) Clamping ring for the sampling head
9) Sampling head PM_{10}, constituted by:
10) impact disk

Fig. 3.3.1: High volume sampler a) external overview; b) inner details; c) sampling head details [38]

3.4 E-AIM modelling

The Extended AIM Aerosol Thermodynamics Model (E-AIM) [54] is a model for the calculation of phases partitioning in aerosols and solute and solvent activities in aqueous solutions and liquid mixtures. It consists in a chemical system corresponding to the one described by Clegg et al. (2007) [55], shown in Fig.

3.4.1, which can contain the following condensed phases (all allowed to equilibrate with the gas phase):

- inorganic and organic solids;
- an aqueous phase containing both organic solutes and inorganic ions;
- a hydrophobic organic liquid phase.

In this work, organics were not considered, as the model was used to simulate single salt systems and a system containing a ternary mixture of NaCl, $NaNO_3$ and Na_2SO_4.

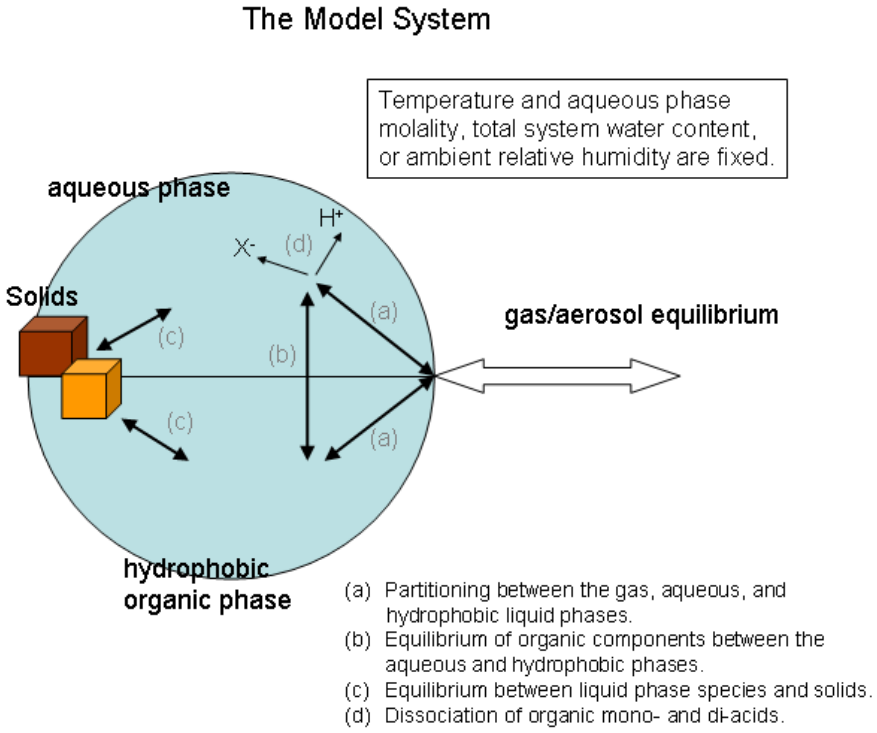

Fig. 3.4.1: Clegg. et al. (2007) model system [56]

Although in Fig. 3.4.1 the system looks like an aerosol droplet in equilibrium with the surrounding atmosphere, the calculations are the same as if a bulk system was considered. The model does not include aerosol size effects, that would enhance the equilibrium partial pressures of water and volatile components for fine particles. Equilibria between the liquid and the gas phases and the formation of solids are determined by both the analytes' activity coefficients and their concentrations in the aerosol phase. Calculations of the activities of water and ions present in the aqueous aerosol utilise the Pitzer, Simonson and Clegg

equations [56], which correlate activity coefficients f_i to the excess Gibbs energy for any amount of material G^E and to the n_i moles of the species i that are present according to equation (1). Taking into account equation (2), which defines the x_j mole fraction of the species j as the ratio between its number of moles and the sum of n_i moles, and defining the excess Gibbs energy per mole of particles g^E, calcunations can be written in the form of equation (3). The g^E term is assumed to be the result of the sum of short-range force (g^S) and long-range Debye-Huckel (g^{DH}) components, as shown in equation (4), which are derived by further expansions presented in Clegg et al. (1992) paper [56].

$$RT \ln (f_i) = (\partial G^E / \partial n_i)_{T,P} = (\partial (\sum_i n_i g^E) / \partial n_i)_{T,P} \quad (1)$$

$$x_j = n_j / \sum_i n_i \quad (2)$$

$$g^E = RT \sum_i x_i \ln (f_i) \quad (3)$$

$$g^E = g^S + g^{DH} \quad (4)$$

Regarding DRH calculations, an expression derived by Tang and Munkewitz (1993) [57] was applied. Most of experiments in literature derive DRH at T 25°C; then, by applying equations that consider the T dependence of DRH and that create a connection between DRH at a given T and DRH at another one, further data can be calculated. As shown in equation (5), DRH is dependent on solubility, enthalpy of solution and temperature.

$$d[\ln (DRH/100])/dT = -n (\Delta H_s / RT^2) \quad (5)$$

where DRH is the deliquescence relative humidity, T is the temperature, n is the solubility (mole of solute per mole of water), ΔH_s is the enthalpy of solution, R is the ideal gas constant (8,314 J*mol^{-1}*K^{-1}).

By expressing the solubility with a polynomial function of the type $n = A + BT + CT^2$, the equation (5) can be integrated from T_0 (298 K) to T, in order to outline the T dependence of DRH, leading to equation (6).

$$DRH(T) = DRH(298)\ exp\{(\Delta H_s/RT^2)\ [A\ (\frac{1}{T} - \frac{1}{298}) - B\ ln\ (\frac{T}{298}) - C(T - 298)]\} \quad (6)$$

where A, B and C are constant parameters that vary according to the species that is concerned and to its solubility at a given temperature.

Among the different types of calculations that can be performed by using the Model IV of E-AIM, in this study the *Simple Calculation* was chosen. This model determines the state of a system containing water and two or more ions (among H^+ - NH_4^+ - Na^+ - SO_4^{2-} - NO_3^- - Cl^-), at equilibrium with an atmosphere of known temperature and relative humidity. The formation of solids is allowed and can be controlled by the user, who inputs relative humidity (expressed as a fraction), temperature and moles of each ion that is present in the system; outputs regard the amounts of liquid water, dissolved ions, and solids present at equilibrium. The partial pressures or partial pressure products of any NH_3, HNO_3, HCl, or H_2SO_4 that would be in equilibrium with the condensed phase are also reported.

As an example, in Fig. 3.4.2 the input buttons of the Model IV that were useful for this study are displayed: both T and RH have to be input, as well as the ions moles to consider in the system; the outputs are presented in Fig. 3.4.3. Varying the RH and keeping T and ions moles constant, it is possible to achieve the DRH both for single and multicomponent systems, and to get hints about which species crystallize first and which remain in solution for a longer time. In this study also activity plots were drawn according to these calculations, in order to evaluate if equivalents or moles were more suitable to be considered for the sulphates (as in all the other cases that were studied no differences are displayed, because of the 1:1 ratio between anions and cations). Results about DRH and activity plots are presented in paragraph 4.1.

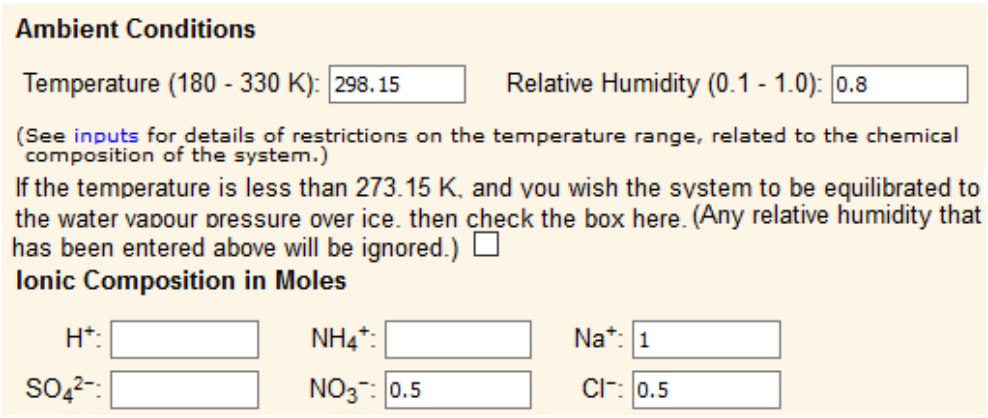

Fig. 3.4.2: E-AIM software – example of Model IV considered inputs [54]

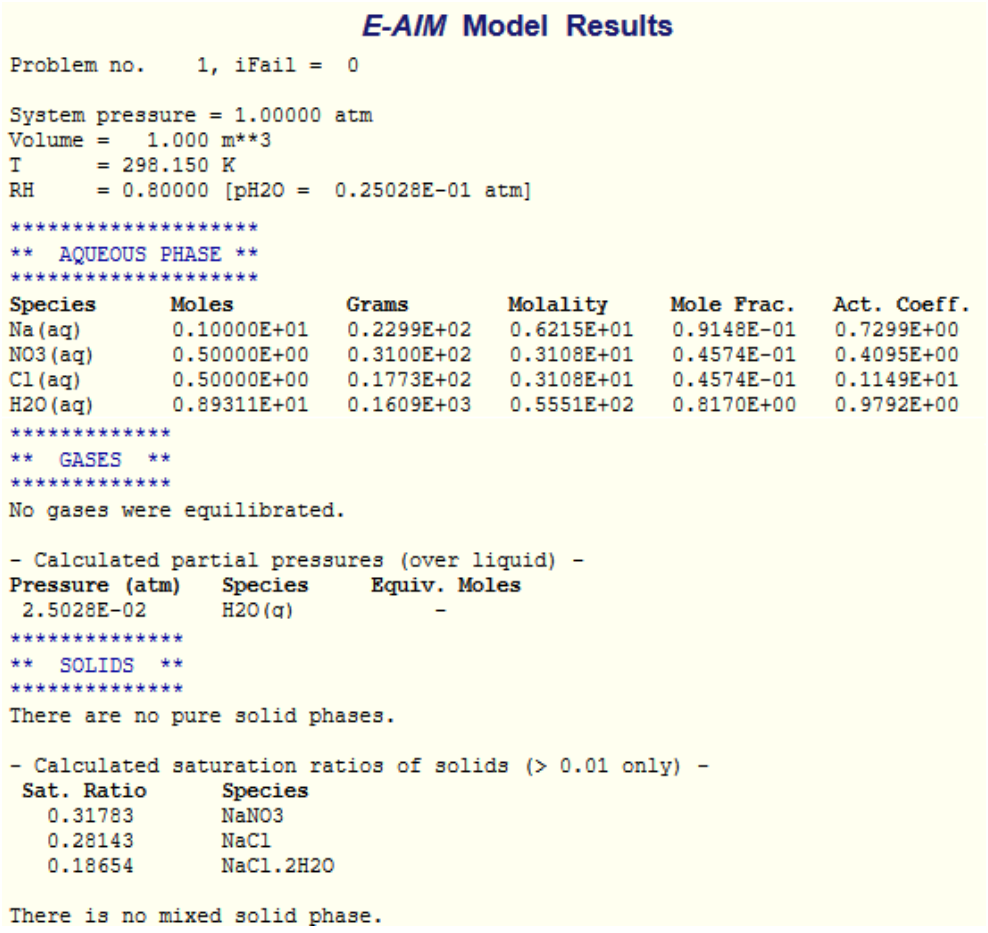

***E-AIM* Model Results**

```
Problem no.    1, iFail =  0

System pressure = 1.00000 atm
Volume =   1.000 m**3
T      = 298.150 K
RH     = 0.80000 [pH2O =  0.25028E-01 atm]

********************
**  AQUEOUS PHASE **
********************
```

Species	Moles	Grams	Molality	Mole Frac.	Act. Coeff.
Na(aq)	0.10000E+01	0.2299E+02	0.6215E+01	0.9148E-01	0.7299E+00
NO3(aq)	0.50000E+00	0.3100E+02	0.3108E+01	0.4574E-01	0.4095E+00
Cl(aq)	0.50000E+00	0.1773E+02	0.3108E+01	0.4574E-01	0.1149E+01
H2O(aq)	0.89311E+01	0.1609E+03	0.5551E+02	0.8170E+00	0.9792E+00

```
*************
**  GASES  **
*************
No gases were equilibrated.

- Calculated partial pressures (over liquid) -
```

Pressure (atm)	Species	Equiv. Moles
2.5028E-02	H2O(g)	-

```
**************
**  SOLIDS  **
**************
There are no pure solid phases.

- Calculated saturation ratios of solids (> 0.01 only) -
```

Sat. Ratio	Species
0.31783	NaNO3
0.28143	NaCl
0.18654	NaCl.2H2O

```
There is no mixed solid phase.
```

Fig. 3.4.3: E-AIM software - Model IV outputs [54]

3.5 Accelerated aging

When dealing with the set up of accelerated aging cycles, important considerations concern the parameters setting and the instrumental limits. On one hand, the parameters settings concern the possible variables that should be

set and controlled in the climatic chamber (i. e. temperature, relative humidity and their respective ramps and light exposure), defining suitable and realistic ranges; on the other hand, the instrumental limits refer to those operative ranges and to further limitations that are related to the design of the machine that is used.

3.5.1 Climatic Chamber

The climatic chamber used to perform accelerated aging was a Climacell111 (see Fig. 3.5.1), consisting in a stainless steel inner chamber of 54 cm x 37 cm x 53 cm, equipped with one shelf and connected to a water reservoir and to a thermostat.

Fig. 3.5.1: Climatic chamber Climacell 111

Even though the climatic chamber Climacell111 can vary its parameters between T -9,9°C and +99,9°C and RH 1 and 99%, in order to control both these parameters together there are further restrictions. The T and RH conditions in which both parameters result to be kept under control using the climatic chamber Climacell111 are the ones depicted in Fig. 3.5.2, if lighting is not concerned; therefore, the upper limit of RH is equal to 90% between T 10°C and 90°C, while the lower limit of RH is 10% between T 30°C and 90°C. In case UVA lamps are switched on to illuminate shelves, the range of controlled operating conditions is

further restricted [58]. The climatic chamber Climacell111 reaches primarily the set T, and on a second step it balances the RH up to the desired value; for this reason, a possible shift in the RH values and an induction time to recover have to be taken into account when setting cycles. A step-like program lead to a better fitting of the set values, with respect to long ramps that cover large T and RH intervals. During the ageing, only one shelf was put, in order to get the best conditions of homogeneity into the chamber. Samples were placed at the centre of the shelf in an area indicated by the constructors as the one in which conditions are homogeneous. Fan speed was set at its maximum (100) in order to achieve fast distributions of heat and humidity. The ageing cycle applied and the description of its setup are reported in the following paragraph.

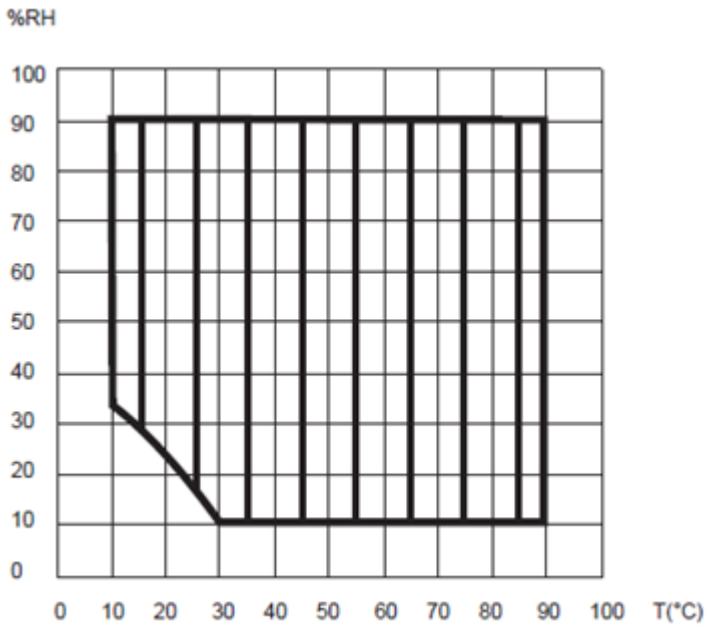

Fig. 3.5.2: Limit values for controlled operating conditions of Climacell111 [58]

3.5.2 Ageing cycle setup

In this study, the general set up of the aging cycle was tailored taking into account preliminarily the cycle for bronze aging proposed by Ferrari A. (2009) [52], discussed in paragraph 2.4 and summarized in Fig. 3.5.3, and implementing it to make it more suitable for our purposes and available instrumentation.

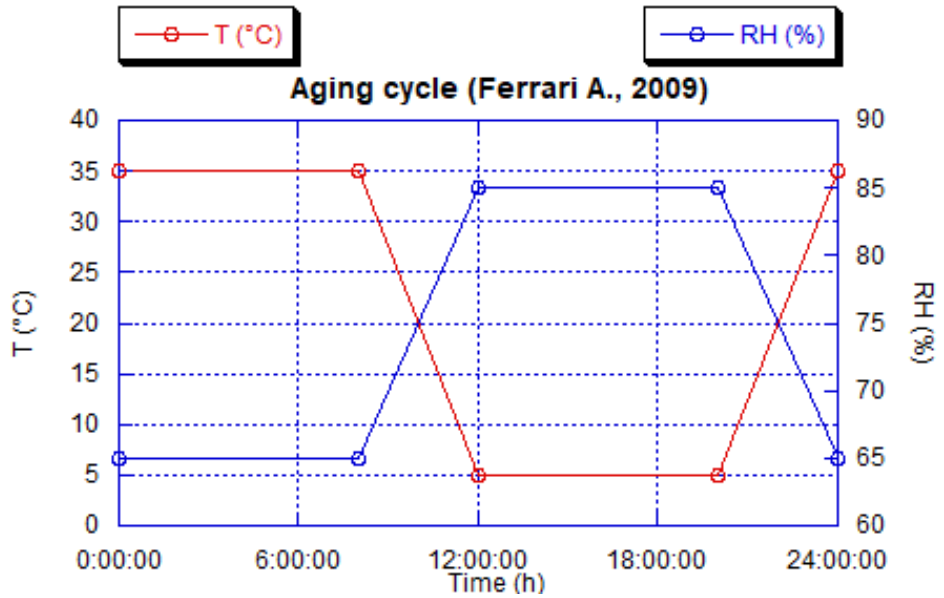

Fig. 3.5.3: Ageing cycle by Ferrari A. (2009) for bronze specimens [52]

Environmental data evaluation

In order to simulate realistic environmental values of T and RH to set during the aging cycles, data from the Regional Agency for Environmental Protection (Arpae) regarding the “Rimini Urbana” station were collected. In particular, T and RH recorded at 2 m height each hour were the investigated data over a range of 5 years at first [59].

By plotting T and RH recorded in the last 5 years, as it has been done in Fig. 3.5.4, it can be noticed that they show a very similar behaviour on an annual basis; for this similarities, it is possible to justify further and more specific consideration on the limit T and RH values to adopt just by treating the last year data (between 21/09/2016 and 21/09/2017). Further graphics to prove the similar tendencies of the last years’ parameters are shown in Appendix A.

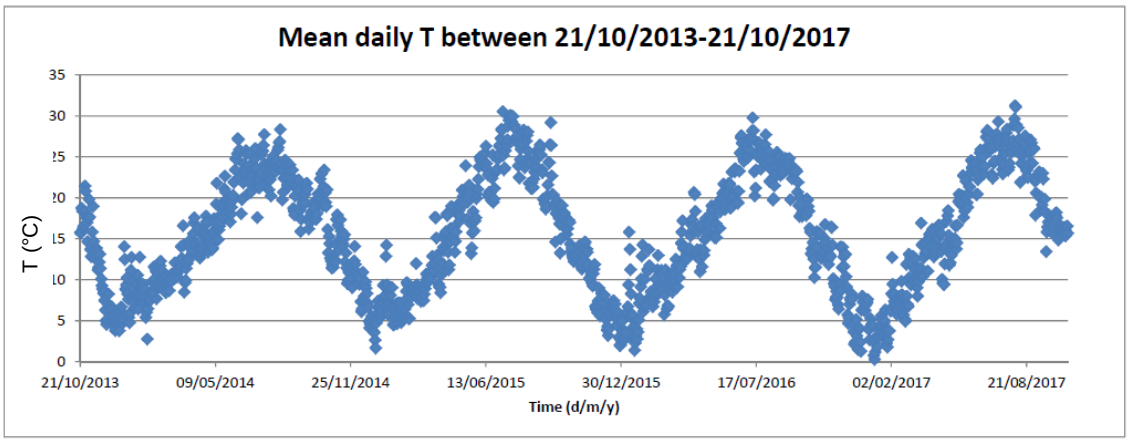

(a)

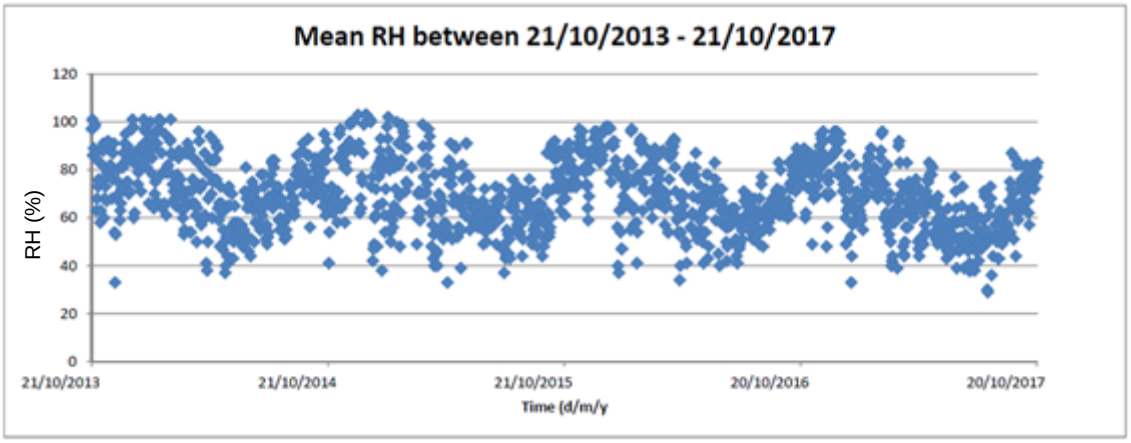

(b)

Fig. 3.5.4: a) Mean daily Temperature plot; b) Mean daily Relative Humidity plot from 21/10/2013 to 21/10/2017 based on Arpae data from “Rimini Urbana” station.

As the T and RH fluctuations of the last years were similar to each other, general considerations around T and RH limit values were drawn by Arpae data concerning a shorter period of time, lasting from 21/09/2016 to 21/09/2017; for convenience, data were split and considered in two different intervals of time, in order to draw two seasonal cycles: the autumn-winter (AW) one, from 21/09/2016 to 21/03/2017, and the spring-summer (SS) one, from 21/03/2017 to 21/09/2017. The minimum T and the maximum RH over the year occurred between November and January, while the maximum T and the minimum RH between June and August. Graphics of mean, minimum and maximum hourly T and RH, corresponding to the above cited periods, are shown in Appendix B. The limit values of T and RH, excluding less than 1% of data to ignore values which occurred just rarely, were extrapolated for the two periods. Aiming to

simulate the daily cycle of T and RH in an accelerated version, T and RH curves were plotted focusing on 4 days, respectively on solstices and equinoxes in 2017. As shown in Fig. 3.5.5 and in all the other cases presented in Appendix C, with features more or less pronounced, in the early morning T is low and RH is high; then, when T raises, RH diminishes, until a plateau of the two parameters during the central daylight hours; approaching to the evening, T decreases again and RH raises and they keep almost constant again during the central hours of night

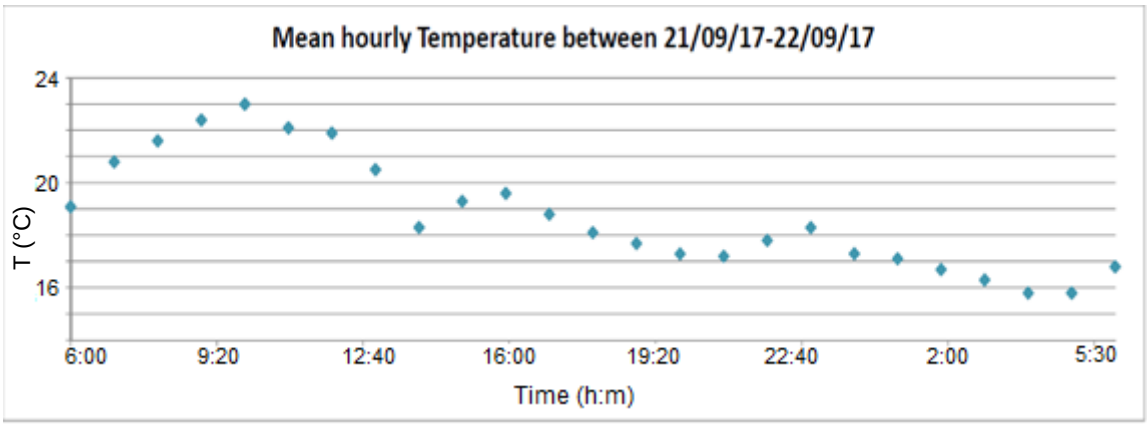

(a)

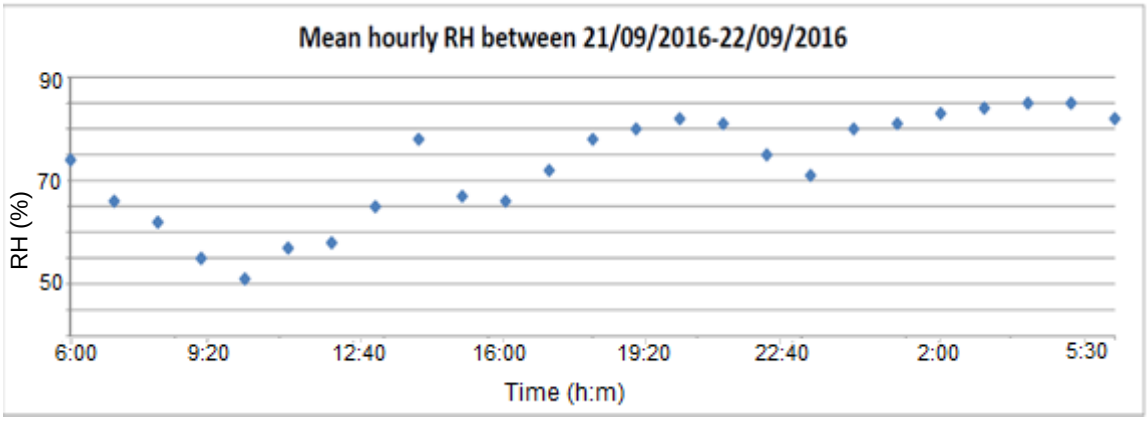

(b)

Fig. 3.5.5: Arpae data on 2017 autumn equinox relative to a) mean hourly T; b) mean hourly RH

Ageing cycles definition

Two seasonal cycles referring to the Autumn-Winter (AW) period and to the Spring-Summer (SS) one were set and are displayed in Fig. 3.5.6 and Fig. 3.5.7. The maximum T corresponds to the lowest RH and viceversa, as in the aging cycle proposed by Ferrari A. (2009) [52] and as observed during the daily T and

RH fluctuations recorded by the Rimini Urbana station [59]. T and RH minima and maxima were chosen according to the Arpae data presented in Appendix B. These two cycles were not applied in this study, but they represented a preliminar step for the set up of the effective general cycle that was used.

- Autumn-Winter cycle

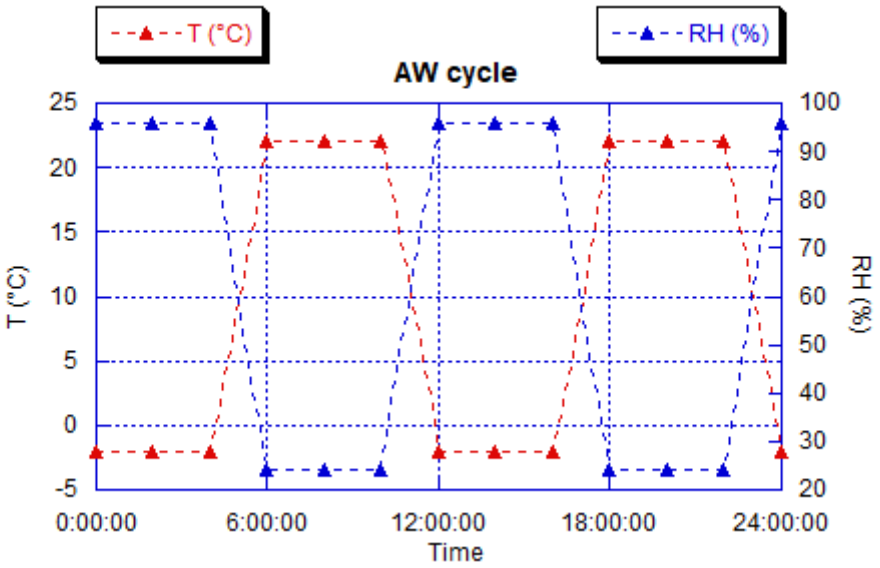

Fig. 3.5.6: Autumn-Winter cycle

- 4 h at T -2°C and RH 96%
- 2 h ramp T +6°C / 30 min and RH -12% / 30 min
- 4h at T 22°C and RH 24%
- 2 h ramp T -6°C / 30 min and RH +12% / 30 min
- Repetition since the first step

- Spring-Summer cycle

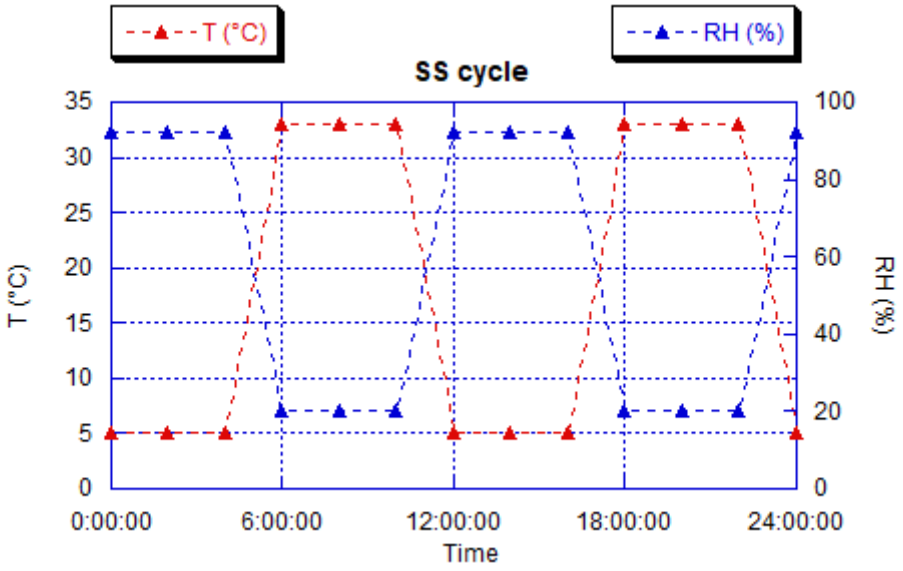

Fig. 3.5.7: Spring-Summer cycle

- 4 h at T 5°C and RH 92%
- 2 h ramp T +7°C / 30 min and RH -18% / 30 min
- 4h at T 33°C and RH 20%
- 2 h ramp T -7°C / 30 min and RH +18% / 30 min
- Repetition of the cycle from the first step

After the set up of these seasonal cycles, by averaging the limit conditions obtained in the AW and SS cycles, a general aging cycle, which is displayed in Fig. 3.5.8 and described below, was used to age samples in this study. The minimum RH to reach was set to a higher value taking into account that the salts used in this study were solid below RH 27% at T 33°C, and therefore it did not matter so much a small RH minimum variation in terms of deliquescence, while it could allow the machine to work better, providing more regular steps during the ramps and fitting better in the operative ranges to control both T and RH (see Fig. 3.5.2). Supplementary tests were done in order to ensure the capability of the chamber to control T and RH conditions even out of the declared operative ranges and are presented in paragraph 4.2; however, in order to not stress too much the machine, the minimum T of 5 °C was restricted to shorter periods than 4 hours of plateau. The frosting option and the light exposure were not considered at this point; however, a general cycle concerning also the frosting

option was drawn and is reported in Appendix D together with light exposure hints for future applications.

- General cycle applied in the study

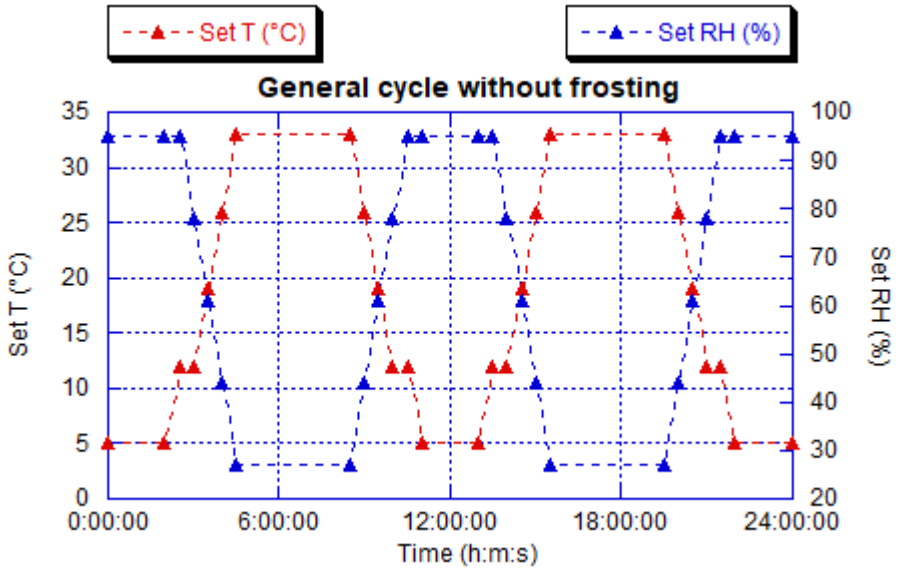

Fig. 3.5.8: T and RH oscillations in the general daily cycle

- 2 h at T 5°C, RH 95%
- 1 h ramp to reach T 12°C, RH 95%
- 30 min at T 12°C and RH 78%
- 1 h 30 min ramp at T +7 °C / 30 min, RH -17% / 30 min
- 4 h at T 33 °C, RH 27%
- 1 h 30 min ramp at T -7 °C / 30 min, RH +17% / 30 min
- 30 min at T 12 °C, to reach RH 95%
- 1 h ramp to reach T 5°C, RH 95%
- Repetition of the cycle from the first step

This general daily cycle was repeated for three weeks in total; after this period, ATR-FTIR analyses were performed on residues onto the “dry” single salt samples before pickling, while pickling and successive AAS analyses were performed onto the pickling solutions from the “wet” single salt samples.

In the successive paragraphs, the accelerated ageing range of time will be divided into steps labelled as:

- “t0”, referring to the time at which the salt residues were spread, underwent to deliquescence in the case of “dry” specimens, and dried before starting the accelerated ageing procedure;
- “t1”, referring to the time after one week of accelerated ageing into the climatic chamber;
- “t2”, referring to the time after two weeks of accelerated ageing into the climatic chamber;
- “t3”, referring to the end of the accelerated ageing procedure, corresponding to three weeks into the climatic chamber.

3.6 Pickling procedure

After three weeks of aging into the climatic chamber, single salt samples were pickled according to the following tested procedure [60].

For the wet-treated samples, masks with inner area 1 cm x 1,1 cm (see Fig. 3.6.1) were preliminarily applied onto the surfaces, in order to ensure that no removal of the lacquer was going to occur and that the pickled area was the same for every specimen. Then, a series of washings alternating distilled water and HCl 37% were done, applying the liquids using a pipette: 2 mL H_2O; 2,5 mL HCl; 2 mL H_2O; 2,5 mL HCl; 2 mL H_2O. Samples were weighted at different steps of the pickling and two acid washing resulted sufficient as no significant differences in weight loss were detected between them. After the mask removal, glue residues were cleaned with acetone soaked cotton swabs. The pickling solutions were brought up to 20 mL volume using distilled water and stored in HDPE bottles at 4°C for the following metal analyses.

The pickling of the dry-treated samples was similar to the “wet” ones, but additionally specimens were sonicated in beckers with 20 mL distilled water for 60 s. Then, masks to cover borders were applied to these samples too. The same alternating washings that were performed for the “wet” samples were done. Eventually mechanical cleaning using acetone soaked cotton swabs was performed.

Fig. 3.6.1: Pickling procedure performed onto the “wet” sample treated with NaCl: detail of alternating HCl 37% and distilled water washings

3.7 Analytical methodologies

Each week from the beginning to the end of the ageing, all the samples were checked by SEM-EDX and Raman spectroscopy, together with pH measurements and colorimetric analyses on the specimens where wet depositions were performed.

ATR-FTIR spectra were recorded on dry residues at the end of the aging procedure. After pickling, line profiling was done onto the single salt specimens (both “wet” and “dry” ones). AAS was done onto the pickling solutions of the “wet” specimens.

3.7.1 Color measurements

Color measurements were performed using the 3D color space CIELAB as defined by the Commission International de l’Éclaraige (CIE). The three axes of this space are constituted by L* (luminosity), that ranges between 0 and 100, a*

(green-red), between -500 and 500, and b* (blue-yellow), between -200 and 200 (see Fig. 3.7.1), and each color can be identified as a vector E*. For the evaluation of the deterioration occurred on a sample, the interesting parameter to monitor is not the E* vector itself, but its difference ΔE*, defined in Eq. (5), to compare the original color of a material with respect to its evolution [60]. Despite the fact that the limit for ΔE* is commonly fixed to higher values than 3 to state that color changes are visible on artworks [61], the threshold of perceptibility of color changes can differ on person. Considerations on ΔL*, Δa* and Δb* can allow to interpret better which component varied and resulted in color modifications.

$$\Delta E^* = \sqrt{(\Delta L^*)^2 + (\Delta a^*)^2 + (\Delta b^*)^2} \tag{5}$$

Using a Datacolor D400 UV-Vis Spectrophotometer, color measurements were performed on a sample were single salt solutions were dropped; analyses were carried out before any salt deposition, after the salt deposition and at the end of the aging, in order to retrieve possible colour changes on the sample surface. The geometry of the instrument is d/8°, which allows both the inclusion (SCI) or the exclusion (SCE) of the specular reflected radiation; the SCE modality was chosen in this study, together with the CIE standard illuminant D65 (simulating solar radiation) and 10° as standard colorimetric observer. Thanks to the same instrument, also reflectance data were obtained.

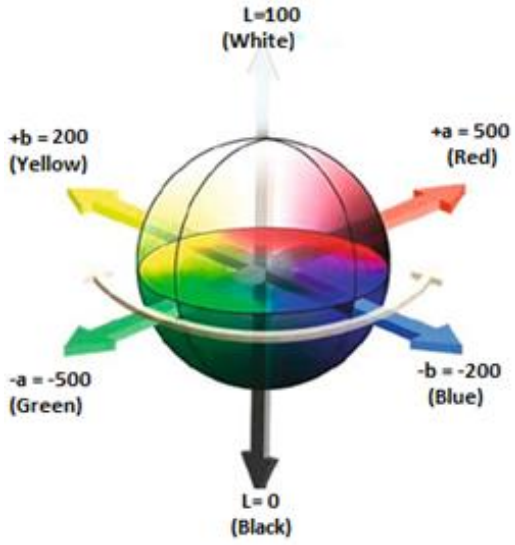

Fig. 3.7.1: CIELAB space representation [62]

3.7.2 SEM-EDX

Scanning Electron Microscopy (SEM) is an analytical technique to observe the sample surface morphology and to get some hints about its composition. The achievement of information using the SEM is related to the ejection of electrons from the sample thanks to the interaction with an electron beam: from the primary beam bombardment, low energy secondary electrons (SE), backscattered electrons (BSE), Auger electrons and X-rays are generated (see Fig. 3.7.2).

The two common types of electrons used to get a signal in SEM are SE and BSE: SE correspond to an inelastic scattering, BSE to an elastic scattering; also Auger electrons and X-rays can be used to achieve information on the chemical composition of the sample, if a specific detector is present.

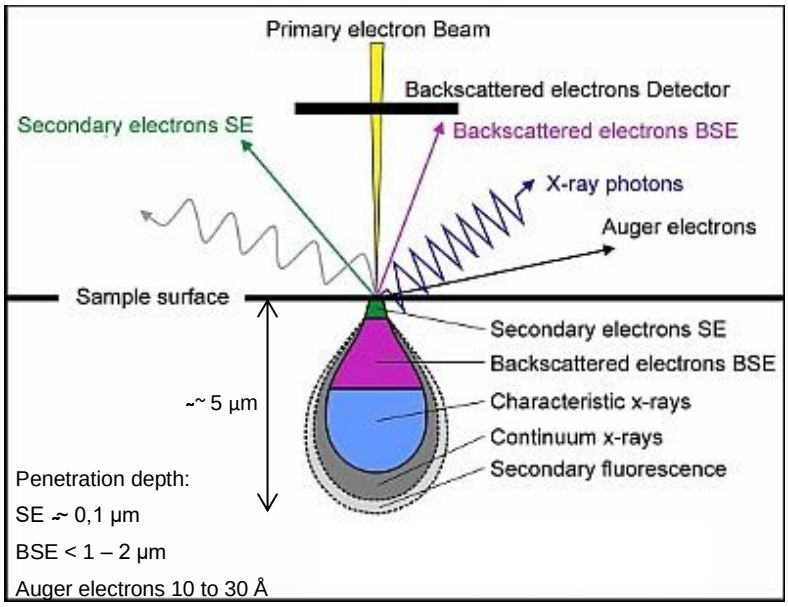

Fig. 3.7.2: Electrons and radiation arising from the interaction between the incoming beam and matter in SEM [63]

The Scanning Electron Microscope is constituted by four main parts, which are schematized in Figure 3.7.3:

1) the *optical-electronic system*, which includes the electrons source placed at the top of the displayed column; the electrons can be produced in thermal emission or field emission and, once they are generated, they are oriented to hit the sample in the desired area. Their path is defined by

lenses and magnetic coils, which deflect the beam to scan the desired area of the sample.

2) the *sample-holder chamber*; which consists in a compartment at the electron column where specimens can be placed on a mobile sample holder.
3) the *detectors*, that have to collect the signals produced by the interaction of the beam with the sample surface; a Variable Pressure Secondary Electrons (VPSE) detector catches the SE, while a quadrant semiconductor diode is used for the BSE.
4) the *vacuum system*, that has the task to prevent the deterioration of the electron, because of the electron production at high temperatures (~2700-2800 K), and to ensure the passage of electrons enhancing their mean free path.

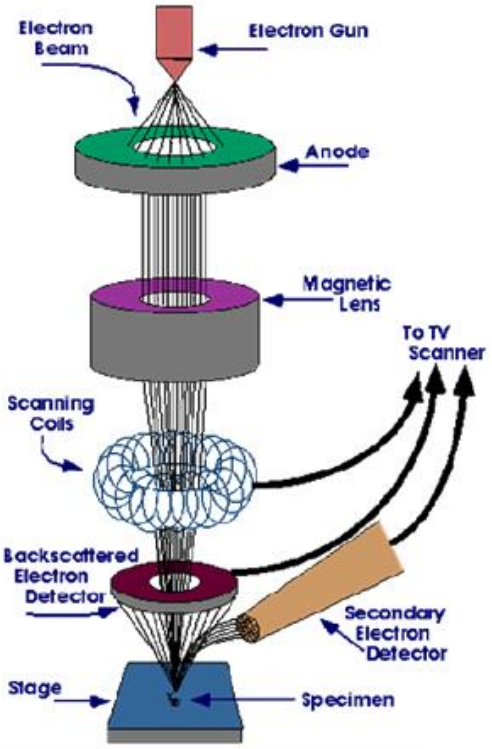

Fig. 3.7.3: SEM-EDX scheme [64]

All the parts in which the passage of electrons happens are isolated and in high vacuum conditions to perform the analysis. Each pixel of the image that appears on the screen is synchronized with the position of the beam on the sample in the microscope, leading to a simultaneous scan that can be monitored onto the screen; the resulting image is a distribution map of the signal intensity that is

emitted from the scanned area of the specimen. The magnification of the image comes out from the ratio between the amplitude of scan on the sample and the amplitude of scan onto the screen. [63]

In order to perform the analyses required in this study, the instrument that was used was a Variable Pressure Scanning Electron Microscope (VP-SEM) ZEISS EP EVO 50, equipped with SE and BSE detectors. Pressure ranges include: High Vacuum, ~10-4 Pa; Variable Pressure, 10-1000 Pa; Environmental Pressure, <3000Pa. Images were recorded in High Vauum conditions. The electron beam was kept focused at 8,5 mm from the surface. As non-conductive materials allow the accumulation of static electric charges, their image information looks deteriorated, therefore, when Teflon was exceeding from the borders of the specimens, the part in excess on the bottom face was removed in order to enhance the contact between bronze samples and stage. Applying an accelerating voltage of 20 keV, an EDX probe Oxford Instruments INCA X-act Penta FET® Precision [z>4 (Be), resolution 129eV (MnKa @ 2500cps)] was used to obtain chemical information of the samples. The EDX probe can be controlled via a software (Software Inca Microanalysis Suite version 4.15 – issue 18 – service pack 5) that recognizes peaks automatically referring to internal standards for semi-quantitative analysis, and it allows to analyse points, lines, areas and to perform mapping.

3.7.3 Raman spectroscopy

Raman spectroscopy is a non-destructive technique that probes inelastic scattering events promoted by monochromatic light, which interacts with molecular vibrations, phonons or other excitations in the system, resulting in a shift of the energy of the laser photons and providing information on the occurring modes that are Raman active.

Typically a sample is illuminated with a laser beam in the visible, near IR or near UV range, and the electromagnetic radiation is collected with a lens and sent through a monochromator. As shown in Fig. 3.7.4, the excitation by the incoming beam promotes the molecule into a virtual energy state for a short time (around

10^{-12} s) before the photon emission. The elastic scattered radiation at the wavelength corresponding to the laser line (Rayleigh scattering) is filtered out by either a notch or edge filter, while the rest of the collected light is dispersed onto a detector. In order to keep the total energy of the system constant after the molecule reaches a new rovibronic state, the scattered photon shifts to a different energy; this energy difference is equal to that one between the initial and final rovibronic states of the molecule, leading, in the case of inelastic scattering, to a Stokes shift (if the final state is higher in energy than the initial state) or to an anti-Stokes shift (if the final state is lower in energy than the initial one). By the interaction of the electron cloud of the specimen with the electric field of the incoming beam, an induced dipole moment is created within the molecule based on its polarizability, which influences the intensity of the Raman shift proportionally. The Raman spectrum (see Fig. 3.7.5) consists of an unshifted intense component with respect to the initial frequency (Rayleigh scattering), corresponding to photons elastically scattered, and the Stokes and the anti-Stokes lines, perfectly symmetric respect to the Rayleigh line. Usually only the Stokes lines are considered in chemical analysis because of their higher intensity, considering that, on the basis of the Boltzmann distribution law, at near room temperature the ground vibrational level is the most populated one.

In order to record Raman signals, the Raman spectrophotometer consists of several parts shown in Fig. 3.7.6: one or more lasers to create the incoming beam, lenses for the microscope, filters (most commonly notch or edge ones), splitting devices, diffraction grating to bend the Raman shifted light according to the wavelength, detector, computer, microscope [65].

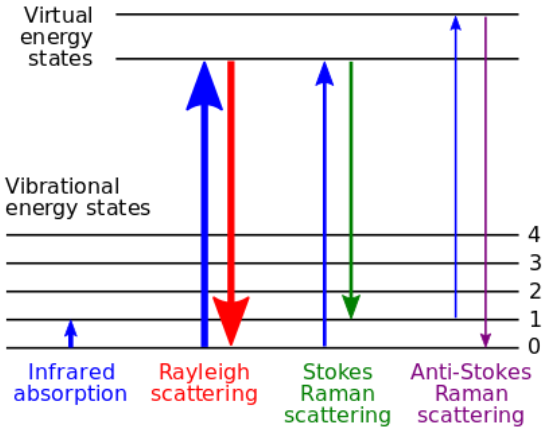

Fig. 3.7.4: Transitions associated with elastic and inelastic scattering [66]

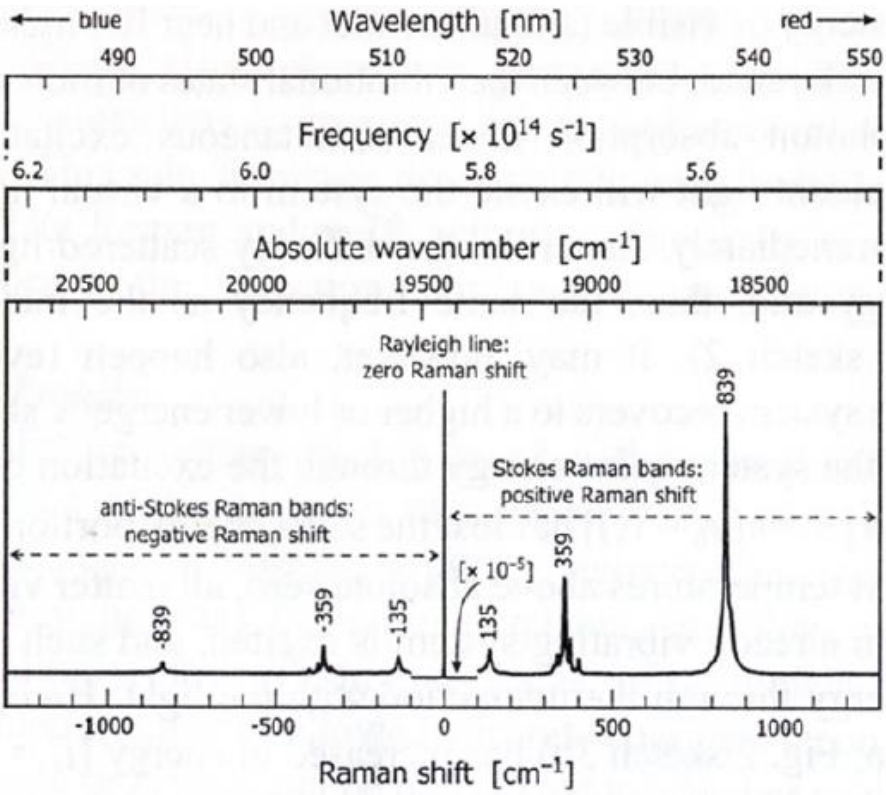

Fig. 3.7.5: Raman spectrum, an example [67]

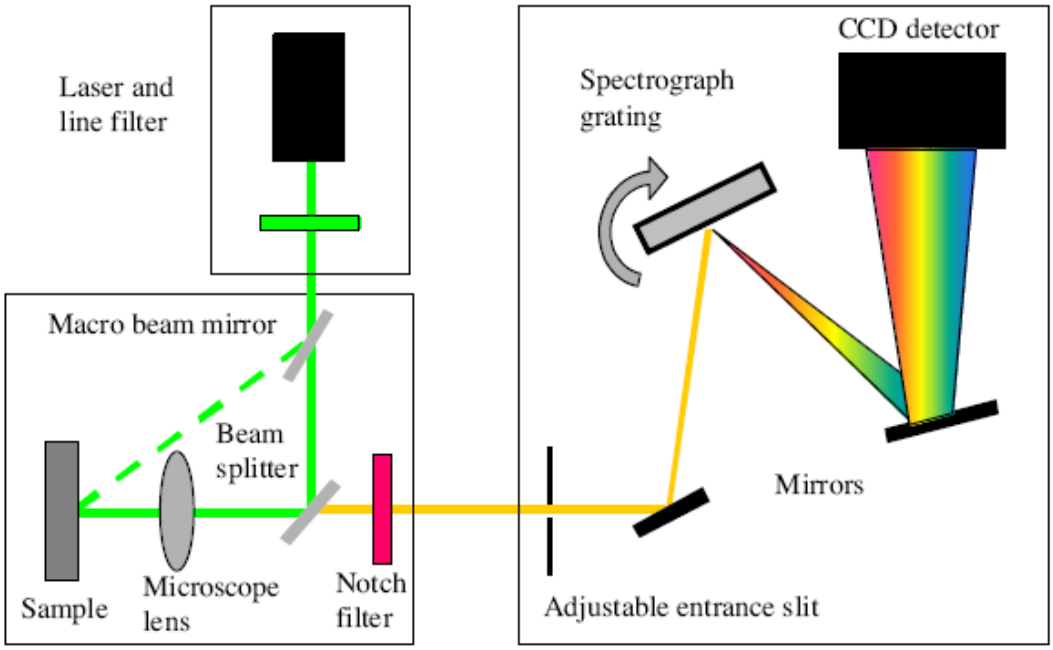

Fig. 3.7.6: Raman spectrophotometer scheme [68]

In this study, a Renishaw Raman Invia instrument, coupled to a Leica DMLM microscope (objectives 5x, 20x, 50x), was used, performing the analyses with an

Ar^+ 514,5 nm laser with power of 30mW reduced at 5 or 10% depending on the circumstances. Further components of the instrument concern an edge filter, used to cut off the Rayleigh scattering, a monochromator (1800 lines/mm) and a Charge-Coupled Device (CCD) detector thermoelectrically cooled (203 K). Every spectrum was constituted by 4 accumulations, requiring 10 s for each of them, with spectral resolution of 2 cm^{-1}. The wavenumbers that were investigated ranged between 100 and 2000 cm^{-1} except for some sulphate samples, for which the range was extended up to 4000 cm^{-1} in order to get information on the hydration degrees of some compounds.

3.7.4 ATR-FTIR

The Fourier Transform IR (FTIR) is a spectroscopic technique that allows to obtain infrared spectra via a mathematical elaboration of the raw data collected from the interaction of a radiation flux with a sample, that displays variations of its dipole moment upon vibrational motions of its atoms, when resonance conditions are met. As shown in Eq. (6), vibrational frequencies are inversely proportional to the square root of the reduced mass, therefore heavier atoms signals will be found at lower frequencies. The common units used in IR spectroscopy are wavenumbers, expressed in cm^{-1}, rather than frequencies, even though they are proportional to each other; relations between frequencies, wavelengths and wavenumbers are summarized in Eq. (7).

$$\bar{\nu} = \frac{1}{2\pi c}\sqrt{\frac{k}{\mu}} \tag{6}$$

$$\boldsymbol{E = h\nu = hc/\lambda = hc\bar{\nu}} \tag{7}$$

where ν is the frequency, c is the light velocity, k is the force constant, μ is the reduced mass, E is energy, h is Planck's constant, λ is the wavelength, $\bar{\nu}$ is the wavenumber.

During this studies, this kind of analysis was performed in Attenuated Total Reflectance (ATR) mode, which uses the internal reflections of a crystal, that has

a higher refractive index than the specimen, in order to generate an evanescent wave (see Fig. 3.7.7) which, in the spectral region of medium infrared, helps to identify some features of the sample. All the energy is then reflected; however, the beam penetrates slightly beyond the reflecting surface and then returns; placing a material in direct contact with the reflecting surface, the beam loses energy at those wavelengths that the material can absorb thanks to an interaction with the penetrating beam. [69]

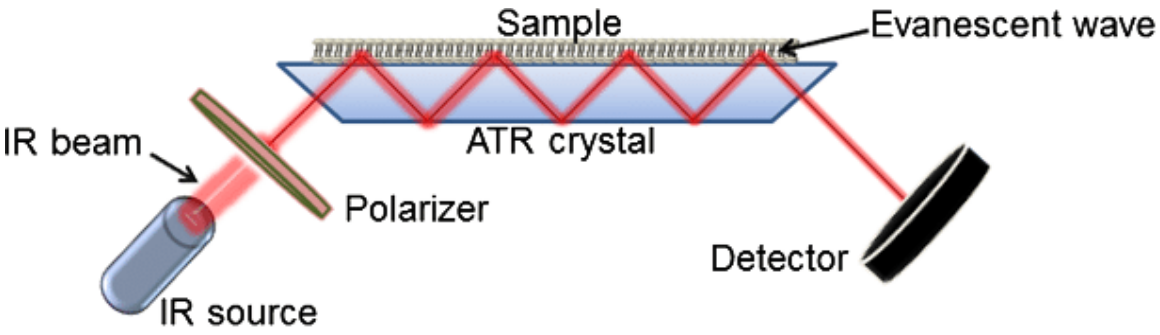

Fig. 3.7.7: ATR-FTIR instrument scheme [70]

This methodology does not require sampling and it is referred as a micro- or even non-destructive technique; microdestruction can arise from the pressure that is required to keep in close contact sample and crystal and to get the conditions to record nice quality spectra. The penetration of the radiation in ATR modality depends on its wavelength, its incident angle and the refractive index of the two media, and it can be reduced up to 2 μm [69].

In this study an FT-IR Alpha Bruker instrument, equipped with a SiC (Globar type) source and a Rocksolid interpherometer, was used; samples were placed in contact with a diamond crystal to obtain the external reflection, and the corresponding spectra were collected in transmittance mode between 4000 and 400 cm^{-1}, with spectral resolution of 2 cm^{-1} and 32 scans. The detector that recorded the signals is a deuterate triglycine sulphate (DTGS).

3.7.5 Line Profiling Analysis

Line profiling analysis consist in the measurement of the surface profile in terms of roughness. In this study a contact profilometer equipped with a diamond stylus was used: the stylus is moved vertically in contact with a sample and then moved laterally across the sample for specified distance and contact force. The stylus senses the surface height via mechanical contact with sub-nanometric precision, while the lateral resolution is limited by the stylus tip size, which can be as small as 100 nm. Small surface variations in the vertical displacement of the stylus are plotted as a function of position, ranging from nanometric to millimetric features. The height position of the diamond stylus generates an analog signal which is converted into a digital signal, which is stored, analyzed, and displayed. The radius of diamond stylus ranges from 20 nanometres to 50 µm, and the horizontal resolution is controlled by the scan speed and data signal sampling rate. The stylus tracking force can range from less than 1 to 50 milligrams. Vertical resolution is typically sub-nanometer as well. Because the stylus is in contact with the surface, this method is not sensitive to surface reflectance or color. Contact profilometry is a direct technique, therefore it not require any modeling. [71] For a given test line, the roughness (named Wt) was defined as the arithmetical mean of peaks above and under the baseline. [72]

In this study a Tester T2000 with an inductive transducer was used. The instrument is equipped with a diamond tip that is connected solidally to a thin stick; on the superior part of the stick there are ferrite plates at a given distance from coils, where an alternating current circulates. Varying the distance of the plates with respect to the coils, because of the surface roughness, the inductance in the coils changes and therefore the alternating tension, that is translated by the Tester into a profile according to the input algorithms. The surface parameters that were achieved are the ones listed in Table 9.

Table 9: Line profiling output paramenters

Parameter	Definition
Rmax (Maximum single depth)	Maximum amplitude, within l_m, of the filtered profile
Rt (Maximum depth)	Distance between the tangent to the peaks and the tangent to the holes, within the length of the filtered profile

3.7.6 Atomic Absorption Spectroscopy

Atomic Absorption Spectroscopy (AAS) is an analytical technique that allows to determine qualitatively the presence and quantitatively the concentration of chemical elements in a sample considering the absorption of light by free atoms in the gas state. The analytical application is based on the fact that metal atoms absorb strongly at discrete, element-characteristic wavelengths, producing excited states. Concentration and absorbance result to be correlated according to Beer-Lambert's law (Eq. 8):

$$A = \log (I_0/I) = \varepsilon_\lambda dM \tag{8}$$

where A is the absorbance, I_0 is the intensity of the incoming radiation, I is the intensity of the beam after its passage through the sample, ε_λ is the molar absorption coefficient, d is the geometrical path travelled by the radiation across the sample and M is the solution molarity. [73]

The main units that compose an AAS instrument are the following ones, displayed in Fig 3.7.8:

1) *Radiation source*, constituted by a hollow cathode (HDL) or an electrodeless discharge (EDL). HDL lamp is constituted by a glass cylinder filled with argon in which a little target of the element of interest is placed, so that ions are accelerated by applying an electric potential difference to let them then collide onto the cathode, causing the ejection of metal atoms from the surface. These atoms tend to return to the ground state by emitting radiation with the wavelength characteristic of the

element. The EDL is a ceramic tube filled with low argon, in which a quartz bulb containing the element to be analysed and surrounded by a radiofrequencies (RF) generator is placed. The energy vaporizes the element and excites atoms that emit their characteristic spectrum to return in the ground state.

2) *Chopper*, (not present in all the instruments) to split the radiation beam and get both reference and analyte signals; the reference signal consists in the spectrum of the metal that constitutes the hollow cathode or, alternatively, in a correction via Zeeman effect, which permits a more precise background subtraction and therefore allows to lower the detection limit thanks to a modulated magnetic field (0,8 Tesla) applied to the atomizer and switched on automatically during the atomization step only. This magnetic field allows the splitting of the signals and a successive subtraction of what is not within the expected region of the spectrum.
3) *Atomizer*, which can be a photometer flame burner (F), this assembly comprises of nebulizer to get a fine aerosol from the initial sample, or a graphite furnace (GF) with electrothermal atomization.
4) *Monochromator*, to discriminate wavelengths after the sample crossing and to eliminate emitted light interferences;
5) *Detector*, usually constituted by a photomultiplier tube.

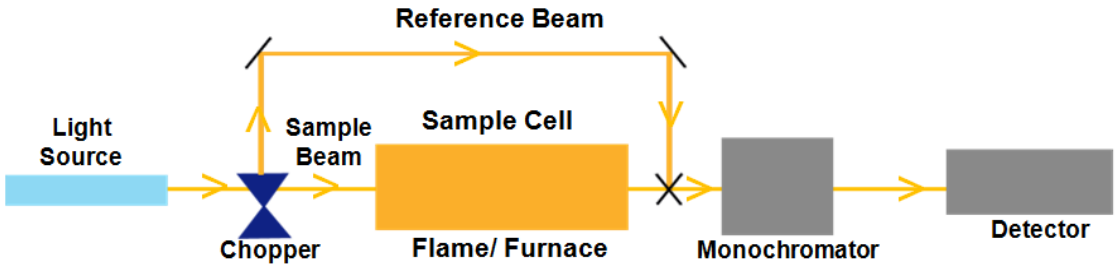

Fig. 3.7.8: Atomic Absorption Spectroscopy equipment scheme [74]

The beam traverses the flame (or the graphite furnace), it is focused on the entrance slit of a monochromator and read by the detector. Several elements can be analysed both in liquid and solid state choosing the most suitable atomizing method. Some elements are not detectable in flame, maybe because

of the formation of oxides, but they can be analysed by AAS by changing the flame type or by using other atomizer methods are used. On the other hand, some elements, as zinc, can contaminate easily furnaces, and therefore are analyzed preferentially by flame.

In this study a PerkinElmer HGA 900 (Fig. 3.7.9) with Deuterium background correction was used for analyzing Cu and Zn by F-AAS. A multi-element hollow cathode lamp (Cu-Fe-Mn-Zn) and an air/acetylene flame were used. Samples are input manually.
For the GF-AAS analyses of Pb and Sn, a PerkinElmer PinAAcle 900Z instrument, equipped with an AS 900 autosampler, was used. The background correction was performed via longitudinal AC Zeeman effect. Electrodeless Discharge Lamps where used for Pb and Sn determination. Calibration curves were plotted by measuring absorbances and deriving concentrations of a series of standards, listed in Table 10. Data were processed with WinLabAA Furnace/Flame Software; all the processed data had a relative standard deviation (RSD) below 10%.

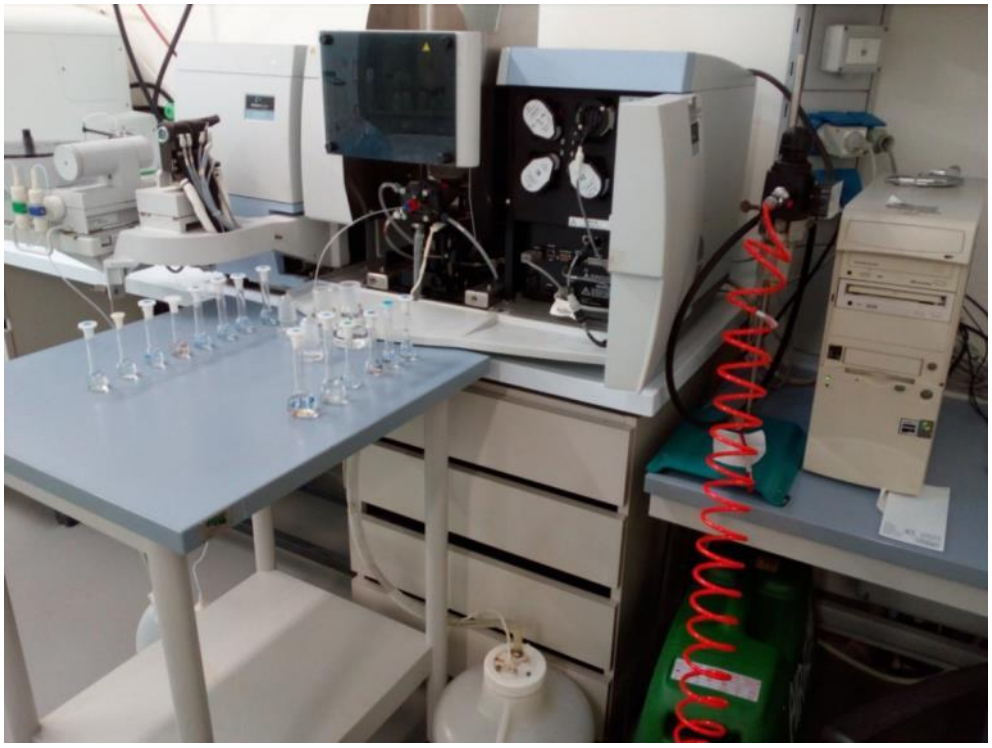

Fig. 3.7.9: PerkinElmer HGA 900 for AAS

Table 10: Calibration curves data

Element (λ in nm)	Standards (ppm)	Calibration curve slope	Correlation coefficient (R^2)
Cu (324,75)	0,5 – 1 – 2 – 5 – 10	0,07081	0,999594
Pb (283,31)	0,0025 – 0,005 – 0,01 – 0,02	0,00299	0,999931
Sn (286,33)	0,01 – 0,02 – 0,05 – 0,1	0,00101	0,999593
Zn (213,86)	0,1 – 0,3 – 0,5 – 1	0,020436	0,999910

4 Results and discussion

This chapter is divided in sub-sections regarding validation tests (section 4.1), macroscopic modifications of the specimens during the ageing procedure (section 4.2), surface analyses for monitoring the evolution of salts and corrosion products onto the bronze samples (section 4.3) and final tests after pickling the specimens (section 4.4 regarding AAS and section 4.5 regarding line profiling analyses).

4.1 Preliminary validation tests

Preliminary validation tests have involved:

6) the climatic chamber to use for the ageing procedure, in order to establish the effective compatibility of the instrument with the set T and RH parameters and the ranges of time to arrange them (section 4.1.1);
7) the experimental verification of the theoretical calculations regarding the DRH of salts (section 4.1.2);
8) the choice of the proper unit of measurement for the establishment of the amounts of substances to spread for suitable comparisons (section 4.1.3).

4.1.1 On the climatic chamber

The general cycle without frosting was chosen to begin these studies on the PM induced corrosion. As the T and RH limits for the general cycle without frosting were a bit out of the operating limits of the chamber in order to have control of both parameters, validation tests were done to assess if the chamber was really not able to cover these values or if just a poor deviation was observed. Two cycles were performed by placing a thermo-hygrometer into the climatic chamber: one cycle was performed leaving the RH off at T 5°C (Fig. 4.1.1), the other one switching RH on at 95% at T 5°C (Fig. 4.1.2). In Fig. 4.1.1 RH measurements by the climatic chamber are not displayed because they are not provided when the RH control parameter is set on “off”; however, according to the thermo-hygrometer data, the chamber seems to reach by itself the 95% RH at 5 °C; this means the machine should not be stressed if the desired RH is set in the program, as the same behaviour is displayed in the Fig. 4.1.2. With RH in

off, it implies around 20 minutes to reach RH 95%, while with set RH it reaches it in 10 minutes.

An additional feature of the chamber was tested: during the cycle in Fig. 4.1.2, around 9.50 h, the door of the chamber was opened for around 20 seconds: as it can be observed by the recorded RH values, the chamber can compensate and restore the set RH in around 5 minutes, which is a short time compared to the time ranges for ramps and plateaux in the general aging cycle that was chosen; this is an interesting feature of the machine, because this means that not significative perturbations happen in case the chamber was opened during the aging cycles for monitoring and taking photos of the specimens, if these operations are done fast.

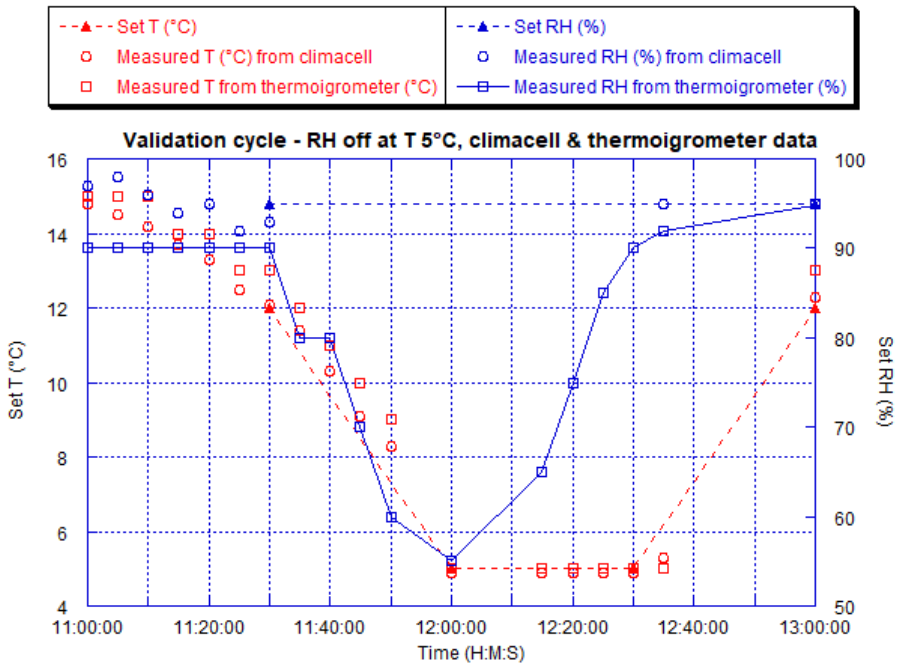

Fig. 4.1.1: Validation of RH control in a part of the general cycle without frosting out of the limit controlled operating conditions – RH off in the climatic chamber settings

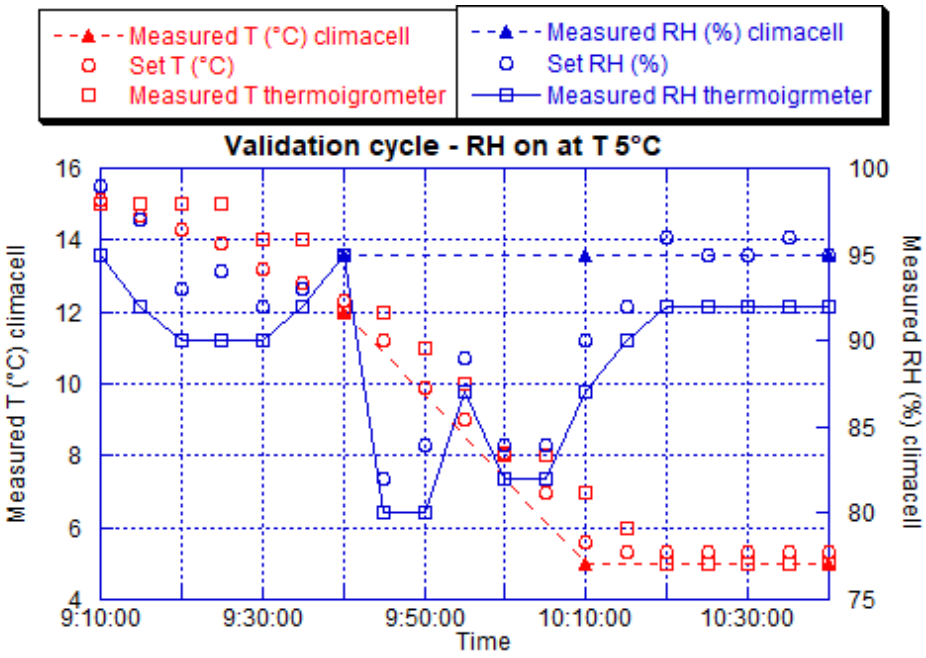

Fig. 4.1.2: Validation of RH control in a part of the general cycle without frosting out of the limit controlled operating conditions – RH on in the climatic chamber settings

4.1.2 On the DRH of salts

By the validation test of the DRH predictions, it was observed that the predictions of E-AIM software were matching with the experimental observations, in the range ±3% with respect to the theoretical DRH that was tested.

DRH values at different T (fitting in the range of T that is set in the general cycle) are reported in Fig. 4.1.3 for each salt considered in a system by itself, finding almost perfect match between DRH values by E-AIM and by other sources in literature [28,75].

Therefore, we can assume that all the salts on the single salt specimens are in solution when RH is above 95% except for Na_2SO_4, which undergoes to deliquescence below 95% only when T is higher than 25°C; on the other hand, all the salts are solid when RH is 27%. According to these results, we expect the salts on the single salt specimens to undergo to 4 deliquescences and recrystallizations per day, unless they react with the substrate forming corrosion products, that than have different solubility and may even not display a DRH.

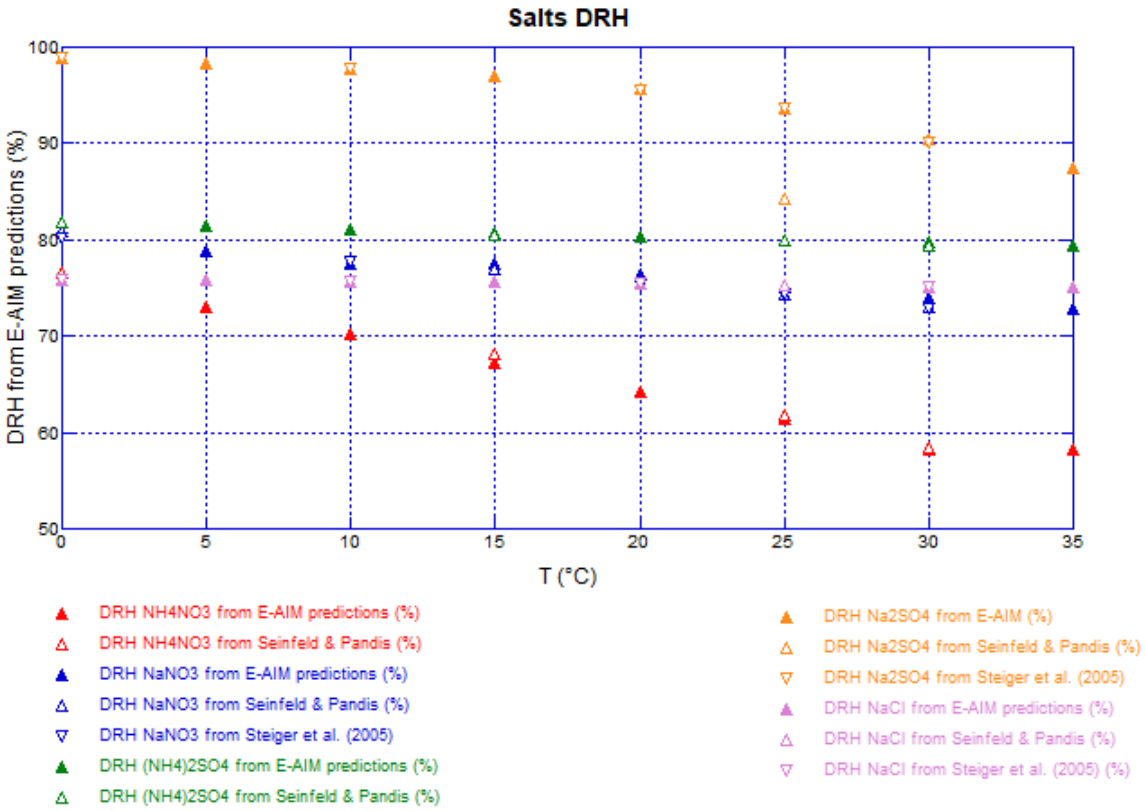

Fig. 4.1.3: DRH comparison between E-AIM (Model IV) predictions and literature data [28,75]

Regarding the ternary system in which NaCl, $NaNO_3$ and Na_2SO_4 were input, according to E-AIM predictions (shown in Table 11) all the species undergo to deliquescence together at T 12°C and RH 95% and at T 19°C and RH 61%, therefore sulphates perform 8 deliquescences per day, while chlorides and nitrates only 4, but remaining in solution for a longer time.

Table 11: Solid phases during the general aging cycle steps for the ternary system (NaCl, $NaNO_3$, Na_2SO_4)

T (°C)	RH (%)	Solid phase
5	95	Na_2SO_4*10H_2O
12	95	No solid phase
12	78	Na_2SO_4*10H_2O
19	61	No solid phase
26	44	NaCl, $NaNO_3$, $NaNO_3$*Na_2SO_4*H_2O

4.1.3 On equivalents and moles

Activity and molarity were plotted at T 5°C, 10°C, 20°C and 25°C at RH 85%, 90% and 95%. Raising T, activity enhances, as expected. According to the plots, in the case of sulphates it makes more sense to work out calculations considering equivalents than moles, as when the salt is under deliquescence it is almost all dissociated; viceversa, if all the salts would have behaved as "monovalent" by a functional point of view, moles would have been useful. In the graphic shown in Fig. 4.1.4, data regarding $(NH_4)_2SO_4$ are plotted, and it can be noticed that the activities of SO_4^{2-} and HSO_4^- differ by several orders of magnitude; the same situation is verified for Na_2SO_4.

(a)

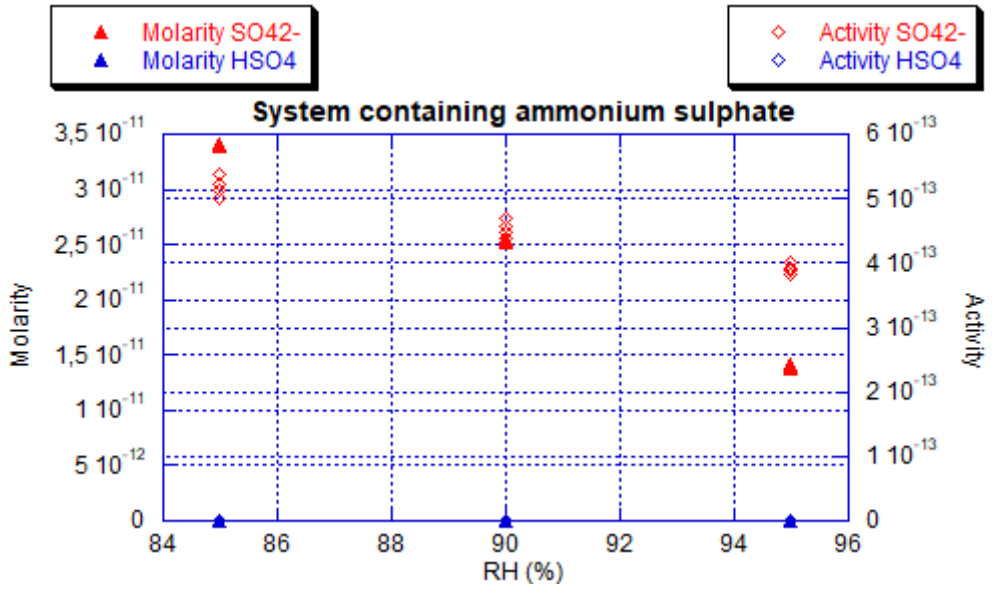

(b)

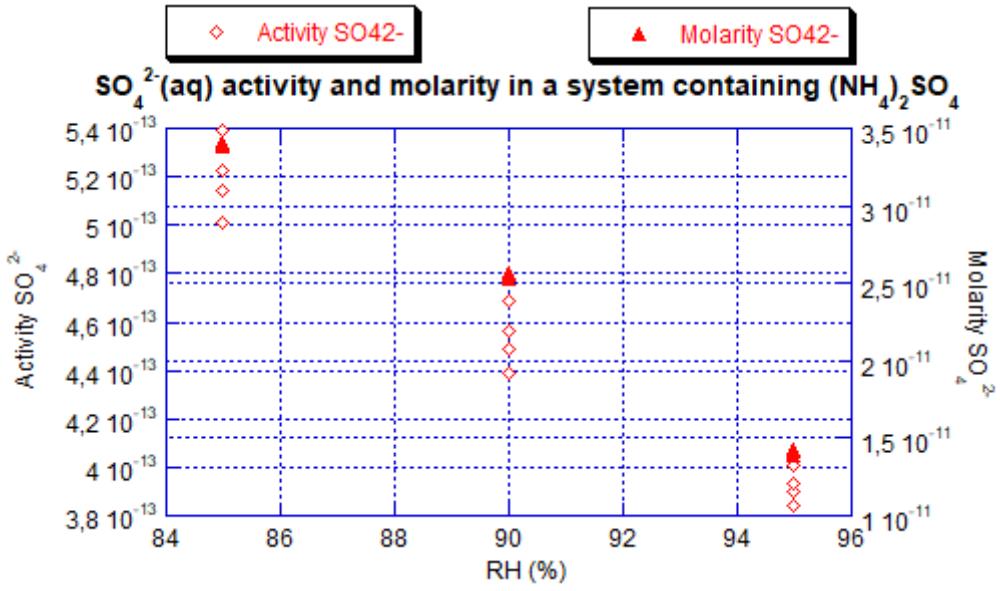

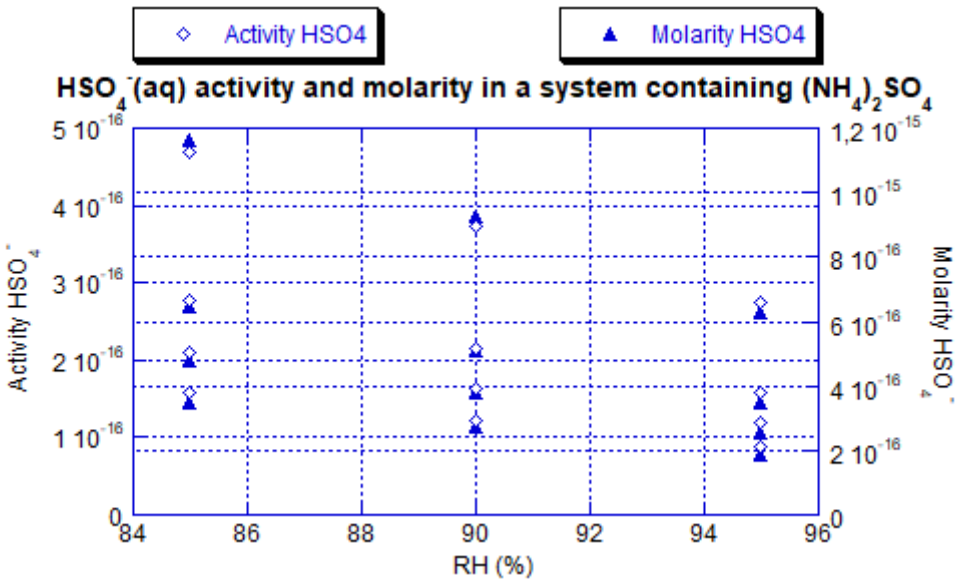

(c)

Fig. 4.1.4: Plots of activity and molarity at different T and RH values in a system containing $(NH_4)_2SO_4$ a) relative to both SO_4^{2-} and HSO_4^- ; b) expansion relative to SO_4^{2-}; c) expansion relative to HSO_4^-

4.2 Visual and Color changes

Considering that the single salts that were spread onto the specimens were all white or transparent, the visible color changes observed onto the “dry” samples give some hints about the reaction with the bronze substrates and the formation of corrosion products, mainly green ones.

The specimen treated with NaCl in “dry” modality evolved during the ageing forming green corrosion products (see Fig. 4.2.1), which expanded over time; the macroscopic appearance of these residues is similar, though maybe more blueish, to the one of NH_4NO_3 “dry” corrosion products (see Fig. 4.2.2 (a)). Also the $(NH_4)_2SO_4$ “dry” specimen presents greenish corrosion products at t3 (see Fig. 4.2.2 (b)).

On the other hand, corrosion products of $NaNO_3$ “dry” and Na_2SO_4 “dry” are the only ones that present a white/transparent aspect (see Fig. 4.2.2 (c) and (d)), and which are similar, in terms of color, to the corresponding “wet “ specimens.

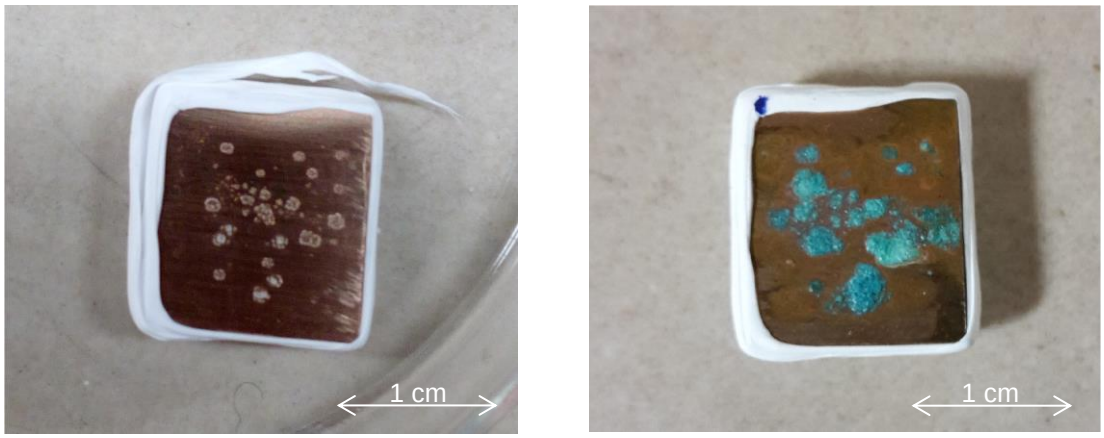

(a) (b)

Fig. 4.2.1: NaCl “dry” a) at t0; b) at t3

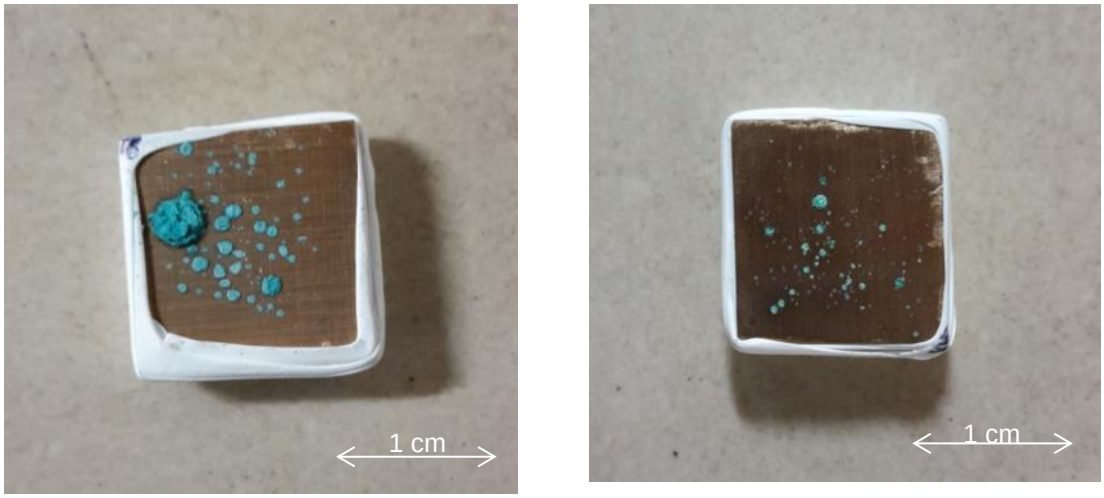

(a) (b)

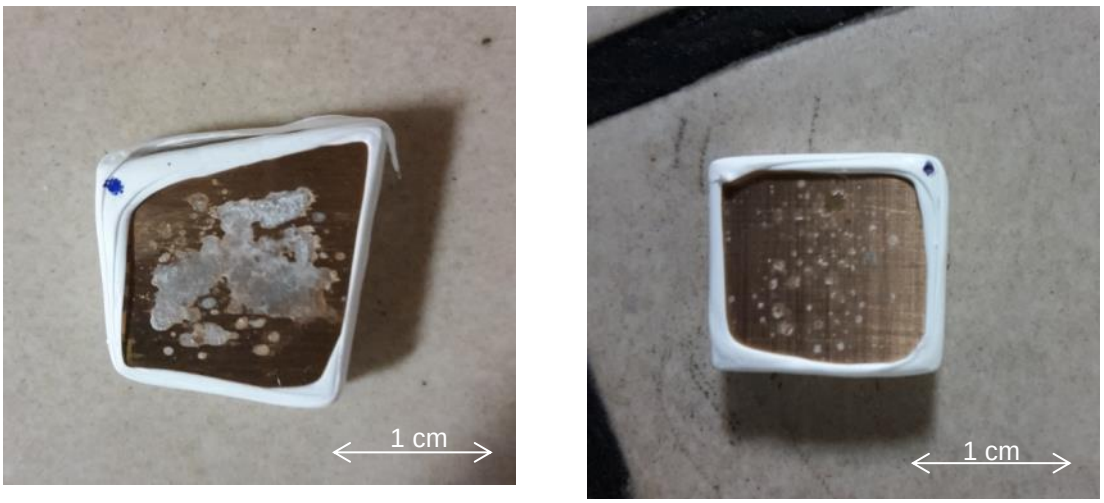

(c) (d)

Fig. 4.2.2: Macroscopic appearance of “dry” samples at t3: a) NH_4NO_3 “dry”; b) $(NH_4)_2SO_4$ “dry”; c) $NaNO_3$ “dry”; d) Na_2SO_4 “dry”

Concerning the evolution of the “wet” samples, in addition to visual examinations, also color measurements were performed. After the deposition of the single salts in “wet” fashion, the formation of a quite homogeneous white or almost transparent patina was observed on the specimens; the color variations of the “wet” samples over the whole ageing procedure have been monitored; the ΔL*, Δa* and Δb* were calculated considering as reference time “t0” the moment in which salts were applied to the samples and fixed onto them. According to the single salt specimens, the samples showed evident color changes ranging from t0 to t3, as ΔE*>3 in all cases, especially for the nude bronze and for the sodium salts. Every specimen lost part of its lightness, except for the Na_2SO_4 “wet” one; in particular, NaCl “wet” displays the highest absolute value for ΔL*. Regarding the Δa* and Δb*, all the samples looked more reddish and yellowish, even though this feature is more evident in Na_2SO_4 “wet” and in the nude bronze. Table 12 summarizes the results obtained. By considering the data obtained from each step (see Table 13 and Table 14), the most of the color changes seem to have happened during the first part of the ageing, while between t3 and t2 no striking modifications resulted, especially concerning the Δa* and Δb*, which are $<|1|$ in most of the cases.

Specimens treated with a ternary mixture of salts produced a white patina in the case of the “wet” sample at t0 and it remained almost unchanged up to t3, while the “dry” one changed the residues color from white (at t0) to green and brown (at t3). The macroscopic aspect of the “wet” and “dry” samples at t3 is displayed in Fig. 4.2.3.

Table 12: Color changes regarding “wet” single salt samples between t3 and t0

Sample	ΔL*	Δa*	Δb*	ΔE*
NaCl “wet”	-8.33	0.21	3.05	8.87
$NaNO_3$ “wet”	-2.53	2.29	6.2	7.08
Na_2SO_4 “wet”	0.51	3.72	10.35	11.01
NH_4NO_3 “wet”	-0.73	2.19	4.98	5.49
$(NH_4)_2SO_4$ “wet”	2.09	1.75	5.28	5.94
“Dry” Nude bronze	-2.86	4.54	15.05	15.98

Table 13: Color changes regarding “wet” single salt samples between t2 and t0

Sample	ΔL*	Δa*	Δb*	ΔE*
NaCl “wet”	-4.98	0.17	2.55	5.60
$NaNO_3$ “wet”	-4.97	1.56	3.3	6.17
Na_2SO_4 “wet”	2.34	2.18	7.14	7.82
NH_4NO_3 “wet”	1.28	1.74	4	4.55
$(NH_4)_2SO_4$ “wet”	3.62	1.82	5.35	6.71
“Dry” Nude bronze	1.27	3.05	7.96	8.62

Table 14: Color changes regarding “wet” single salt samples between t3 and t2

Sample	ΔL*	Δa*	Δb*	ΔE*
NaCl “wet”	-3.35	0.04	0.5	3.39
$NaNO_3$ “wet”	2.44	0.73	2.9	3.86
Na_2SO_4 “wet”	-1.83	1.54	3.21	4.00
NH_4NO_3 “wet”	-2.01	0.45	0.98	2.28
$(NH_4)_2SO_4$ “wet”	-1.53	-0.07	-0.07	1.53
“Dry” Nude bronze	0.11	0.46	2.62	2.66

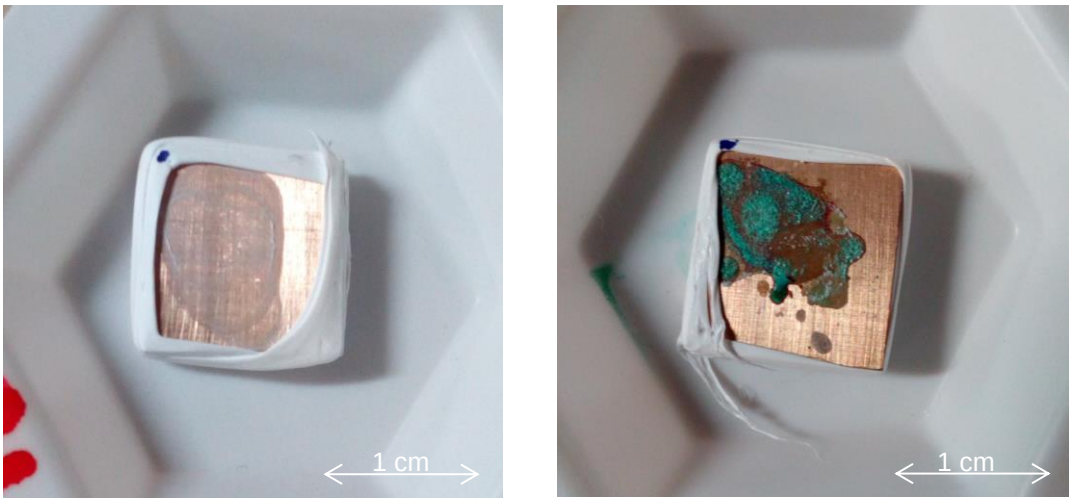

(a) (b)

Fig. 4.2.3: Macroscopic aspect of the samples treated with ternary mixture at t3 in a) “wet” and b) “dry” modality

According to the samples treated with a mixture simulating natural PM, the color data show that both in the “matrix” and in the “matrix+salts” samples visual color changes were evident from t0 to t3: in fact, both the ΔE* are far higher than 3

(see Table 15). Examining the single ΔL*, Δa* and Δb* contributions, it seems that lightness is the parameter that changed the most, resulting in an enhancement of lightness in the case of the “matrix” sample and in an opposite behaviour in the case of the “matrix+salts” sample. Regarding the Δa* and Δb*, the “matrix” sample became more reddish and yellowish, while the “matrix+salts” one just very slightly greener and blueish (see Table 15). Macroscopically, on the “matrix+salts” sample some greenish and brownish areas were formed at t3 around the border of the deposition drop, in correspondence of parts that underwent clearly to deliquescence during the ageing cycle, as shown in Fig. 4.2.4; these greenish and brownish residues have not been observed onto the “matrix” sample, therefore they are related to the soluble salts influence; similarities to macroscopic observations onto the “dry” sample trated with ternary salts mixture have been found.

Table 15: Color changes of samples with mixture simulating natural PM between t3 and t0

Sample	ΔL*	Δa*	Δb*	ΔE*
Matrix	10.23	2.27	5.54	11.85
Matrix + salts	-14.7	-0.44	-0.97	14.74

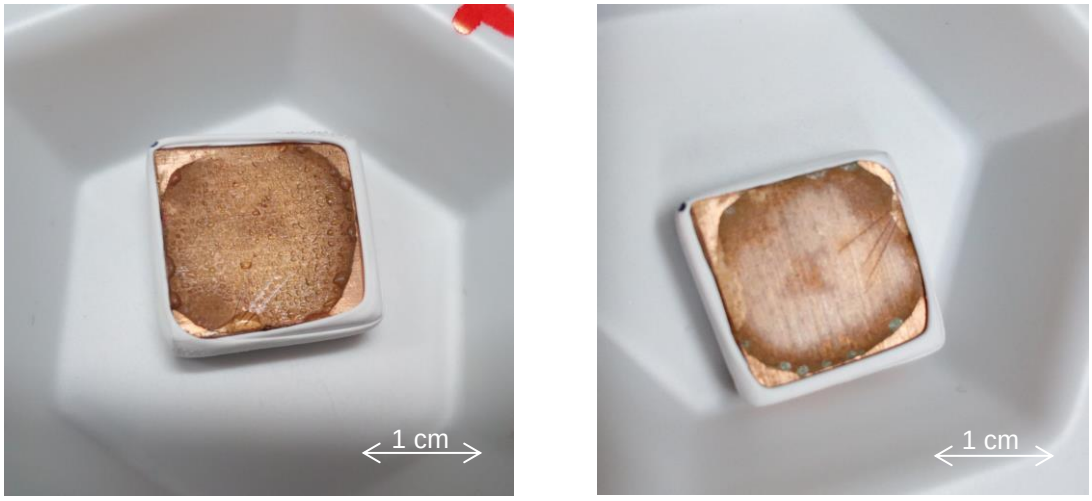

(a) (b)

Fig. 4.2.4: “Matrix+salts” sample a) at T 5°C and RH 95%, under deliquescence; b) at t3,displaying greenish residues along the border

Looking also at the reflectance curves (see Fig. 4.2.5), it can be observed that, while the “matrix+salts” curve seems mainly to shift down during ageing, the “matrix” curve not only shifts up but also seems to change its shape that, in general, is an indication of the occurring of compositional variation.

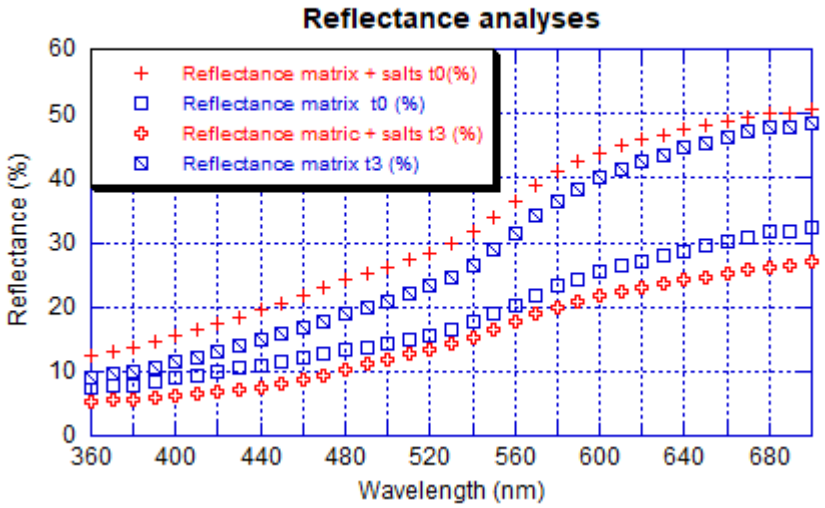

Fig. 4.2.5: Comparison of reflectance curves of “matrix” and “matrix+salts” samples at t0 and t3

So, considering both color and reflectance data, it could be supposed that the addition of salts to the matrix induce a darkening on the surfaces but not a great change on the a* and b* component, probably due to the formation of a mixture that better covers the surfaces and does not make chemical changes visible on the external layer. On the other side, the matrix itself leave the surface less “covered”, making the formation of red-yellow corrosion products more visually evident; the absence of soluble salts which form corrosion products with the substrate can allow the migration of matrix components against the deposition drop borders instead of “cementing” and preventing the migration of components away from the central area.

The specimen where natural PM was applied changed its visual appearence too from t0 to t3, becoming darker and more brownish and greenish over the parts of the sample which underwent to deliquescence (see Fig. 4.2.6 and Fig. 4.2.7), similarly to the sample treated with an artificial matrix and soluble salts.

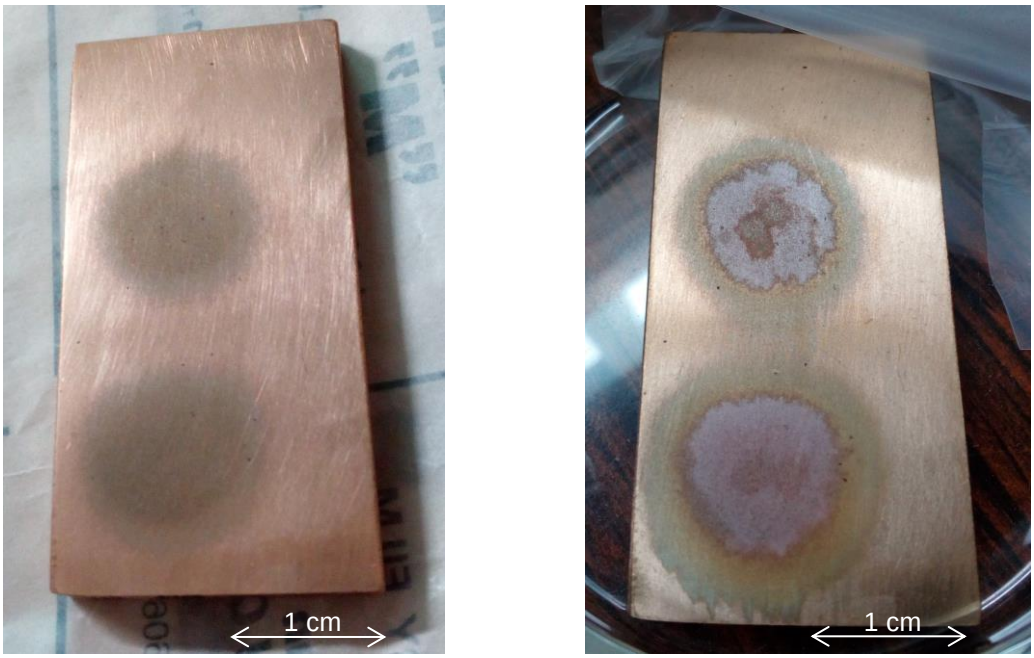

(a) (b)

Fig. 4.2.6: Macroscopic aspect of the sample treated with natural PM a) at t0; b) at t3.

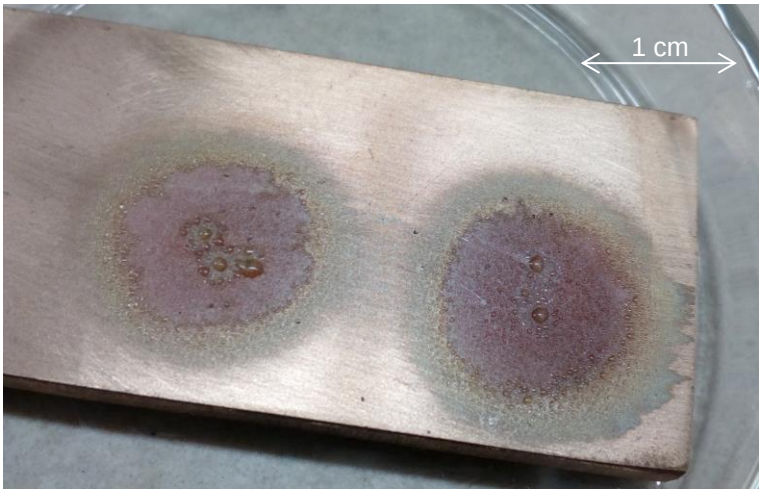

Fig. 4.2.7: Sample treated with natural PM at T 5°C and RH 95%, showing areas underdeliquescence

4.3 Surface analyses: evolution of salts and corrosion products

4.3.1 Single salts samples

4.3.1.1 Blank

The “dry” blank specimen did not shown any peculiar feature at t0, developing just cuprite (Cu_2O) during the accelerated aging and Pb carbonates and oxides between t2 and t3. The cuprite identification was confirmed by Raman spectroscopy: in particular, the Raman active band belonging to the triply degenerate bending mode was found at 525 cm^{-1}, together with further well known peaks at 634, 436, 217 and 120 cm^{-1} which would be expected to be silent, but that are frequently observed because of a breakdown of selection rules ascribed to defects, non-stoichiometry and resonant excitation [76]. Cerussite ($PbCO_3$) was identified from the band relative to the carbonate symmetric stretching mode at 1048 cm^{-1} [77-79], while litharge (α-PbO) by peaks at 202 cm^{-1}, resulting by a combination of vibrational modes, and at 155 cm^{-1}, relative to the Pb-O symmetric stretching mode [80]. Moreover, condensation water (in low T and high RH conditions) was found onto the specimens only in areas where salts were spread, therefore lowering on the blank “dry” specimen the formation of corrosion products due to the interaction of the bronze with water.

The “wet” blank specimen at t0 presented Pb carbonates (snowflake-shaped crystals) and oxides (stick-shaped crystals), which were identified by Raman analyses as cerussite, litharge and massicot (β-PbO). These lead oxides were found associated in some Raman spectra, resulting in a shift towards lower frequencies of the Raman modes that are active for both the species, as for the Pb-O symmetric stretching mode (that for massicot alone falls around 145 cm^{-1} [77]) and in the appearance of bands belonging to massicot-only due to its lower symmetry (orthorhombic) with respect to litharge (tetragonal). These residues remained almost unaltered over the whole aging, except for the hydration of cerussite to hydrocerussite ($2PbCO_3*Pb(OH)_2$) at t1, distinguishable from cerussite because of the Raman shift of the symmetric stretching band at 1048

cm^{-1} [77-79] and of the CO antisymmetric stretching mode at 1365 cm^{-1} [79]; at t3 hydrocerussite is the main species that is detected together with cuprite. Magnifications up to 5000x were reached by SEM in order to observe the cited residues (see Fig. 4.3.1).

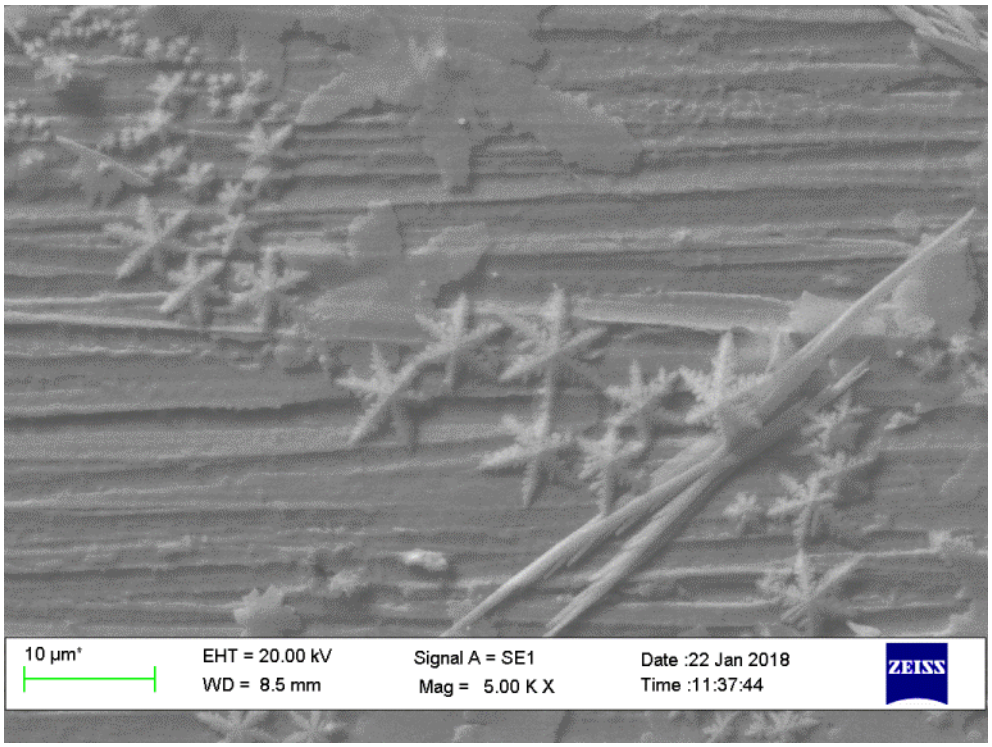

Fig. 4.3.1: Blank “wet” at t0, SEM image in secondary electrons of Pb based crystals at 5000x magnification.

4.3.1.2 NaCl

NaCl “dry”

The SEM analyses showed that at t0, corresponding to the moment next to the first deliquescence and recrystallization after the salt deposition, the main mineral species onto the specimen were euhedral cubes (see Fig. 4.3.3), that EDX proved to be constituted by Na and Cl in 1:1 ratio, and elongated Pb based crystals below 10 µm, which were identified as PbO by the atomic percentages of the EDX analysis. The cubes were identified definitively as halite (NaCl) after the Raman analysis, which did not provide any signal, as NaCl is Raman silent; the sodium chloride crystals have recrystallized without migrating far from the

original deposition sites. An enrichment in oxygen was found to be due to cuprite formation.

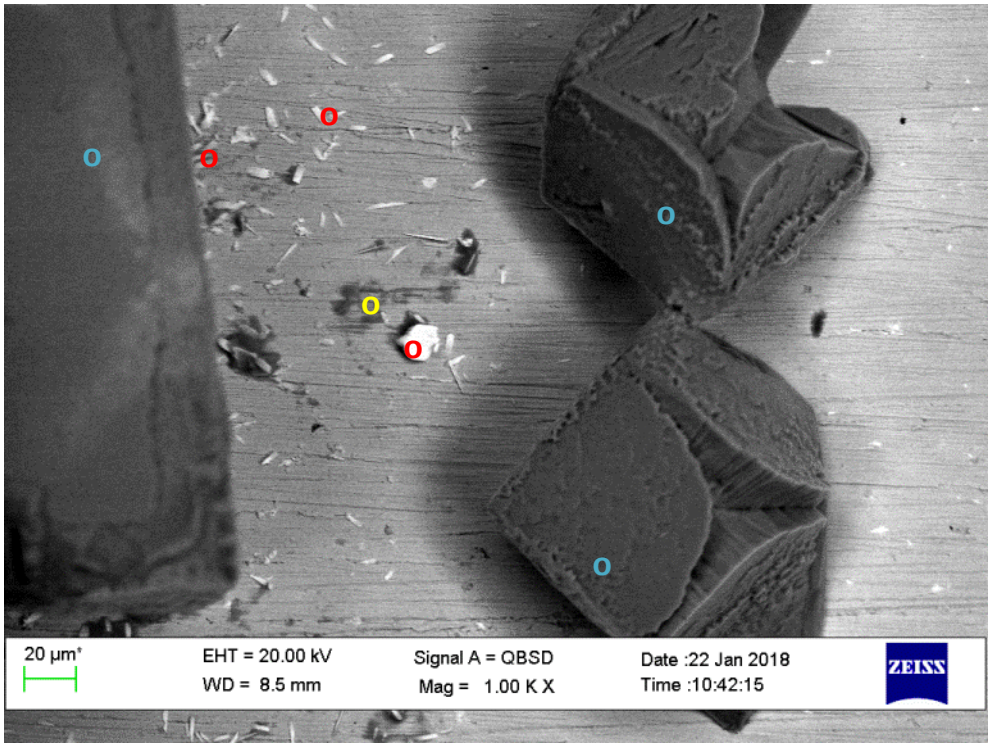

EDX - atomic %:	Assignment
o Na K 50%, Cl K 50%	NaCl
o Pb M 50%, O K 50%	PbO
o CuK 66%, O K 33%	Cu_2O

Fig. 4.3.3: NaCl “dry” at t0: SEM image in backscattered electrons of NaCl cubes and Pb based crystals at 1000x magnification.

At t1, some NaCl crystals were found again, but crystals observed at t0 seemed to be “melted”, as a consequence of the deliquescence/recrystallisation cycles to which the sample was submitted during the first week of ageing. Clinoatacamite ($Cu_2Cl(OH)_3$) crystals of a few microns were found to be formed (see Fig. 4.3.4) by the analysis of the Raman spectra: bands relative to Cu-O-H deformations were found between 979 and 926 cm^{-1}, one band relative to Cu-O stretching at 512 cm^{-1} and one last signal at 356 cm^{-1} relative to Cu-Cl stretching [81]. Pitting was observed for the first time at t1.

At t2, pitting was enhanced (see Fig. 4.3.5) and Raman analyses on the pitting areas show presence of Pb carbonates. Clinoatacamite and cuprite were found again.

At t3, cross-like shaped crystals, whose composition in atomic percentages was Na K 50%, Cl K 50% by EDX, were observed (see Fig. 4.3.6). EDX on some areas found Na K 33%, C K 16,5%, O K 49,5%, Cl K 1%, which could derive from sodium carbonate with some copper carbonate and chloride impurities, that could be responsible of the green color of the residue. Pitting was further enhanced. At t3 Raman analyses allowed to identify the presence of cuprite and atacamite ($Cu_2Cl(OH)_3$), which was confirmed by ATR-FTIR analyses (details on the vibrational frequencies are shown in Table 16). Clinoatacamite and atacamite are green substances, and their finding is in agreement with the macroscopic observation on the corrosion products of this specimen at t3 (see Fig. 4.2.1 (b)).

Atacamite displays in its structure two Cu(II) centers in a distorted octahedral fashion with surrounding OH and Cl groups; the principal fingerprints to recognise atacamite by its vibrational modes are the ones involving hydroxyl groups.

In the ATR-FTIR spectra that were recorded (see Fig. 4.3.7 as an example), signals belonging to hydroxyl groups stretchings were found at 3440, 3423, 3331, 3306 cm^{-1}, in agreement with spectra published by Frost et al. (2002) [82]. Further bands in the hydroxyl group deformation region, between 980 and 820 cm^{-1}, and in the Cu-O stretching region, between 600 and 450 cm^{-1}, were recorded both by Raman and by ATR-FTIR spectroscopy (see Table 16). The Cu-Cl stretching modes are better visible in the Raman spectrum of atacamite, as the diamond cell for ATR-FTIR spectral limit is 400 cm^{-1}; however, one band at 418 cm^{-1} could be discriminated in the IR spectrum and assigned to this vibrational mode. The last vibrational mode that gave rise to a peak in the Raman spectrum is the O-Cu-O bending, assigned to the band at 120 cm^{-1}. [81]

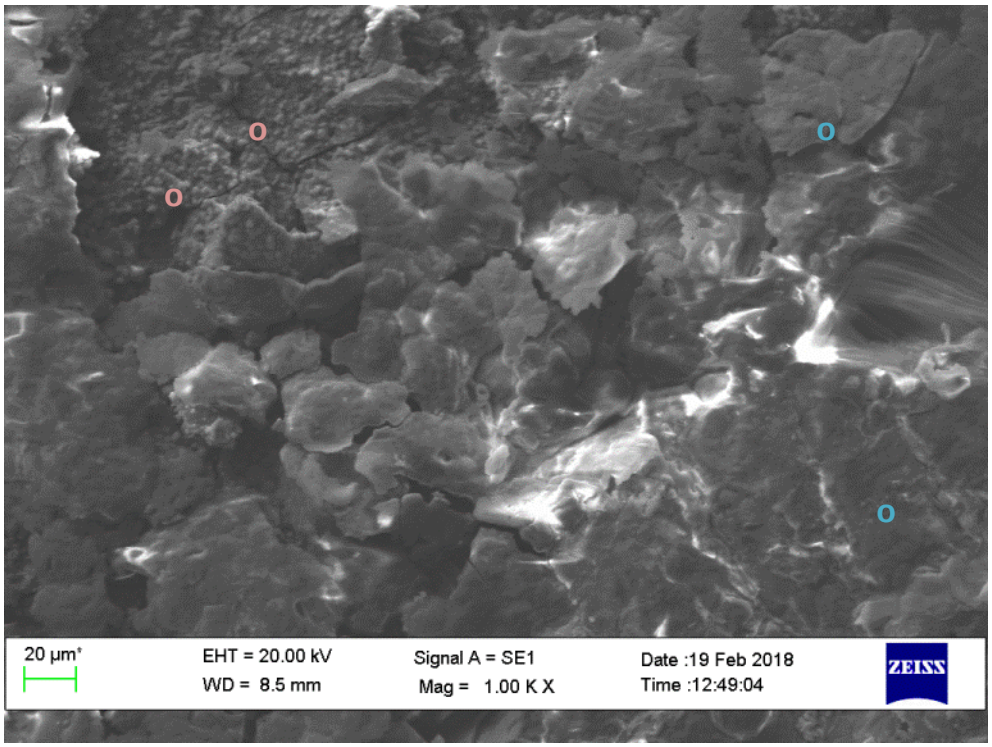

EDX - atomic %:	Assignment
o Na K 50%, Cl K 50%	NaCl
o Cu K 33%, O K 50,5%, Cl K 16,5%	$Cu_2Cl(OH)_3$

Fig. 4.3.4: NaCl “dry”, SEM image recorded at t1 in secondary electrons at 1000x magnification

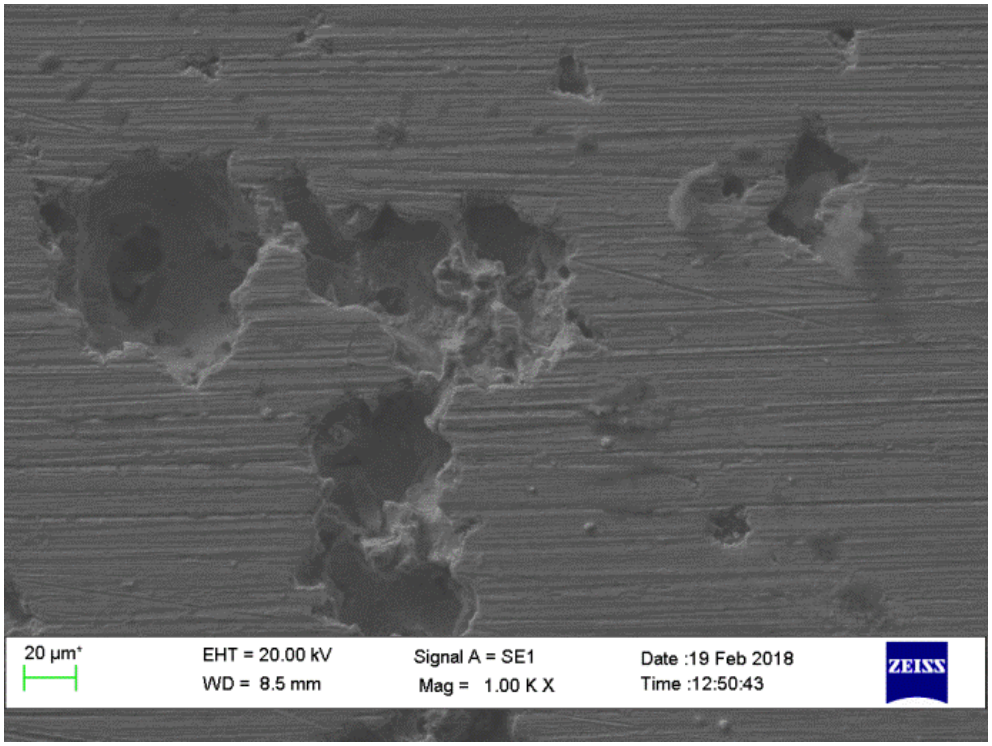

Fig. 4.3.5: NaCl “dry” at t2: SEM image of pitting in secondary electrons at 1000x magnification.

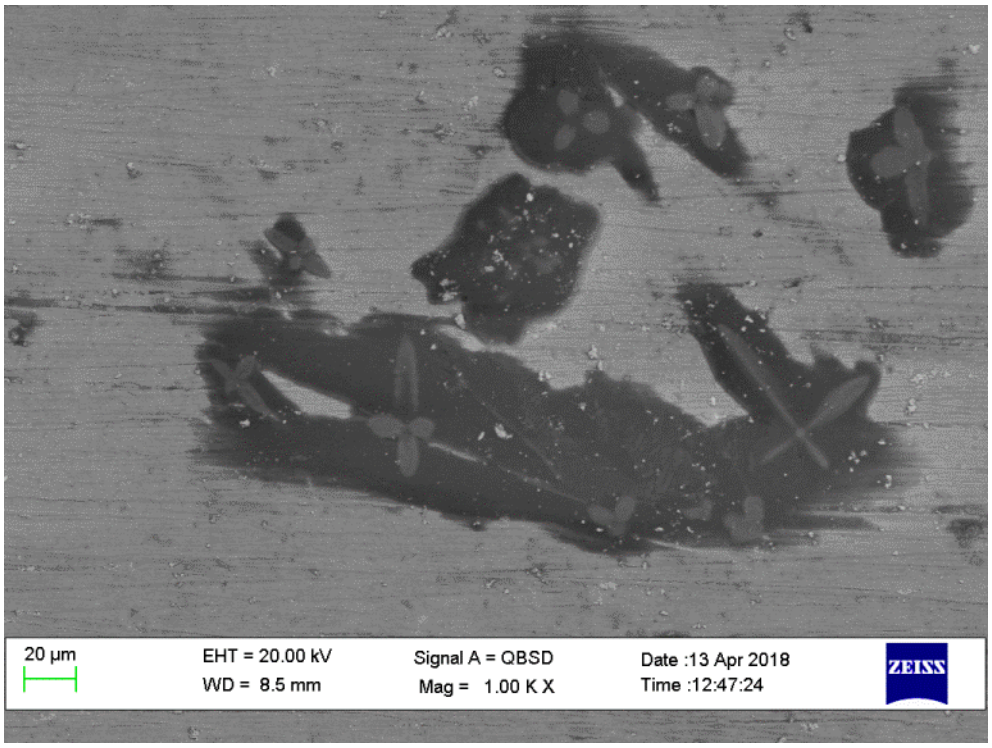

Fig. 4.3.6: NaCl “dry” at t3: SEM image of cross-shaped crystals in backscattered electrons at 1000x magnification.

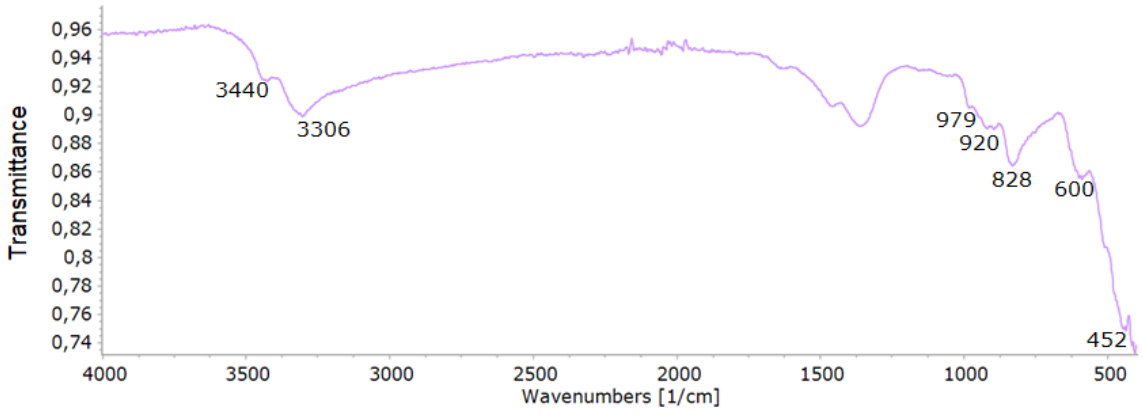

Fig. 4.3.7: ATR-FTIR spectrum of NaCl “dry” at t3; atacamite peaks labelled

Table 16: Raman and ATR-FTIR bands of atacamite

Raman (cm^{-1})	ATR-FTIR (cm^{-1})	Assignment [82]
	3440	O-H stretching modes
	3423	
	3331	
	3306	
970	979	-O-H deformation modes
915	920	
	886	
822	828	
	600	Cu-O stretching
510	511	
	471	
	452	
	418	Cu-Cl stretching
356		
120		O-Cu-O bending

NaCl "wet"

NaCl "wet" presented most of residues along the deposition drop borders since t0 up to t3. Structures presenting similar features to the cross-like shaped crystals found on the NaCl "dry" sample at t3 were observed on the NaCl "wet" sample at t0 (see Fig. 4.3.8), again identified as sodium chloride. These structures seem to be connected to the hexagonal ones mainly found on the border and visible in Fig. 4.3.9 (a). Actually, according to Sunagawa et al. studies [83], the habitus of NaCl can change from cubic to octahedral if impurities of Pb are present, therefore justifying a possible rearrangement of the crystals. However, after one week of accelerated aging (t1), in the same zone the cross-like conformations seem to have lost their original shape and being melted together: as it is shown in Fig. 4.3.9 (b), some of the hexagons and cubes seem "corroded" from their inner part, probably because condensed water stacks onto the upper face of the polyhedrons (see Fig. 4.3.10). Residues result expanded from the borders, surrounding inner rounded crystals which at t0 were constituted by Cu, Cl, and O. At magnification 2000x, other rounded crystals, smaller and lighter, and star-shaped crystals, both Pb based, are found both at t0 and at t1

(Fig. 4.3.11): their analogues have been found on the blank “wet” specimen, corresponding to Pb carbonates and oxides.

At t2 cuprite, clinoatacamite and atacamite were observed (see Fig. 4.3.12 (a) and (b)) and identified by Raman spectroscopy. On the “wet” sample pitting starts to be observed at t2, while on NaCl “dry” at t1, and it is highly enhanced at t3. At t3 cuprite and malachite have been found (see Fig. 4.3.13). The most significant malachite Raman peaks relative to the carbonate modes were found at 1497 cm^{-1}, belonging to the antisymmetric stretching and between 1098 and 1058 cm^{-1}. Regarding the vibrational modes that involve copper, Cu-C and Cu-O stretchings were found respectively at 530 and 432 cm^{-1}; further details on the Raman shift assignments are presented in Table 17. Malachite’s formation is hypotheized to be relate with a cation exchange mechanism that occurs with Pb carbonates, that were not detected together with malachite; another hypothesis concerns the malachite evolution from cuprite [84].

EDX on 500x homogeneous area showed an enhancement of C and O onto the surface (see Table 18) over the ageing; in particular, the oxygen uptake has happened during the first week of ageing, and then its atomic percentage has remained almost unaltered; data regarding lead shift up and downwards because of its irregular distribution in the bronze piece.

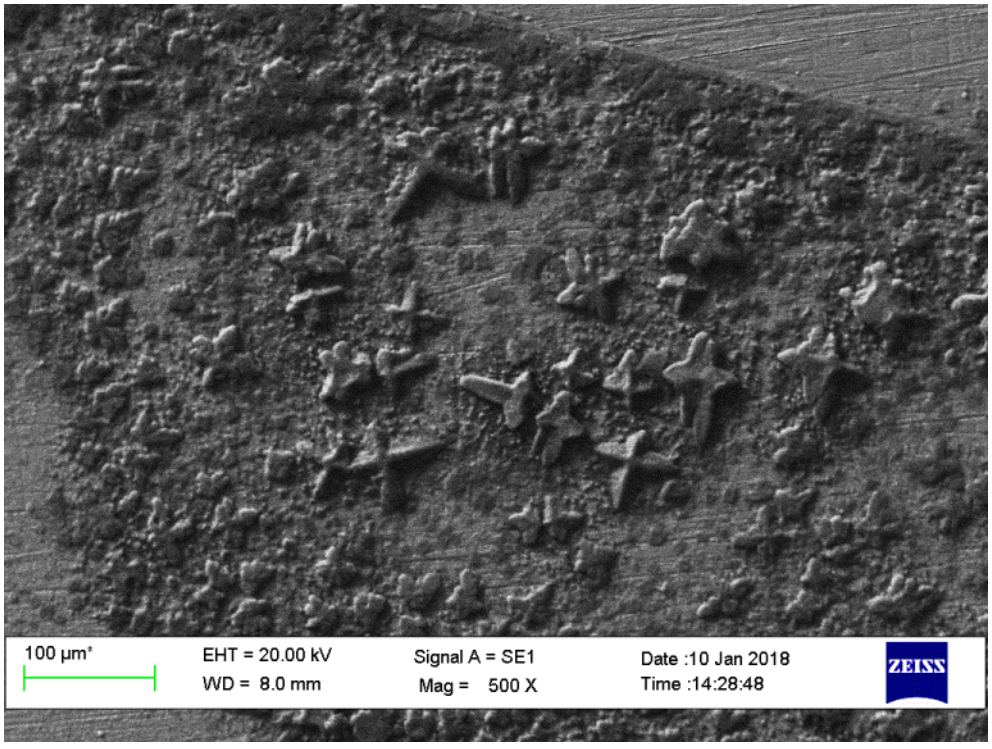

Fig. 4.3.8: NaCl “wet” at t0: SEM image of cross-shaped crystals at 500x magnification.

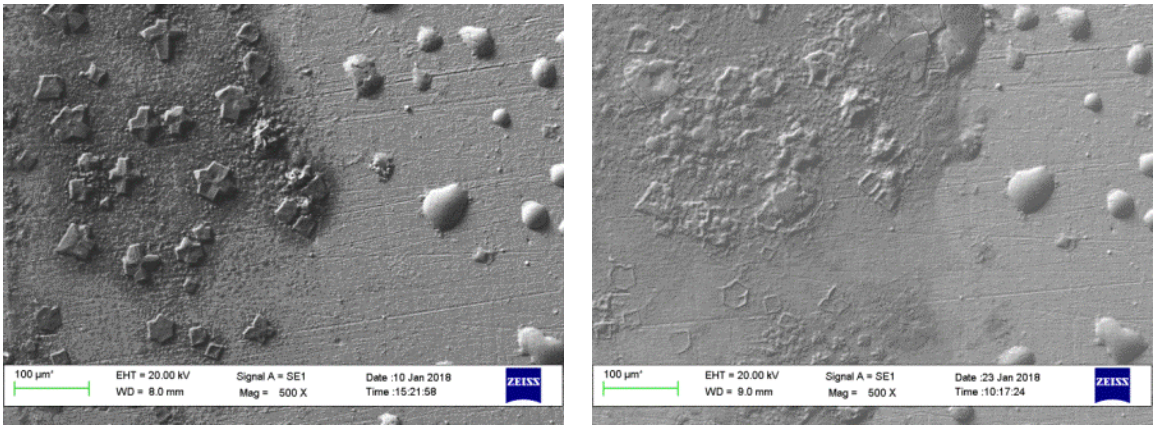

(a) (b)

Fig. 4.3.9: NaCl “wet”: SEM image on the left border of the deposition drop at 500x magnification a) at t0; b) at t1

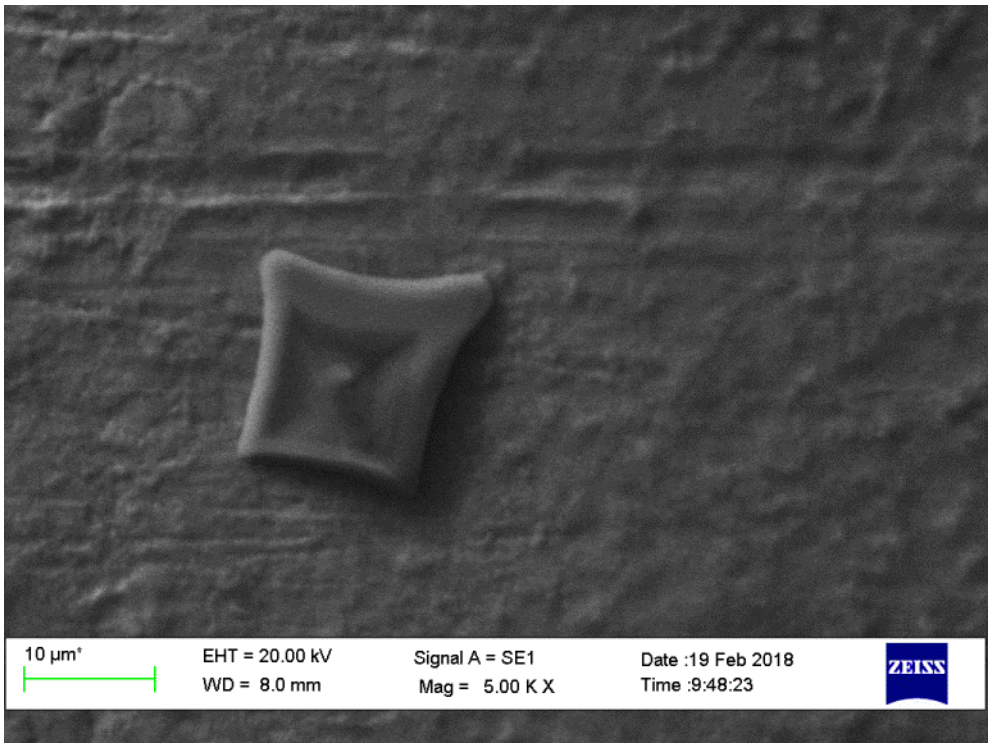

Fig. 4.3.10: NaCl “wet” at t2: detail of a cubic crystal under corrosion by SEM in secondary electrons at 5000x magnification.

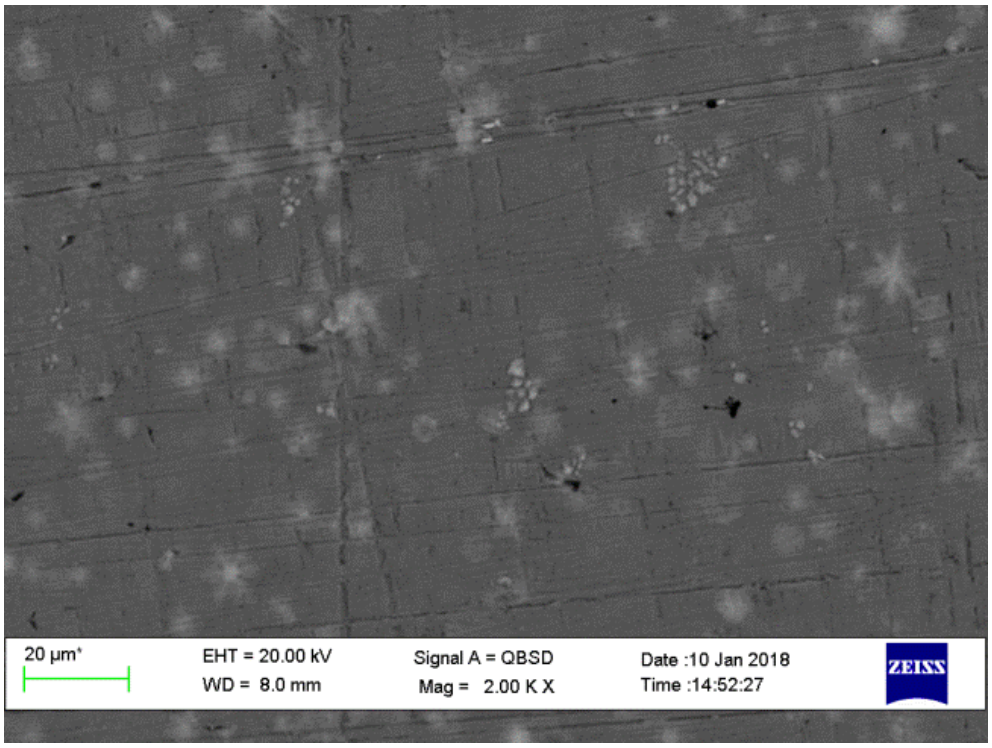

Fig. 4.3.11: NaCl “wet” at t1: SEM image in backscattered electrons of Pb based crystals at 2000x magnification.

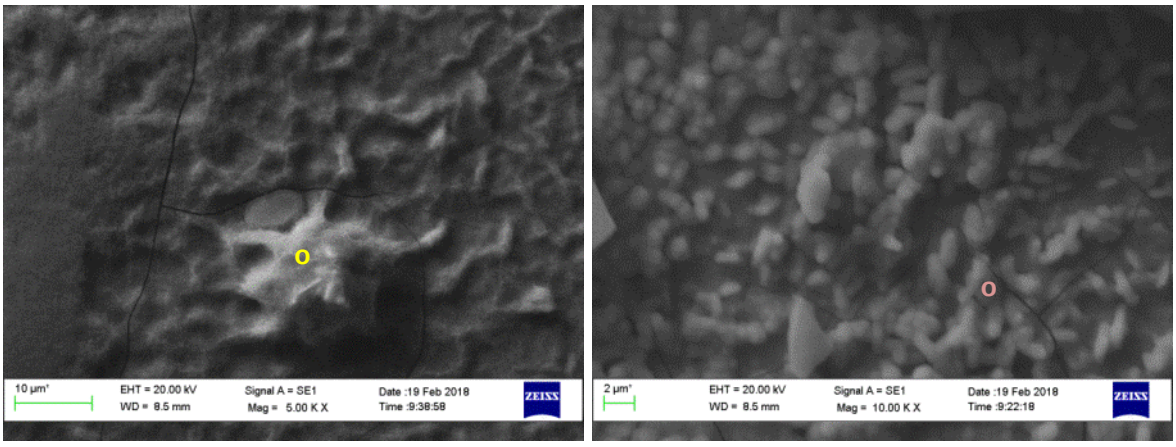

(a) (b)

EDX - atomic %:	Assignment
o Cu K 66,5%, O K 33,5%	Cu_2O
o Cu K 33%, O K 50,5%, Cl K 16,5%	$Cu_2Cl(OH)_3$

Fig. 4.3.12: NaCl “wet” at t2: SEM image of a) cuprite; b) $Cu_2Cl(OH)_3$

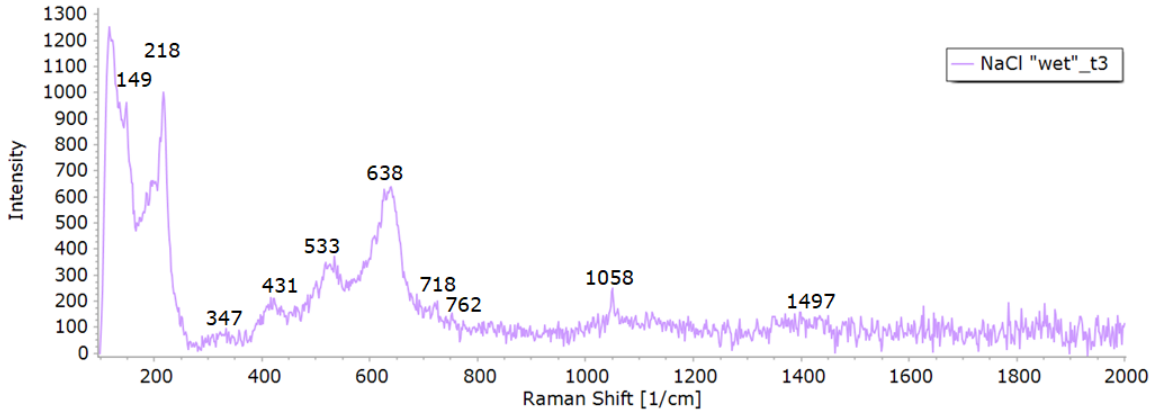

Fig. 4.3.13: NaCl “wet” at t3: Raman spectrum of malachite and cuprite

Table 17: Raman shift of malachite

Raman (cm^{-1})	Assignment [85]
1497	antisymmetric CO_3^{2-} stretching
Broad band between 1098 and 1058	CO_3^{2-} symmetric stretching modes
762	CO_3^{2-} deformation
718	CO_3^{2-} deformation
533	Cu-C stretching
431	Cu-O stretching
347	HO-Cu-OH bending
218	CO-Cu-OH bending mode
149	CO-Cu-OC bending mode

Table 18: EDX analyses on 500x homogeneous area of NaCl “wet”

Element	Atomic percentages (%)			
	t0	t1	t2	t3
C	19	20	25	25
O	27	33	32	33
Cu	48	42	37	38
Zn	3	3	3	2
Sn	1	1	1	1
Pb	1	1	1	1

4.3.1.3 $NaNO_3$

$NaNO_3$ "dry"

Interactions between the spread salt and the bronze sample have happened just poorly in $NaNO_3$ "dry" sample, where nitratine ($NaNO_3$) crystals have been identified from t0 to t3 thanks to Raman spectra (see Fig. 4.3.14). The main band, relative to NO_3^- symmetric stretching, is visible at 1067 cm^{-1}; the assignments for the other peaks are listed in Table 19 [86]. The decrease of the Raman peaks intensity from t0 to t3 can be explained by the loss of $NaNO_3$ crystallinity. At t0 $NaNO_3$ rhombohedral crystals were surrounded by smaller Pb based crystals (see Fig. 4.3.15).

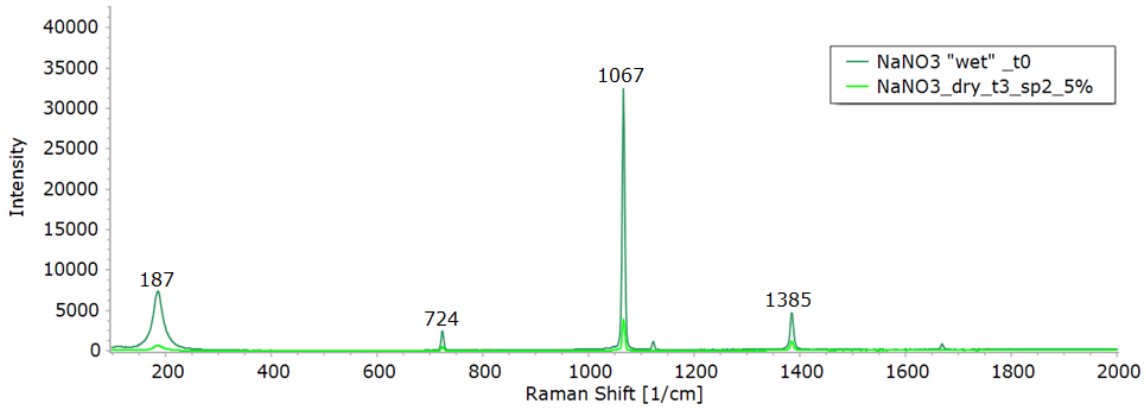

Fig. 4.3.14: Raman spectra of $NaNO_3$ "wet" at t0 and at t3

At t1 $NaNO_3$ euhedral crystals lookee "melted", and recrystallized in smaller size, as it can be noticed by comparing Fig. 4.3.15 (a) and (b). Zooming on areas where the quantity of residues is high (see Fig. 4.3.17), by performing the EDX analysis the presence of $NaNO_3$ together with Na and Pb carbonates can be hypotheized. At t1 and t2, further Raman peaks at 1058 cm^{-1}, relative to carbonate symmetric stretching, and at 682 cm^{-1}, relative to carbonate in plane bending, were found: these peaks can be assigned to sodium carbonate species, whose Raman shift differs depending on the hydration degree.

At t3 the presence of $NaNO_3$ was confirmed by both EDX, Raman and ATR-FTIR analyses; the comparison of the ATR-FTIR spectrum (see Fig. 4.3.18) and of the Raman spectra enhabled the identification of further species that were detected,

as cuprite and sodium carbonates (see Table 19 for Raman and ATR-FTIR signal assignments).

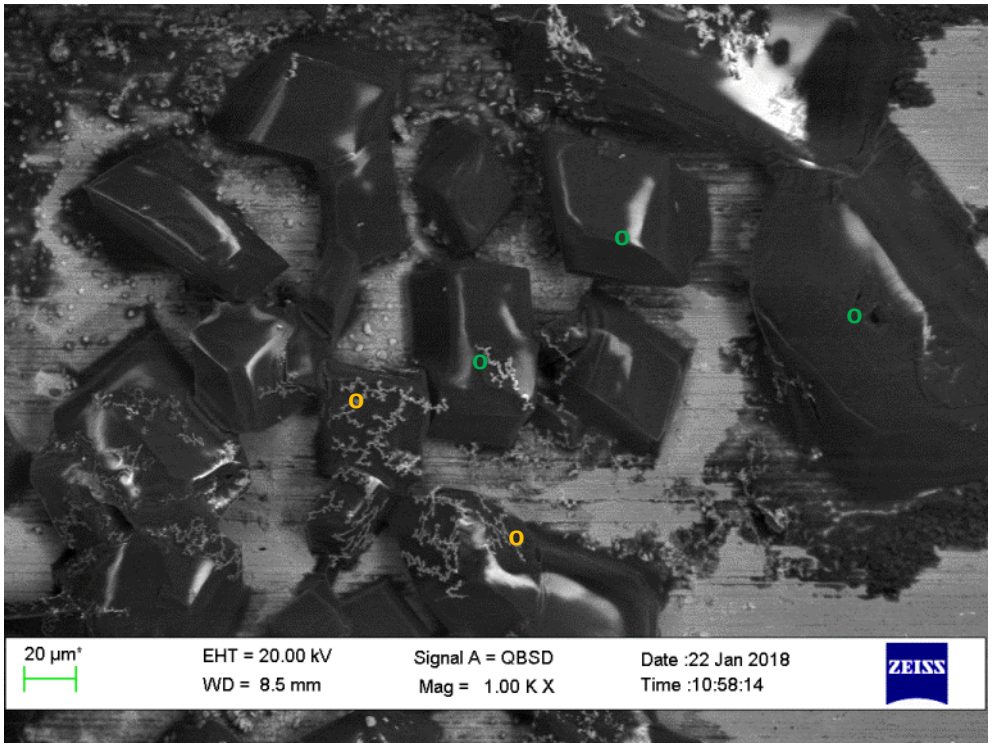

EDX - atomic %:	Identification
o Na K 20%, N K 20 %, O K 60%	$NaNO_3$
o C K 4%, N K 23%, Pb M 2%, Na K 12%, O K 54%	$NaNO_3$, Pb carbonates and Pb nitrates

Fig. 4.3.15: $NaNO_3$ “dry” at t0: SEM image at 1000x magnification.

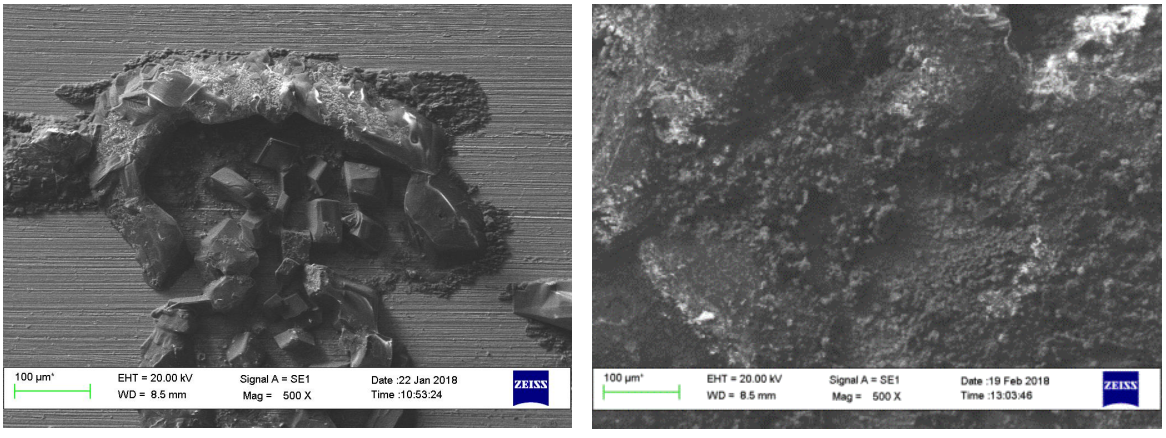

(a) (b)

Fig. 4.3.16: $NaNO_3$ “dry”: SEM images at 500x magnification a) at t0; b) at t1.

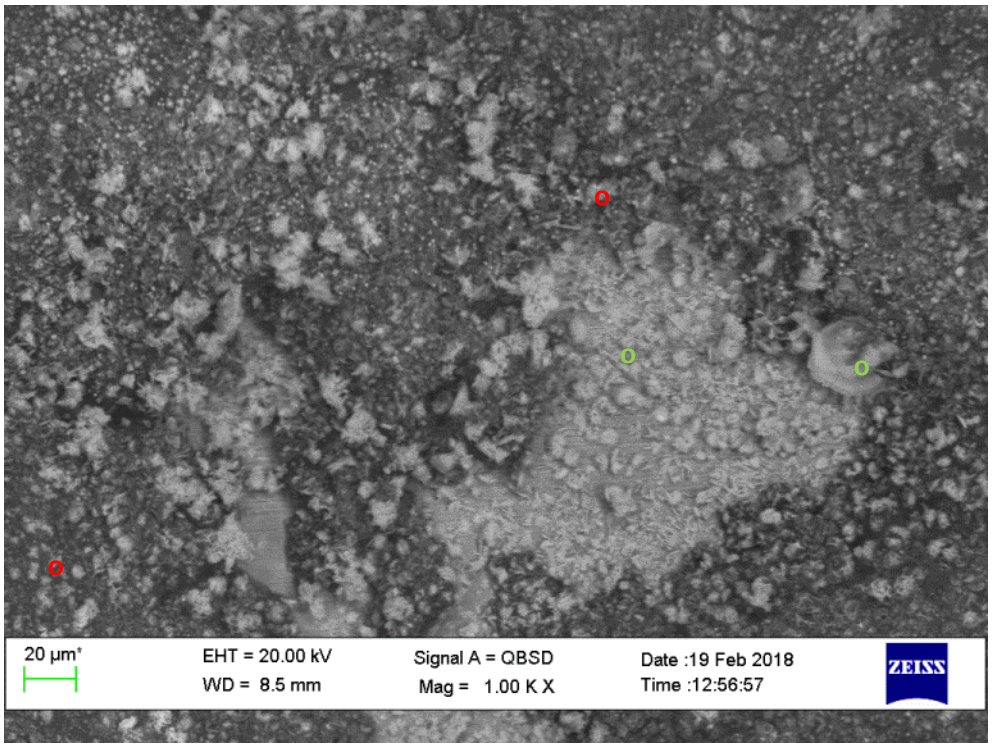

EDX - atomic %:	Identification
o C K 18%, Na K 7 %, N K 14 %,	$NaNO_3$, $PbCO_3$
O K 53%, Pb M 5%	$PbCO_3$
o C K 27%, Pb M 8% O K 40%	

Fig. 4.3.17: $NaNO_3$ “dry” at t1: SEM image in backscattered electrons at 1000x magnification.

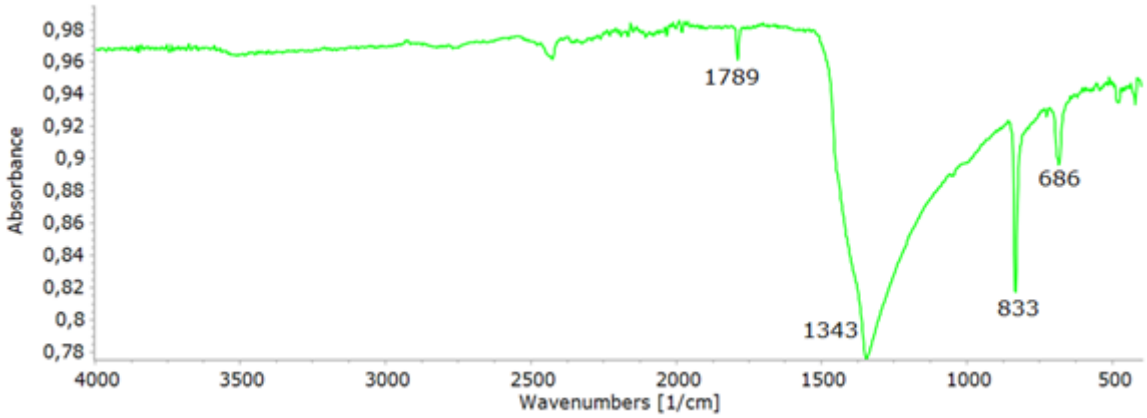

Fig. 4.3.18: ATR-FTIR spectrum of $NaNO_3$ “dry” at t3

Table 19: Raman and ATR-FTIR bands identified on $NaNO_3$ “dry” at t3

Raman (cm^{-1})	ATR-FTIR (cm^{-1})	Assignment [86]
	1789	NO_3^- in plane bending overtone
1385	1343	NO_3^- asymmetric stretching
1067		NO_3^- symmetric stretching
1058		CO_3^{2-} symmetric stretching
	833	NO_3^- out of plane bending
724		NO_3^- in plane bending
683	686	CO_3^{2-} in plane bending
187		NO_3^- librational mode

$NaNO_3$ “wet”

Examining the SEM images recorded on $NaNO_3$ “wet”, as it is shown in Fig. 4.3.19 (a) and (b), no significant differences were observed in the top arc of the $NaNO_3$ deposition drop, nor at larger magnifications. EDX analyses were carried out on the residues in Fig. 4.3.19 (c) and (d), finding Pb, Na, C, O, N, which were found to belong to $NaNO_3$, hydrocerussite and PbO from Raman analyses (see Raman spectrum in Fig. 4.3.20 and peak assignments in Table 20). Proceeding from the top border to the inner part of the deposition drop, a massive coverage was found, present both at t0 and at t3. The central part of the specimen, shown in Fig. 4.3.21, had more thinned residues, that resulted almost unchanged from t0 to t3, and the bronze surface was therefore visible. The EDX analysis that was here performed revealed the presence of Pb, N, O, C and Cu in atomic ratios 15: 14 : 50 : 6, probably indicating the formation of lead nitrates and carbonates.

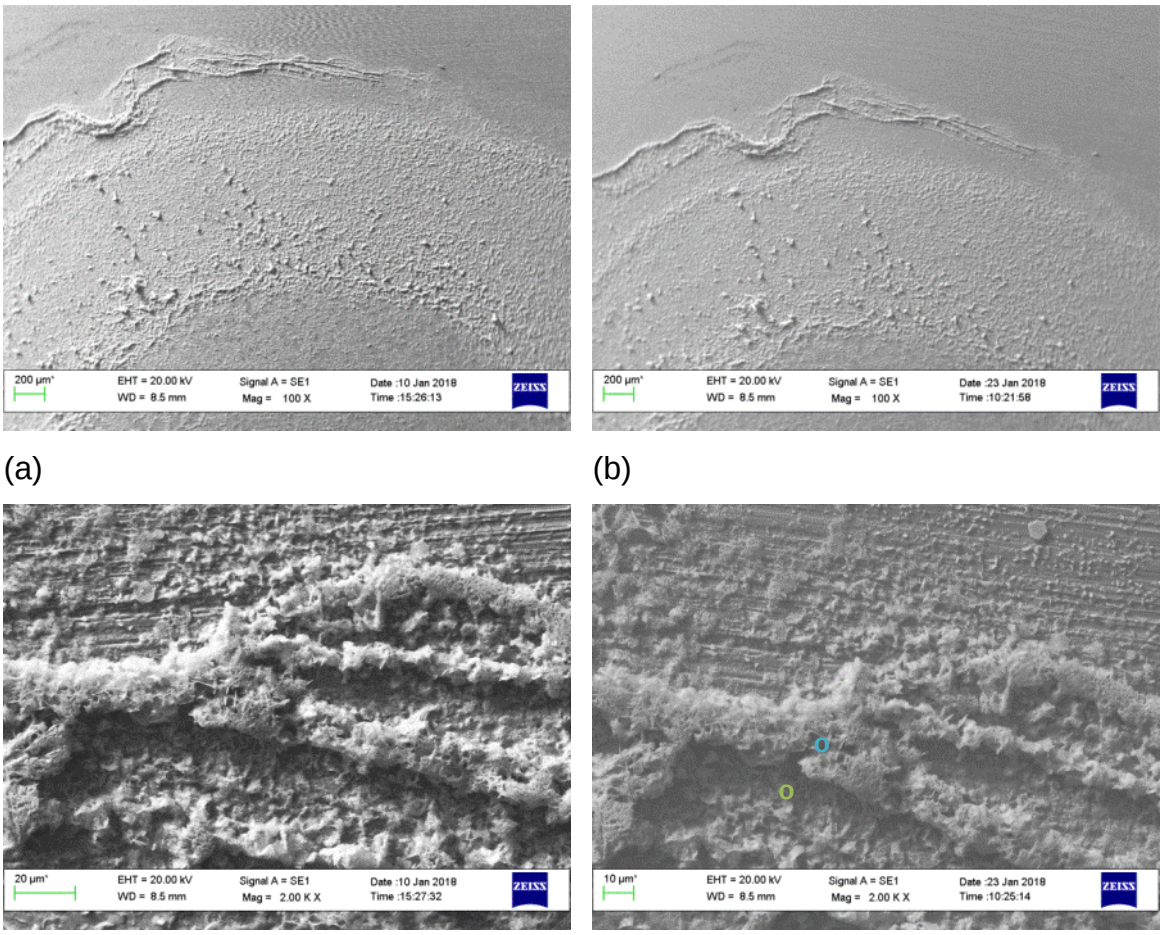

EDX - atomic %:	Assignment
o C K 26%, Na K 4 %, N K 14 %, O K 57%, Pb M 11%	$NaNO_3$, Pb carbonates
o C K 23%, Pb M 10% O K 54%	Pb carbonates

Fig. 4.3.19: $NaNO_3$ "wet", top arc view by SEM a) at t0, 100x; b) at t1, 100x; c) at t0, 2000x; d) at t1, 2000x.

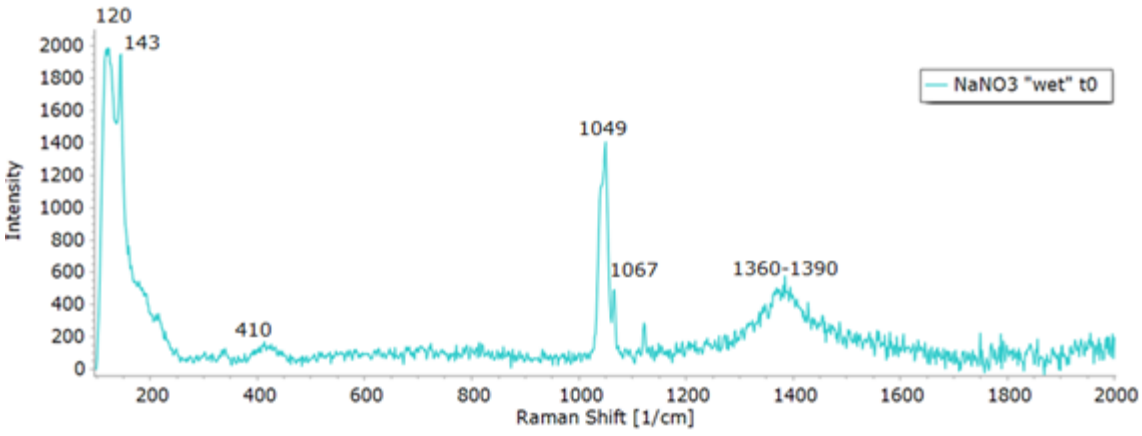

Fig. 4.3.20: Raman spectrum recorded on $NaNO_3$ "wet" at t0

Table 20: Raman peaks assignments for $NaNO_3$ “wet” at t0

Raman (cm^{-1})	Assignment [85]	Species
1390-1360	CO_3^{2-} asymmetric stretching	$Pb_3(CO_3)_2(OH)_2$
1067	NO_3^- asymmetric stretching	$NaNO_3$
1049	CO_3^{2-} symmetric stretching	$Pb_3(CO_3)_2(OH)_2$
410	CO_3^{2-} bending	$Pb_3(CO_3)_2(OH)_2$
143	Pb-O symmetric stretching	PbO
120	Lattice mode	$Pb_3(CO_3)_2(OH)_2$

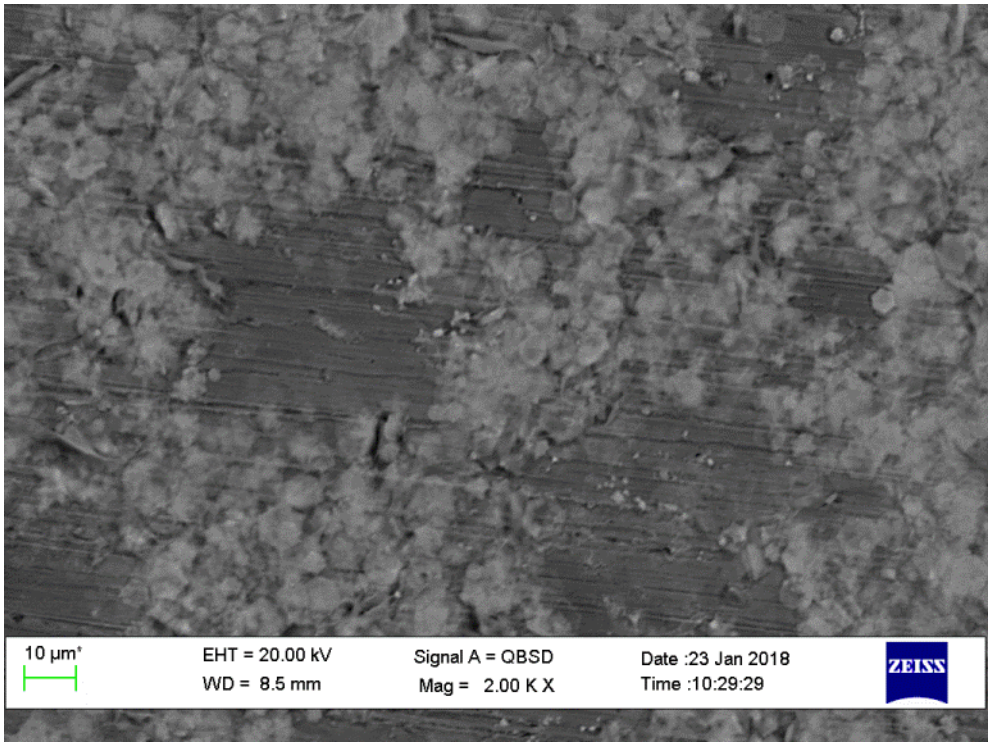

Fig. 4.3.21: $NaNO_3$ “wet” at t0: SEM image in backscattered electrons of the central area at 2000x magnification.

4.3.1.4 Na_2SO_4

Na_2SO_4 “dry”

The Na_2SO_4 “dry” sample displayed thenardite (Na_2SO_4) crystals at t0 (see Fig. 4.3.22 (a)), as suggested by EDX analysis, which found the atomic percentages ratio of Na, S and O equal to 2 : 1 : 4, and confirmed by Raman spectra (see Fig.

4.3.23), which displayed a main peak at 995 cm^{-1} referring to SO_4^{2-} symmetric stretching [87].

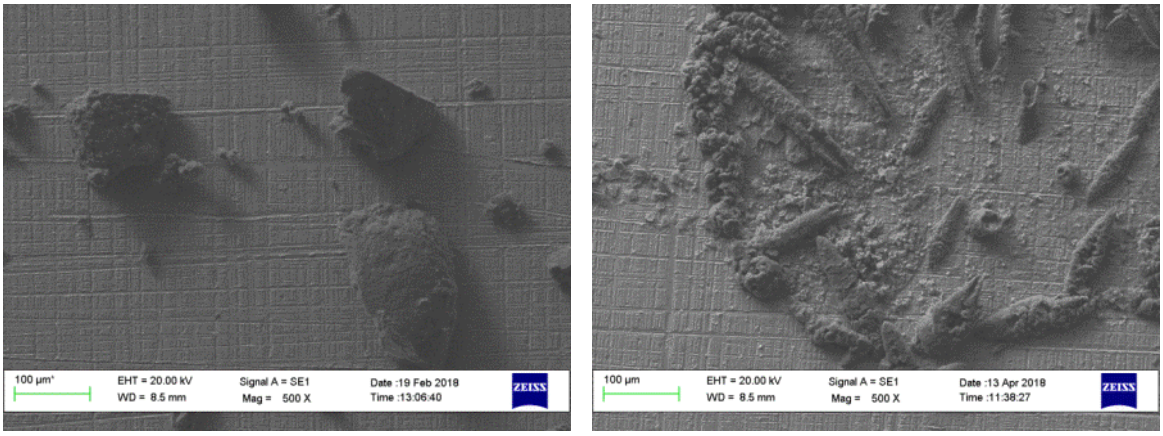

(a) (b)

Fig. 4.3.22: Na_2SO_4 "dry" at a) t0 ; b) t2: SEM images in secondary electron at 500x magnifications.

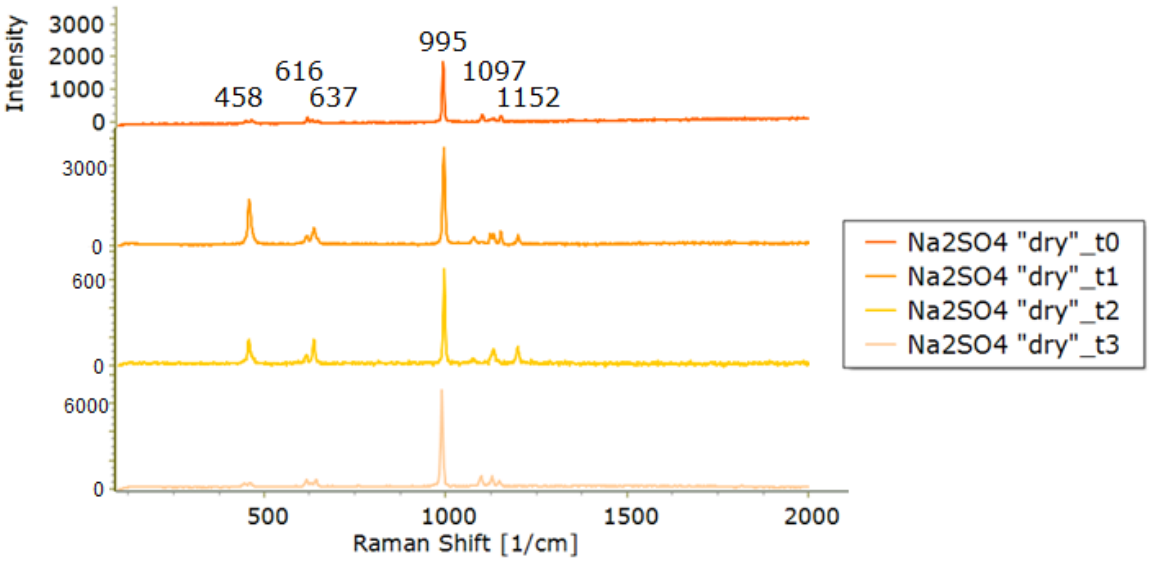

Fig. 4.3.23: Raman spectra of thenardite recorded on the Na_2SO_4 "dry" specimen from t0 to t3

At t1, in addition to thenardite crystals, which assume elongated geometries, species displaying Raman spectra similar to posnjakite ($Cu_4SO_4(OH)_6*H_2O$), which present at 971 cm^{-1} the SO_4^{2-} symmetric stretching Raman peak, were found.

At t2 the elongated crystals assumed circular disposal (see Fig. 4.3.22 (b)), and cuprite and similar to brochantite ($Cu_4(OH)_6SO_4$) species, presenting at 975 cm^{-1} a Raman peak corresponding to SO_4^{2-} symmetric stretching of brochantite [87], were identified.

At t3 Na_2SO_4 thenardite and brochantite, according to Raman and ATR-FTIR spectra analyses, were identified; assignments of the signals belonging to brochantite are reported in Table 21.

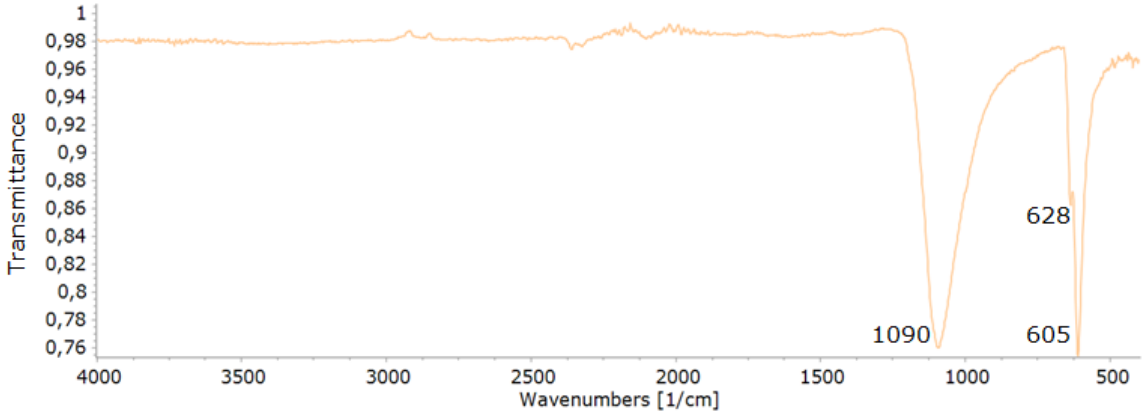

Fig. 4.3.24: ATR-FTIR spectrum

Table 21: Raman and ATR-FTIR bands of brochantite

Raman (cm^{-1})	ATR-FTIR (cm^{-1})	Assignment [87]
1101	1090	SO_4^{2-} asymmetric stretching
992		SO_4^{2-} symmetric stretching
647		SO_4^{2-} bending
632	628	
609	605	Cu-O stretching
464		Cu-O bending
449		SO_4^{2-} bending

Comparing the SEM images of the deposition drop border of the specimen Na_2SO_4 “wet” at t0 and at t1 (Fig. 4.3.25 (a) and (b)), it can be noticed that crystals rearranged in acicular and circular manners similarly to crystals on Na_2SO_4 “dry” at t2 (see Fig. 4.3.22 (b)), maybe because of the progessive retirement of the drying droplets. These residues at t0 were identified as thenardite, displaying Raman signals shifted towards higher wavenumbers with respect to thenardite on Na_2SO_4 “dry” at the same time (for example, the SO_4^{2-}

symmetric stretching falls at 992 cm^{-1} for the “wet” specimen, at 995 cm^{-1} for the “dry” one) [88], probably because of a higher hydration degree of the species on the “wet” specimen. In the central part of the deposition drop, hydrocerussite crystallites were found between t0 and t2. Raman peaks assignable to brochantite were found at t1 together with thenardite ones. Proceeding with the ageing, these crystals became thicker and thicker, and developed dendritic structures and rounded 3D acicular ones, presenting a habitus very similar to brochantite one, as it can be noticed by comparing Fig. 4.3.26 (a) and (b). EDX on 500x homogeneous area do not show significant C or O enrichments between t0 and t3.

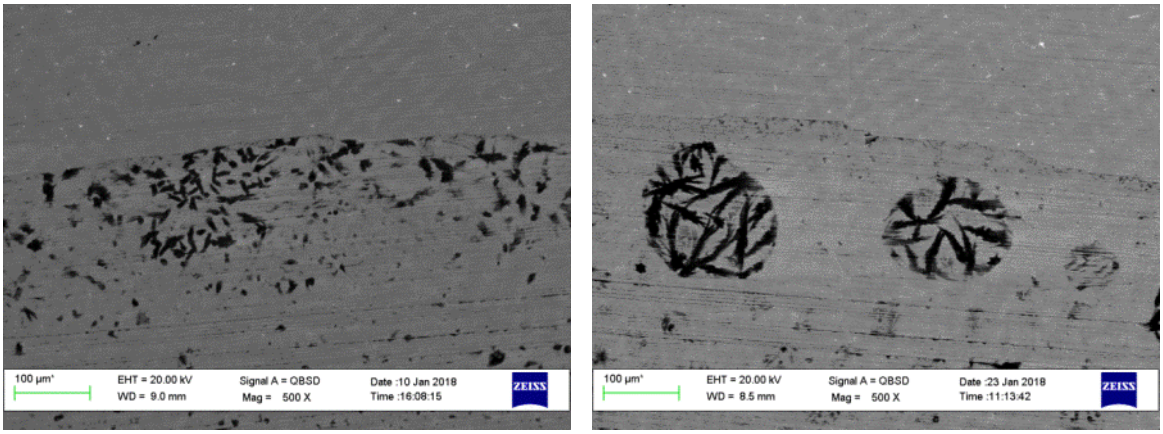

(a) (b)

Fig. 4.3.25: Na_2SO_4 “wet”, top arc view by SEM at 500x magnification a) at t0; b) at t1.

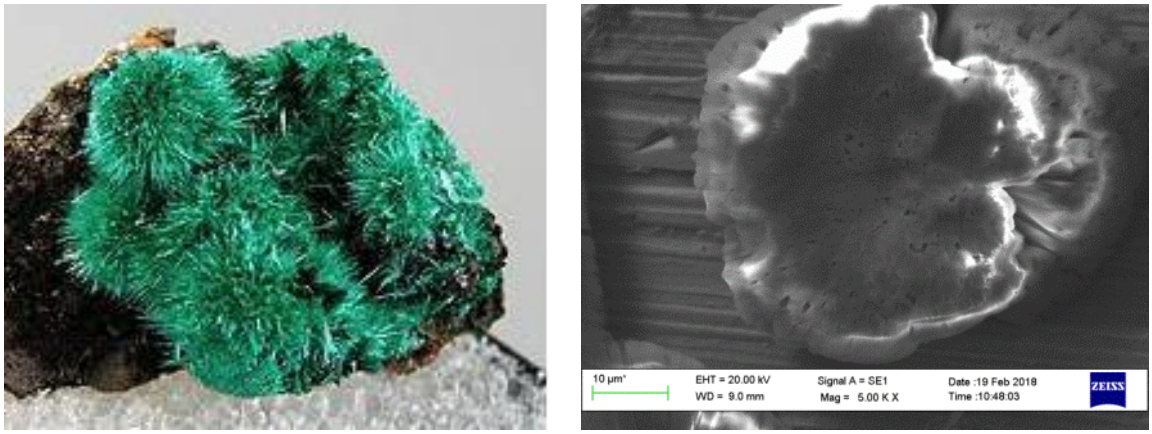

(a) (b)

Fig. 4.3.26: a) Macroscopic photo of brochantite [89]; b) Na_2SO_4 “wet”, SEM image at 500x magnification at t3 presenting acicular structures

4.3.1.5 NH_4NO_3

NH_4NO_3 "dry"

At t0, ammonium nitrate crystals were found to be recrystallized onto the specimen, showing Raman peaks at 1047 cm^{-1} for the NO_3^- symmetric stretching mode [90] (see Raman spectrum in Fig. 4.3.27).

At t1, residues onto the bronze surface resulted to be expanded with respect to t0. The presence of Pb nitrates was suggested both at t1 and t2 by EDX analyses, that found Pb, N and O atomic percentages in ratio 2 : 1 : 4 (possibly corresponding to $3PbO*Pb(NO_3)_2*3H_2O$).

At t2, in addition to Pb nitrates, also gerhardite or rouaite (both $Cu_2NO_3(OH)_3$) has been detected and identified by comparing EDX data (see box below Fig. 4.3.28) and Raman ones (see Fig. 4.3.28). The presence of these species was confirmed also at t3 by ATR-FTIR analysis (see Fig. 4.3.29 for the ATR-FTIR spectrum and Table 23 for the peak assignments).

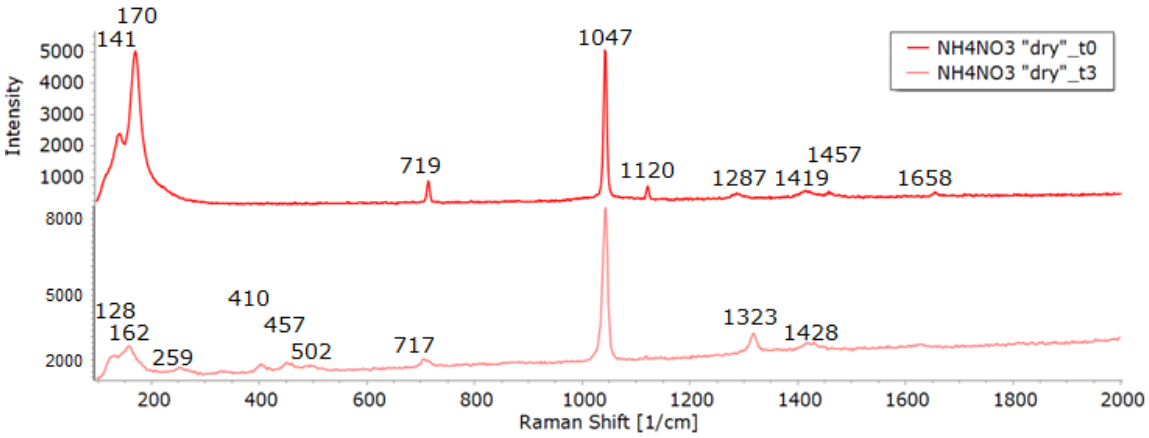

Fig. 4.3.27: Raman spectra of NH_4NO_3 dry" at t0 and t3

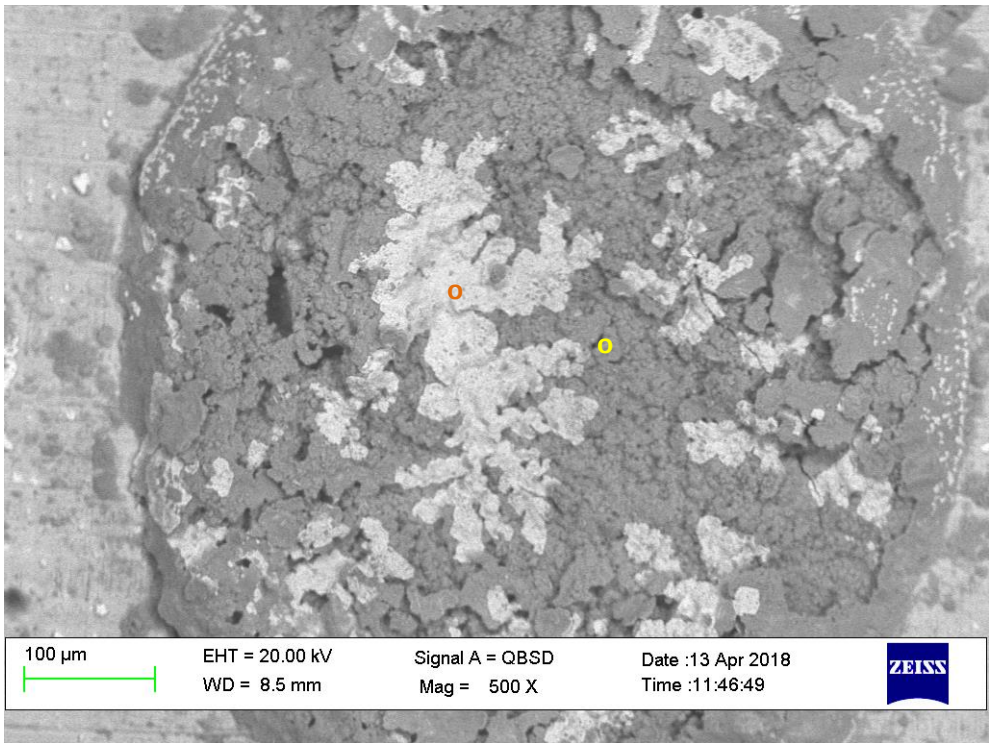

EDX - atomic %:	Assignment
o N K 21%, O K 67%, Cu K 5%, Pb M 4%	Pb nitrates
o N K 11%, O K 67%, Cu K 22%	$Cu_2(OH)_3NO_3$

Fig. 4.3.28: NH_4NO_3 “dry” at t2: SEM image in backscattered electrons at 500x magnification.

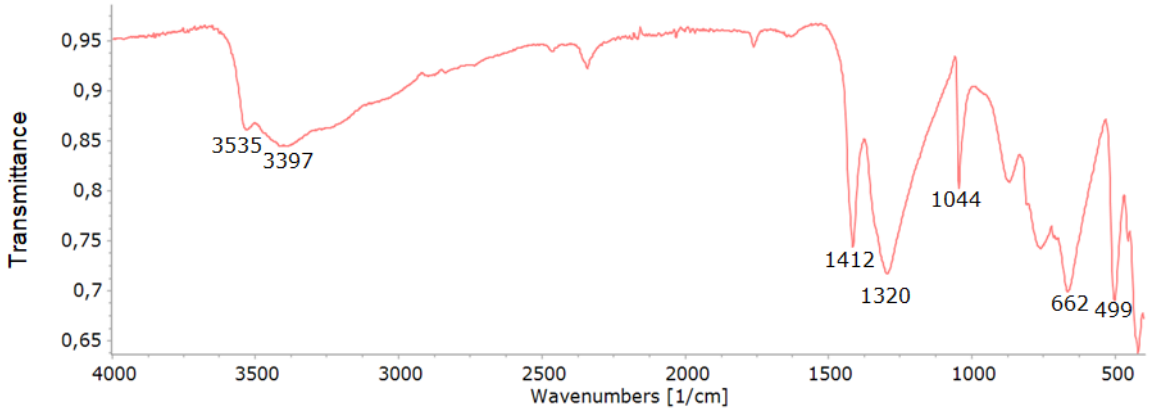

Fig. 4.3.29: ATR-FTIR spectrum of NH_4NO_3 “dry” at t3

Table 23: Raman and ATR-FTIR bands of $Cu_2NO_3(OH)_3$

Raman (cm^{-1})	ATR-FTIR (cm^{-1})	Assignment [91]
	3535	O-H asymmetric stretching
	3397	O-H symmetric stretching
1428	1412	NO_3^- asymmetric stretching
1323	1320	
1047		NO_3^- symmetric stretching
717		NO_3^- out of plane bending
	662	
502	499	O-Cu-O deformation
464		
449		
259		Lattice vibrations
162		
128		

NH_4NO_3 "wet"

The specimen treated with ammonium nitrate in a "wet" fashion is the one that results more unchanged over the whole ageing. At t0 a thick patina, constituted by hydrocerussite and ammonium nitrate by itself, was identified by EDX atomic percentages and Raman signals identification. Pb oxides were identified as needle-like residues mainly located around the border of the deposition drop. At t1, in addition to hydrocerussite, also Pb nitrates were found as corrosion product. Observing the Raman spectrum in Fig. 4.3.30, the NO_3^- symmetric stretching signal falls at 1039 cm^{-1}, therefore at lower wavenumber with respect to NO_3^- symmetric stretching of NH_4NO_3 at 1047 cm^{-1}, because of the Pb-N bond; similarly the NO_3^- out of plane bending mode, which falls at 717 cm^{-1} for ammonium nitrate, appears at lower wavenumbers (711 cm^{-1}). At t2 again hydrocerussite, Pb nitrates and oxides were found, as well as at t3. Hydrocerussite similar structures were found on the $NaNO_3$ "dry" specimen at t0 among the sodium nitrate crystals, as shown in Fig. 4.3.31; this feature can be explained by the fact that condensation water is found on the specimens around the salt residues, therefore between the salt crystals on the "dry" sample the concentration of nitrates and water during the ageing is high, promoting the formation of corrosion products even further than onto the "wet" corresponding

specimen. From the EDX analyses on homogeneous 500x area no particular enrichments in C or O between t0 and t3 were observed, probably because of the Pb nitrates and carbonates patina that hide the bronze surface against the direct contact with the atmosphere.

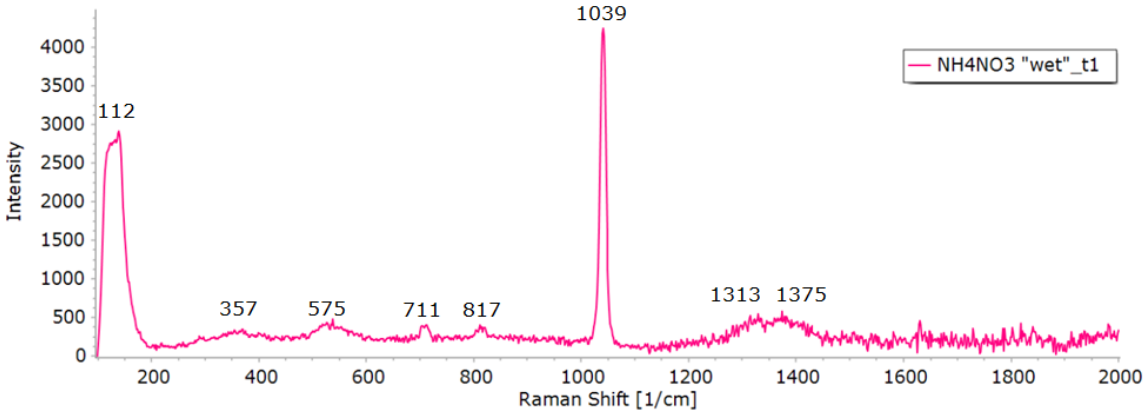

Fig. 4.3.30: Raman spectrum of NH_4NO_3 "wet" at t1

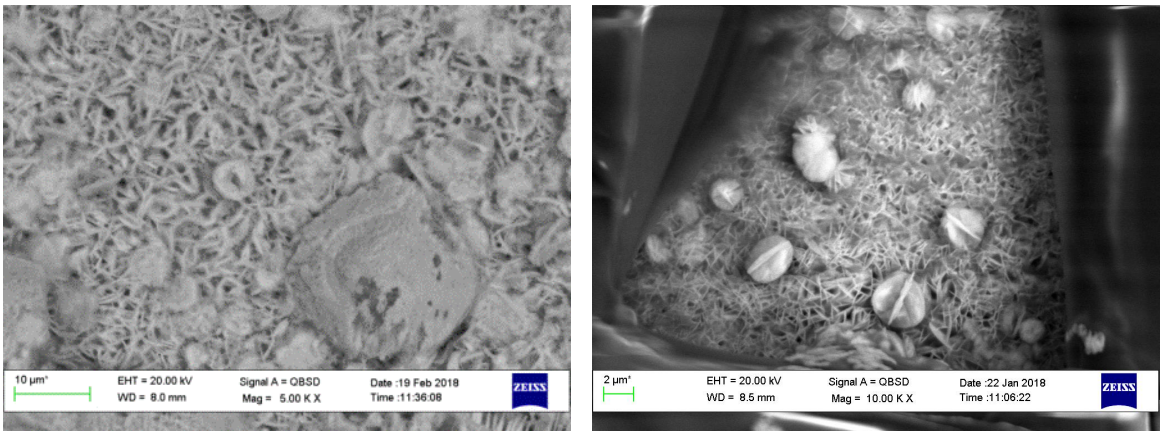

(a) (b)

Fig. 4.3.31: SEM images in backscattered electrons of a) NH_4NO_3 "wet" at t2; b) $NaNO_3$ "dry" (t0)

4.3.1.6 $(NH_4)_2SO_4$

$(NH_4)_2SO_4$ "dry"

At t0 the ammonium sulphate was found to be recrystallized onto the specimen; SO_4^{2-} symmetric stretching was found at 974 cm^{-1} [92]. During the ageing, residues that were at t0 onto the specimen tend to expand and to react with the substrate (see Fig. 4.3.32). At t2 and at t3 cuprite, brochantite and antlerite ($Cu_3SO_4(OH)_4$) were found. Raman spectrum and relative assignments are reported respectively in Fig. 4.3.33 and in Table 23.

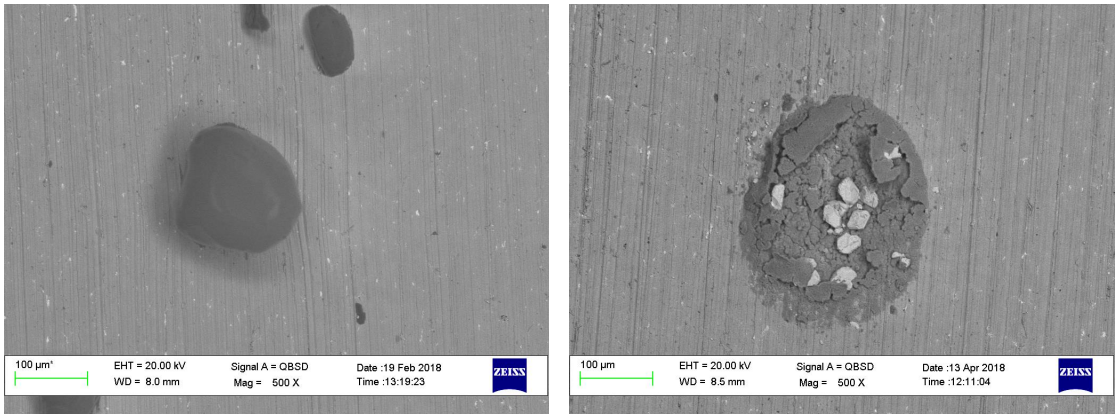

(a) (b)

Fig. 4.3.32: $(NH_4)_2SO_4$ "dry": SEM images in backscattered electrons at 500x magnification a) at t0; b) at t2.

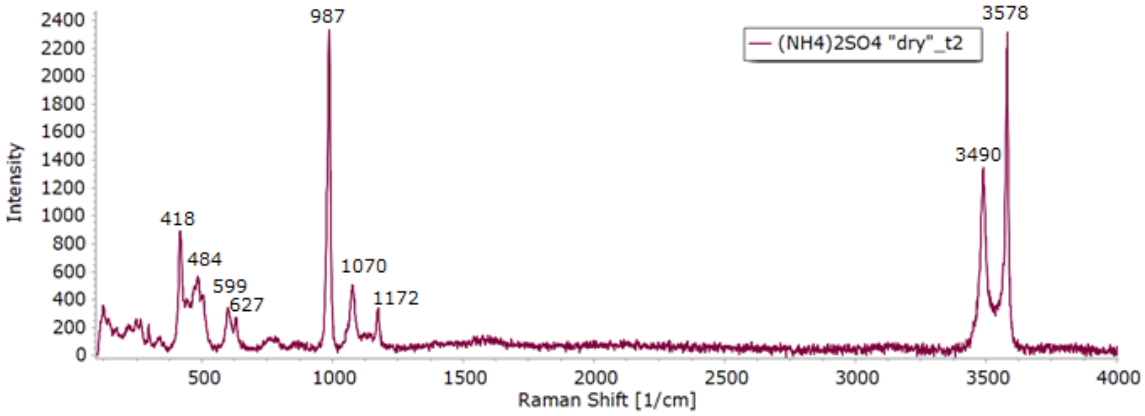

Fig. 4.3.33: Raman spectrum of antlerite recorded on $(NH_4)_2SO_4$ "dry" at t2

Table 23: Raman and ATR-FTIR bands of $Cu_3SO_4(OH)_4$

Raman (cm^{-1})	ATR-FTIR (cm^{-1})	Assignment [91]
3578		O-H asymmetric stretching
3490		O-H symmetric stretching
1172		SO_4^{2-} asymmetric stretching
1070		
987		SO_4^{2-} symmetric stretching
	672	SO_4^{2-} bending
627		
599		Cu-O stretching
484		O-Cu-O deformation
418	421	

$(NH_4)_2SO_4$ "wet"

At t0, ammonium sulphate was found to be partially recrystallized and to have partially reacted with the bronze surface, producing corrosion products whose identification was done by Raman peaks analyses. The main species that were detected are posnjakite and chalcanthite ($CuSO_4*5H_2O$); SO_4^{2-} symmetric stretching values recorded by Raman analyses for each species are listed in Table 24 [91]. Residues onto the $(NH_4)_2SO_4$ "wet" specimen do not seem to have changed so much their morphologies from t0 to t1, but residues have lost their defined shape and became more filamentous (see Fig. 4.3.34 (a) and (b)). Observing the Raman spectra at t1 and t2, one peak at 980 cm^{-1} could be assigned to the SO_4^{2-} symmetric stretching of anglesite ($PbSO_4$), but it is no more found at t3; it can be noticed that the K_{sp} of anglesite is $1,6*10^{-8}$ at 25°C [92], higher than the corresponding carbonate one (K_{sp} $7,4*10^{-14}$ at 25°C), therefore the absence of anglesite detection at t3 can be explained by dissolution of lead sulphate during the ageing and Pb inclusion in less soluble products as hydrocerussite. At t2, residues that were previously identified as posnjakite appear to be more and more dissolved, as it can be observed in Fig. 4.3.35, which represents the t2 stage of the area displayed in Fig. 4.3.34; Raman signals similar to antlerite's ones are observed. At t3, posnjakite and antlerite have been identified by Raman analyses (see Table 25 for the SO_4^{2-} symmetric stretching); a weak Raman signal at 1048 cm^{-1} could be ascribed to CO_3^{2-} symmetric stretching of hydrocerussite. The EDX analysis on homogeneous area at 500x magnification did not show significant C and O uptakes between t1 and t3; it is interesting to notice that Pb was not detected, while other salt treatments provoqued lead inglobation into corrosion products; sulphtes seem therefore to not favour the Pb mobilization as other anoins do.

Table 24: Raman shift of SO_4^{2-} symmetric stretching (cm^{-1}) [91]

986	Chalcanthite ($CuSO_4*5H_2O$)
983	Antlerite ($Cu_3(SO_4)(OH)_4$)
975	Posnjakite ($Cu_4(SO_4)(OH)_6*(H_2O)$
968	Ammonium sulphate ($(NH_4)_2SO_4$)

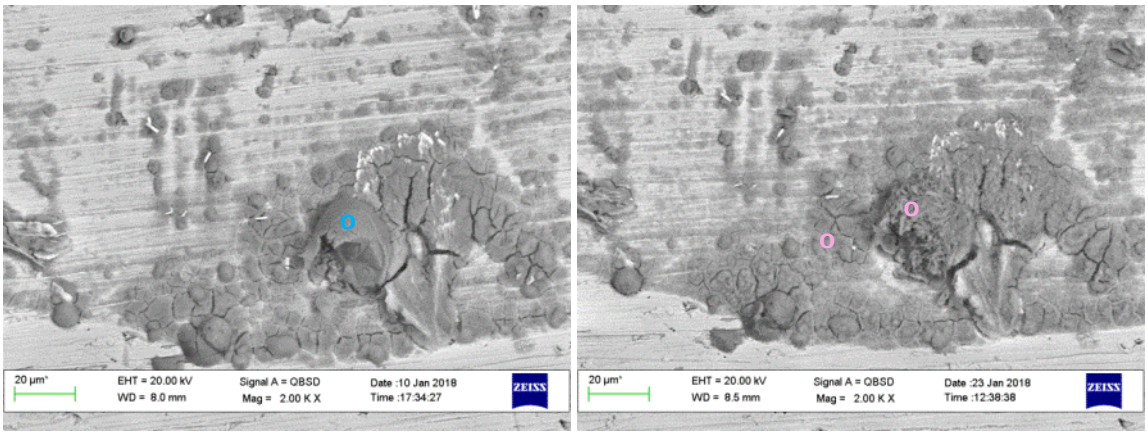

(a) (b)

EDX - atomic %:	Assignment
o N K 2%, O K 67%, S K 8%, Cu K 15%	$(NH_4)_2SO_4$, Cu sulphates
o O K 72%, S K 6%, Cu K 22%	$(Cu_4(SO_4)(OH)_6*(H_2O)$

Fig. 4.3.34 : $(NH_4)_2SO_4$ "wet", bottom arc view by SEM at 200x magnification a) at t0; b) at t1

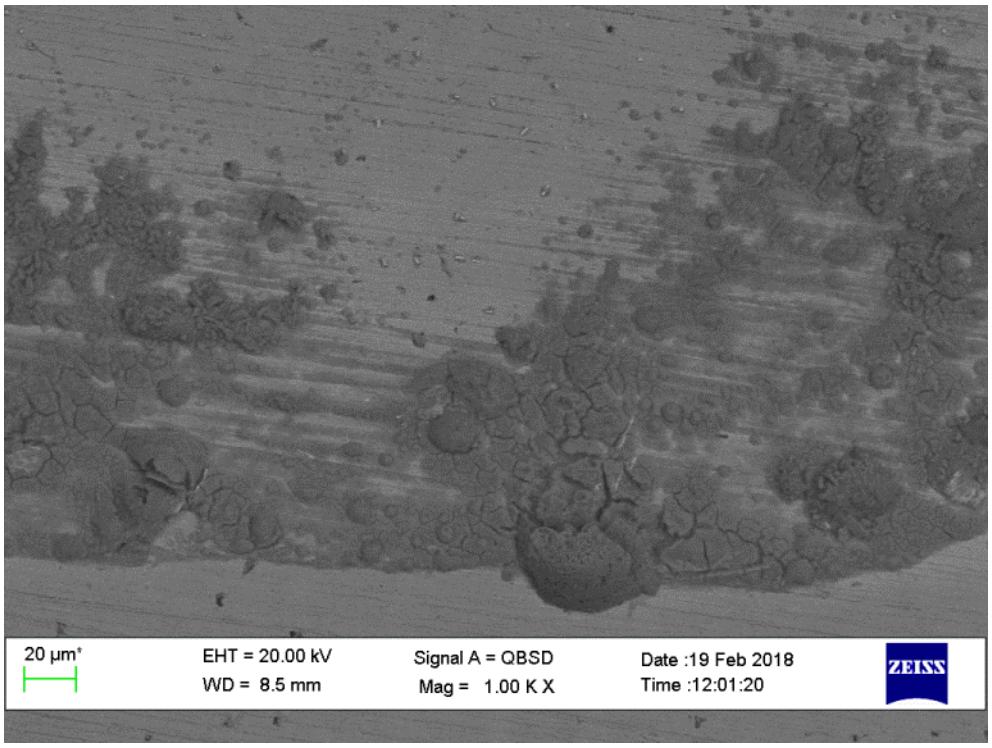

Fig. 4.3.35: $(NH_4)_2SO_4$ "wet", SEM image in backscattered electrons at 1000x magnification at t2

4.3.1.7 To sum up

Here below the evolutions of corrosion products that were identified on each specimen over the whole accelerated ageing are reported. It can be noticed that at t0 on the "dry" specimens the deposited salts have recrystallized, while at t0

on the “wet” samples these salts have already reacted with the substrates in most of the cases, producing cuprite and Pb carbonates and oxides on every specimen and peculiar corrosion products depending on the anion (clinoatacamite for NaCl, Pb nitrates for $NaNO_3$, posnjakite and chalcanthite for $(NH_4)_2SO_4$); these products are the same encountered firstly in dropping studies on bronzes [8]. The corrosion products that are formed are the same for equal salts, but appear at different times according to the deposition modality: as an example, considering the “dry” blank specimen hydrocerussite appears just at t3, while the same substance is formed at t0 onto the “wet” blank specimen; in other cases, generally the time difference between the appearence of a species in the “dry” and in the “wet” samples corresponds to almost one week. The “wet” deposition modality induces the formation of several corrosion products at the same time, while the “dry” mode allows to separate the formation of corrosion products over time, requiring further ageing to obtain the corresponding phases found in the “wet” samples. The evolutions of corrosion products that were observed in this study correspond to literature data on the bronze patinas evolutions [21] (see section 2.2).

Samples which presented less modifications are the ones treated with sodium nitrate, while the corresponding ammonium salt allows the development of gerhardite or rouaite on the substrates, probably because of pH influences: while the sodium salt application leads to a surface pH around 5 all over the ageing, the ammonium salt induces a surface pH shift from 5 to 7 ranging from t0 to t3. Pb nitrates are usually not found in patinas because they are soluble products (K_{sp} 5,88 at 25°C [93]), which can be washed away by water in case of inclinated surfaces or which can be redissolved during deliquescences and the Pb is trapped in less soluble products as Pb carbonates (K_{sp} $7{,}4*10^{-14}$ at 25°C [93]) and oxides (K_{sp} $2{,}4*10^{-5}$ at 25°C [94]). Some differences in corrosion implications between the Na^+ and the NH_4^+ cations can be derived by considering that only on the ammonium-containing samples gerhardite (spreading NH_4NO_3) and antlerite (spreading $(NH_4)_2SO_4$) were formed, while on the specimens treated with the corresponding anions and sodium as counterion these phases were not found. Malachite, brochantite, gerhardite, atacamite and antlerite are corrosion products that develop in bronze patinas after years of exposure, therefore the accelerated ageing methodology worked properly simulating them, using the

calculated amounts of salts (see section 3.2) within three weeks repeating the set general ageing cycle; evolutions of corrosion products over time that were observed in this study correspond to ones reported in literature [21]. In particular, malachite is reported in literature to be a difficult phase to obtain artificially on bronzes by cuprite conversion, therefore it is an interesting achievement for this accelerated ageing methodology.

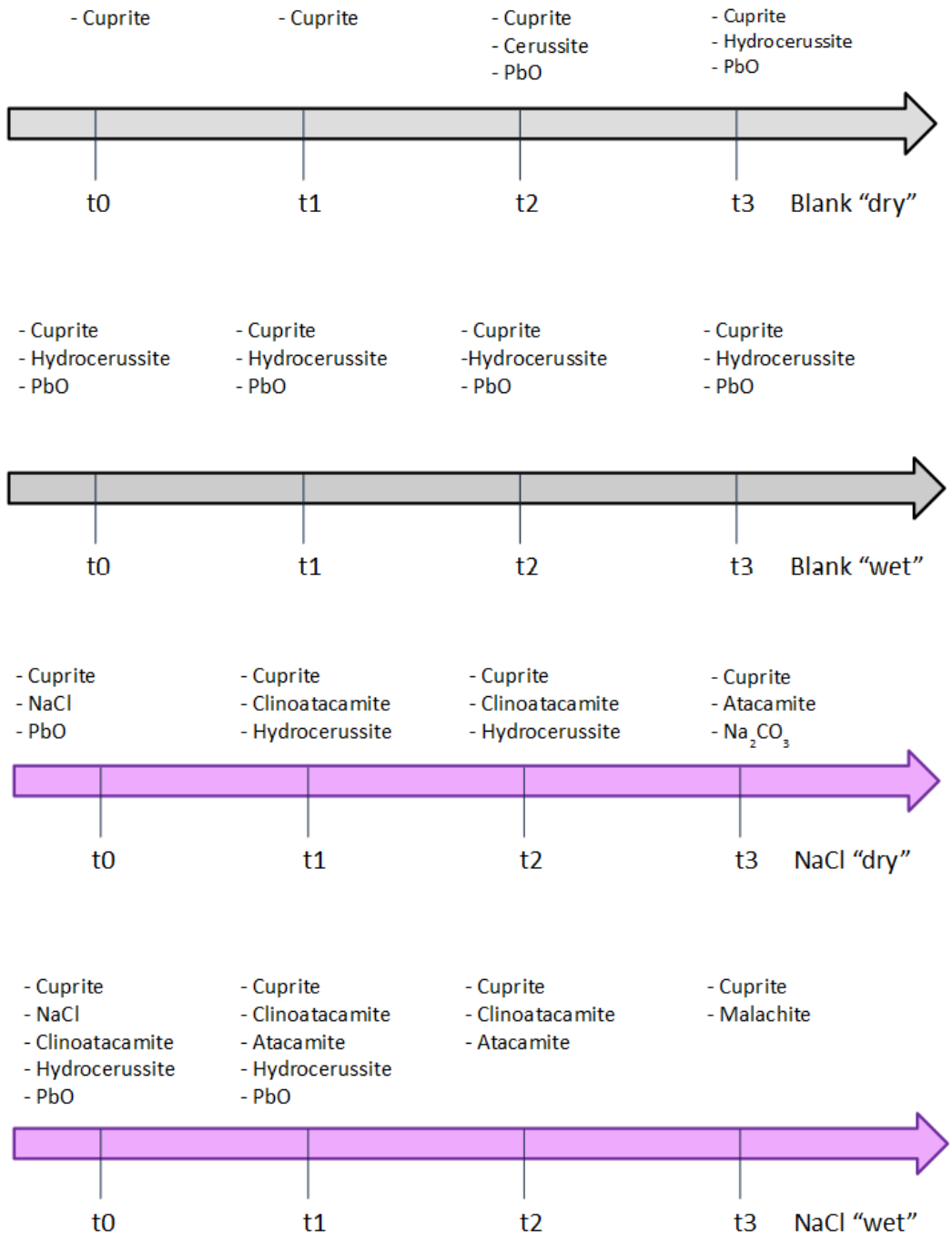

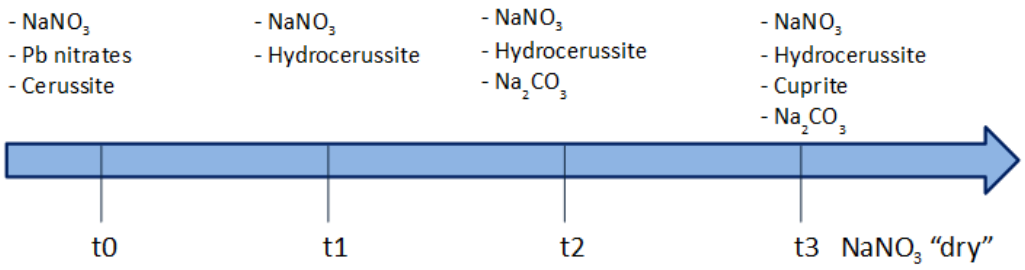
- $NaNO_3$
- Pb nitrates
- Cerussite
- $NaNO_3$
- Hydrocerussite
- $NaNO_3$
- Hydrocerussite
- Na_2CO_3
- $NaNO_3$
- Hydrocerussite
- Cuprite
- Na_2CO_3
t0
t1
t2
t3 $NaNO_3$ "dry"

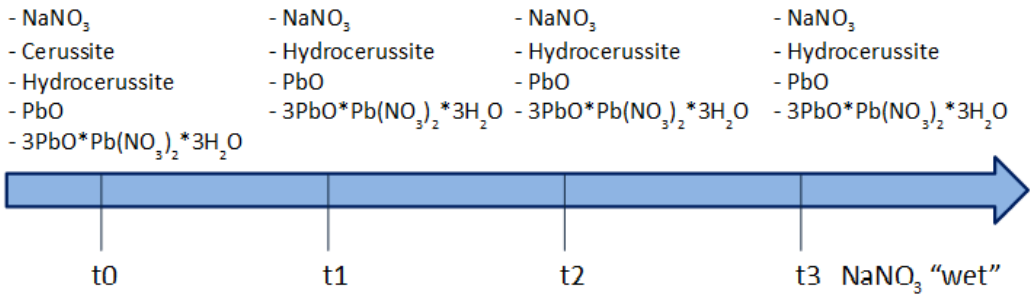
- $NaNO_3$
- Cerussite
- Hydrocerussite
- PbO
- $3PbO*Pb(NO_3)_2*3H_2O$
- $NaNO_3$
- Hydrocerussite
- PbO
- $3PbO*Pb(NO_3)_2*3H_2O$
- $NaNO_3$
- Hydrocerussite
- PbO
- $3PbO*Pb(NO_3)_2*3H_2O$
- $NaNO_3$
- Hydrocerussite
- PbO
- $3PbO*Pb(NO_3)_2*3H_2O$
t0
t1
t2
t3 $NaNO_3$ "wet"

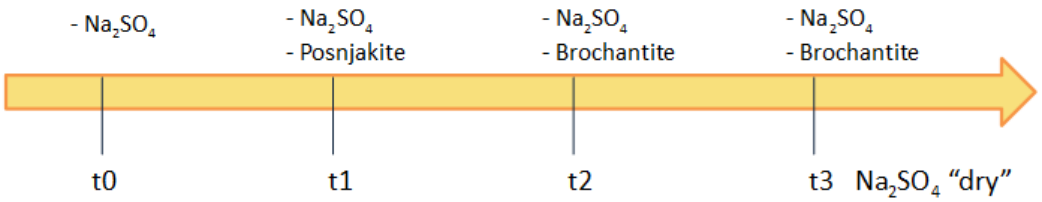
- Na_2SO_4
- Na_2SO_4
- Posnjakite
- Na_2SO_4
- Brochantite
- Na_2SO_4
- Brochantite
t0
t1
t2
t3 Na_2SO_4 "dry"

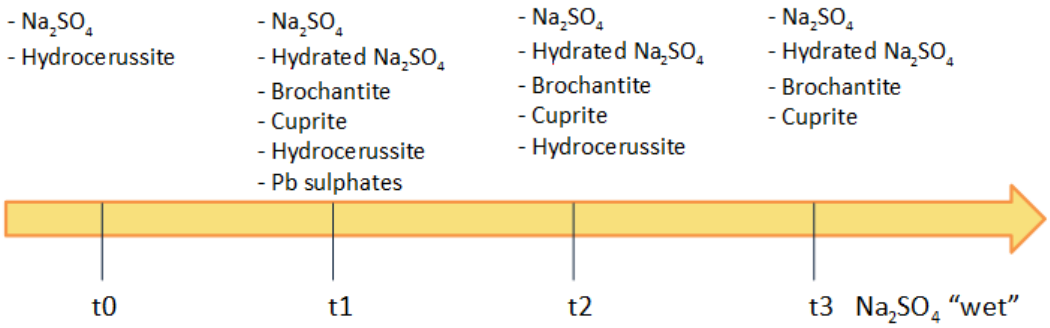
- Na_2SO_4
- Hydrocerussite
- Na_2SO_4
- Hydrated Na_2SO_4
- Brochantite
- Cuprite
- Hydrocerussite
- Pb sulphates
- Na_2SO_4
- Hydrated Na_2SO_4
- Brochantite
- Cuprite
- Hydrocerussite
- Na_2SO_4
- Hydrated Na_2SO_4
- Brochantite
- Cuprite
t0
t1
t2
t3 Na_2SO_4 "wet"

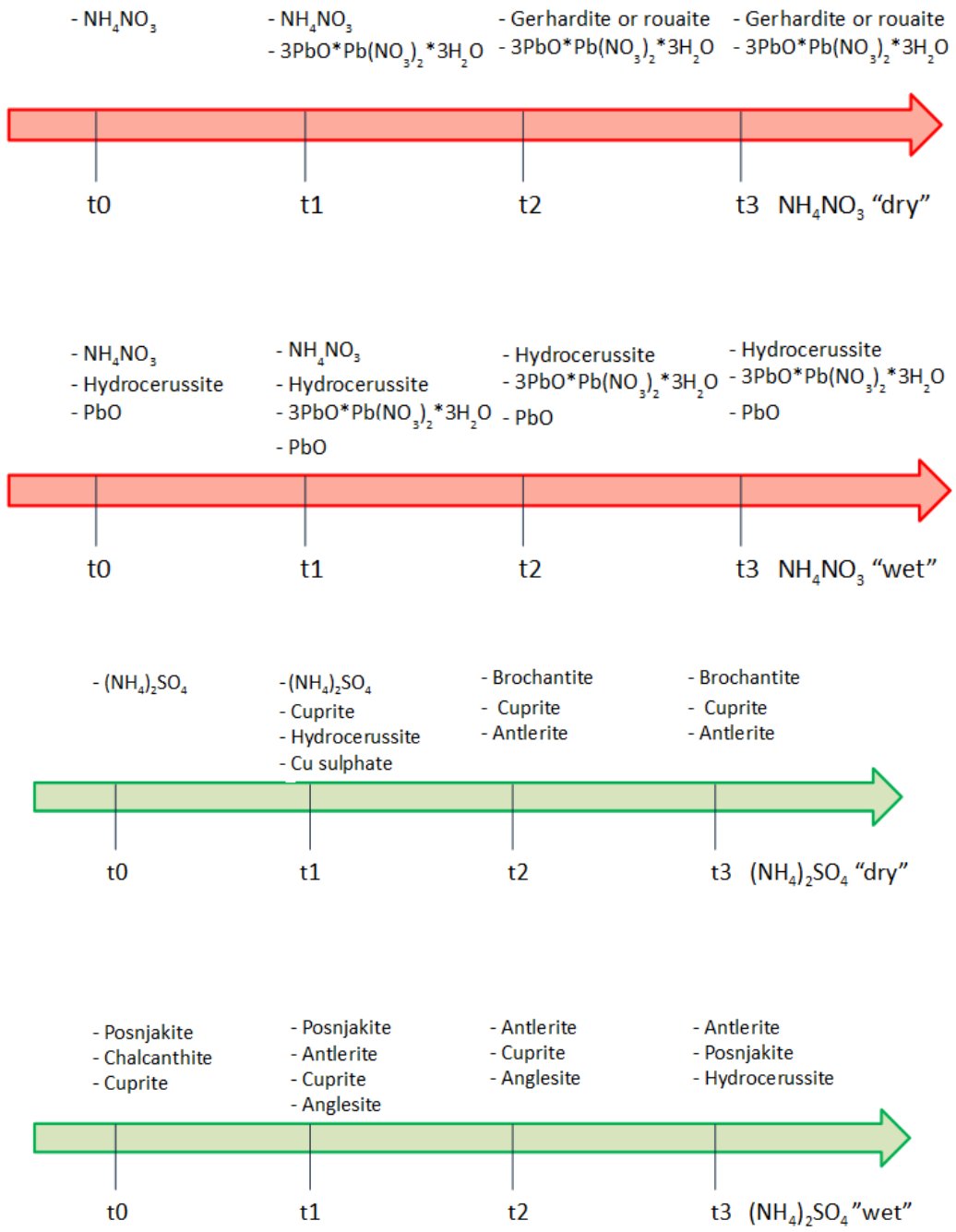

4.3.2 Ternary mixture

Ternary mixture "dry"

At t0 salts that were spread onto the specimen were found to be recrystallized (see Fig. 4.3.36); euhedral cubes of NaCl (EDX atomic percentages of Na and Cl equal to 1 : 1, Raman silent salt), $NaNO_3$ (identified by EDX analyses and by the Raman peak of NO_3^- symmetric stretching at 1058 cm^{-1}) and Na_2SO_4 (identified by EDX analyses and by the Raman peak of SO_4^{2-} symmetric stretching at 990

cm^{-1}) were visible. In addition to these species, in some areas nitrates and sulphates were found to be recrystallized together; this observation is in agreement with E-AIM predictions regarding which solid species could form in a simplified system, containing Na^+, Cl^-, NO_3^- and SO_4^{2-} only, at T 25°C and RH 40-70% (see section 4.1.2, Table 11 for examples). The model assumes that over RH 39% NaCl, $NaNO_3$ and $NaNO_3*Na_2SO_4*H_2O$ are found in solid phase; the model does not consider the interaction with the elements of the bronze substrate, but as a first approximation, it works well for this step of the ageing in which salt species still have to react properly with copper and lead.

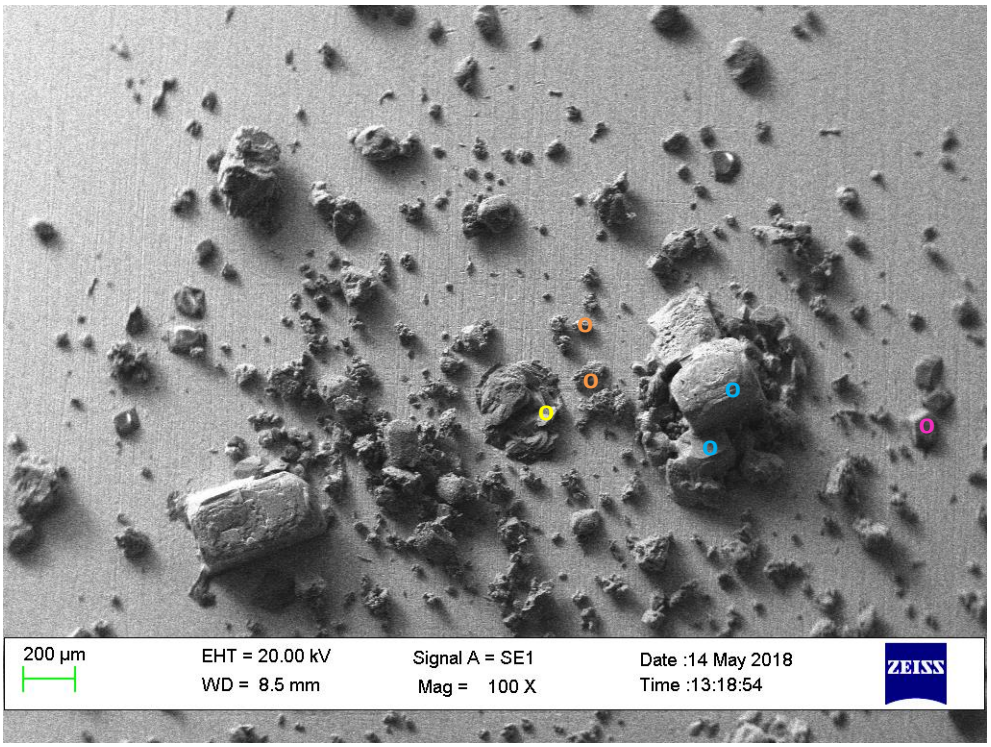

EDX - atomic %:	Assignment
o Na K 50%, Cl K 50%	NaCl
o Na K 28%, S K 14%, O K 56%	Na_2SO_4
o Na K 16%, O K 59%, N K 13%, S K 7%	$NaNO_3*Na_2SO_4*H_2O$
o Na K 20%, O K 60%, N K 20%	$NaNO_3$

Fig. 4.3.36: Ternary mix “dry”, SEM image at 250x magnification at t0

At t3 Na_2SO_4 and NaCl were found to be recrystallized. Cuprite formation and passivation beginning were detected by Raman analyses. Again structures constituted by sulphates and nitrates were found; this association in a hydrated

phase can explain the shift of NO_3^- symmetric stretching at higher frequencies (around 1057-1062 cm^{-1}). Some sulphate and chloride crystals were observed to have grown interpenetrated (see Fig. 4.3.37). but no corrosion products were observed looking on the surface.

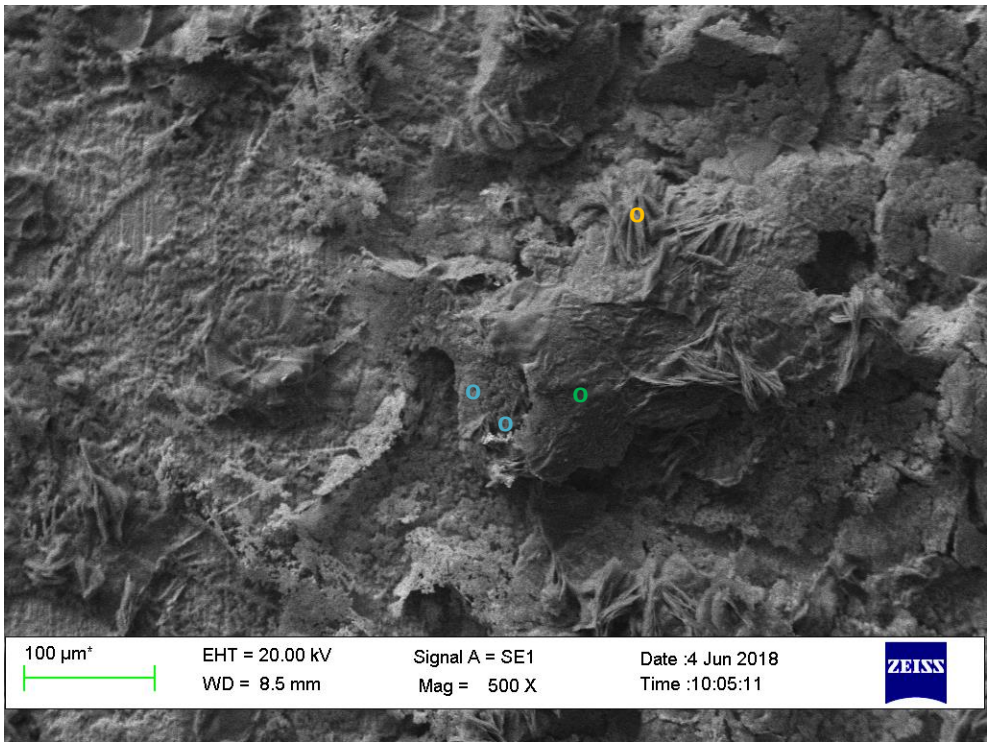

EDX - atomic %:	Assignment
o Na K 27%, O K 60%, S K 12%	Hydrated Na_2SO_4
o N K 12%, O K 60%, Na K 20%, S K 8%	$NaNO_3$*Na_2SO_4*H_2O
o Na K 22%, O K 63%, S K 8%, Cl K 7%	NaCl, Na_2SO_4*$10H_2O$

Fig. 4.3.37: Ternary mix “dry” at t3: SEM image at 100x magnification.

Ternary mix “wet”

The ternary mix “wet” at t0 was covered by hydrocerussite; almost the same morphologies were observed at t3, identified as Pb carbonates, in the form of hydrocerussite, and Pb oxides, in the form of massicot. From the EDX analyses on 500x homogeneous area, it is possible to notice a Pb and O enrichment on the surface from t0 to t3; the lower Cu, Zn and Sn amounts are due to the formation of a massive patina that covers more and more the substrate (see Table 27 for EDX data). Cuprite could be present below this patina and it could

be found by removing part of the residues, as it was found in the case of the other specimens by post-pickling analyses.

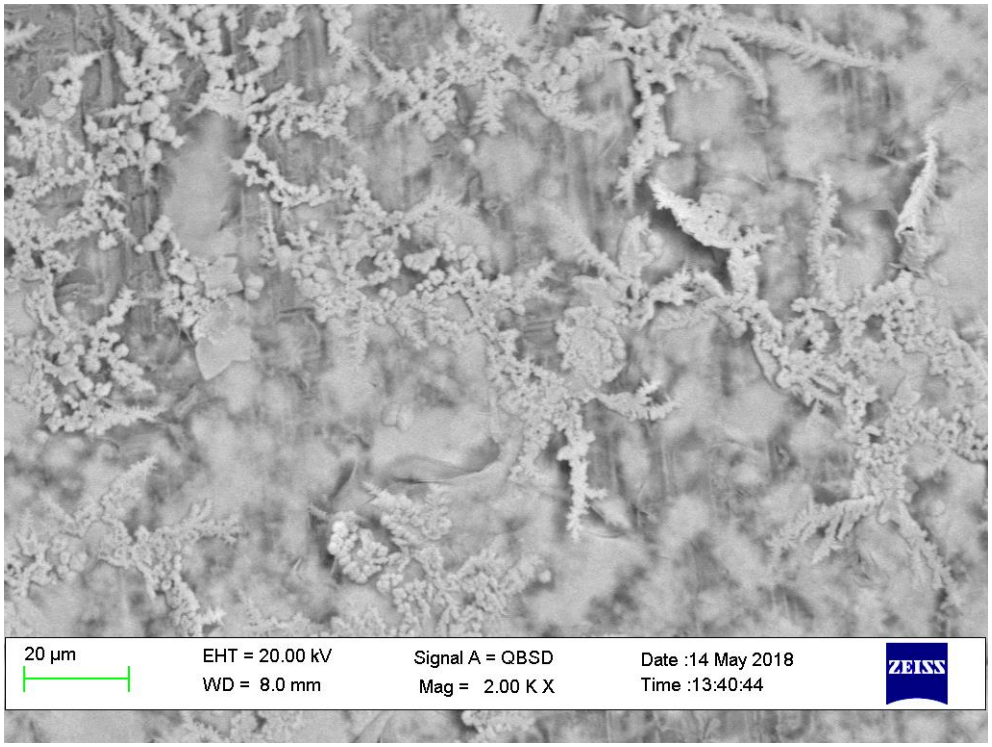

Fig. 4.3.38: Ternary mix “wet” at t0: SEM image in backscattered electron at 2000x magnification.

Table 27: EDX analyses on 500x homogeneous area of ternary mix “wet”

Element	Atomic percentage (%)	
	t0	t3
C	30	28
O	36	41
Cu	25	20
Pb	8	10

4.3.2 Mixture simulating natural PM samples

“Matrix” sample

At t0, the SEM observations confirm a quite homogeneous distribution of the species over the surface of the “matrix” sample (see Fig. 4.3.39). A lot of fluorescence, probably due to the humic acids component, disturbs the Raman signals; the main recognizable Raman peaks belong to calcite ($CaCO_3$), that displays a peak at 1082 cm^{-1} corresponding to the CO_3^{2-} symmetric stretching

mode, Pb oxides and carbonates, cuprite and carbon. At t3 some residues were found to be migrated from the central area to the borders, leaving the inner part of the specimen less covered; no massive structures developed by corrosion products were detected.

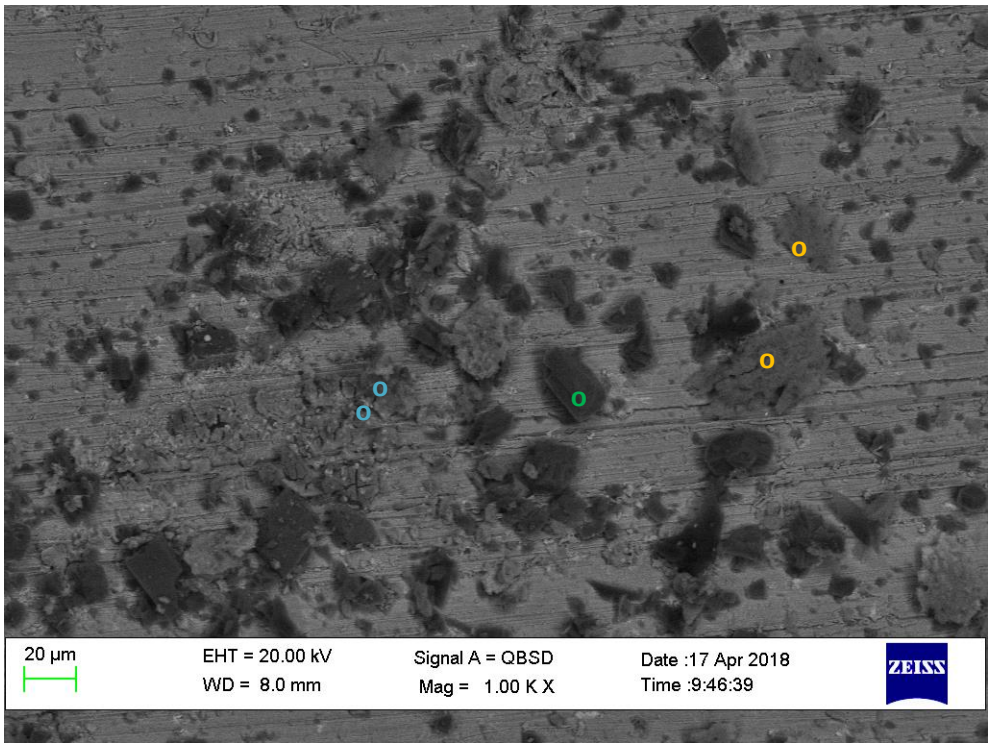

EDX - atomic %:	Assignment
o C K 48%, O K 42%, Ca K 5%, Pb M 3%	$CaCO_3$, $PbCO_3$
o C K 55%, O K 25%, Al 1%, Si 2%, Ca K 2%, Ti K 0.1%, Fe K 0.3%, Cu 11%, Pb M 2.74%	Char
o C K 20%, O K 60%, Ca K 20%,	$CaCO_3$

Fig. 4.3.39: “Matrix” sample, SEM image in backscattered electrons at 1000x magnification at t0

“Matrix+salts” sample

The “matrix+salts” sample at t0 displays some peculiarities due to the salts presence: as it is shown in Fig. 4.3.40 (a), dendritic structures constituted by Na, Cl, N and O are visible. According to Fig. 4.3.40 (a), it seems that NaCl cubes tend to modify their morphology to cross-shaped ones, which resemble the dendrites structures. By Raman spectroscopy it was possible only to identify $NaNO_3$ and carbon; further signals were not visible because of the intense fluorescence as in the “matrix” sample. At t3 dendrites are no more visible (see

Fig. 4.3.40 (b)); Raman spectroscopy allowed to identify carbon (G-band at 1578 cm^{-1} , D-band at 1376 cm^{-1} [94]), $NaNO_3$ (NO_3^- symmetric stretching at 1062 cm^{-1} [85]) and cuprite (see Raman spectrum in Fig. 4.3.41). The whole sample looks more “cemented” with respect to the “matrix” one by observing them by SEM.

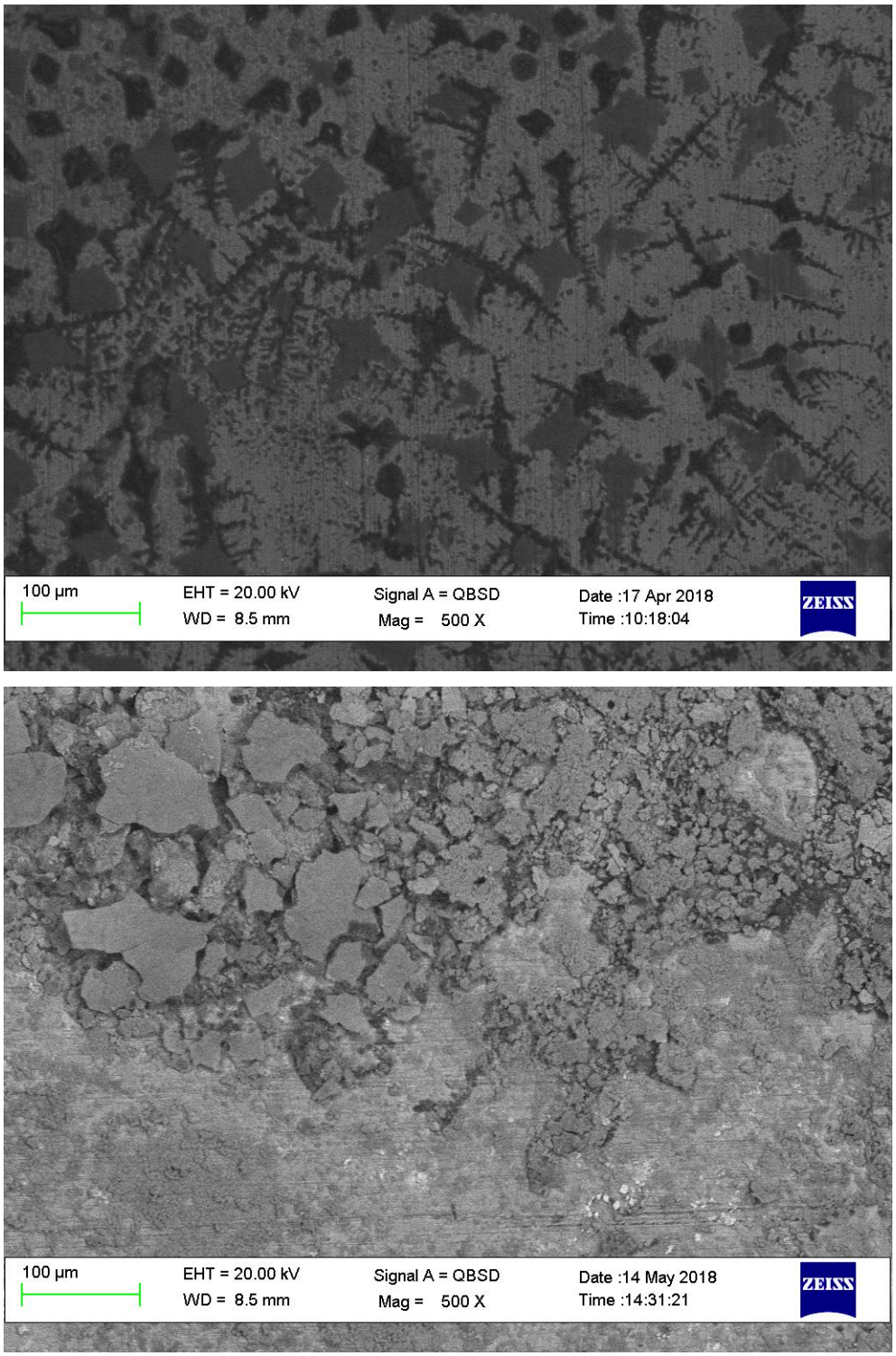

Fig. 4.3.40: “Matrix+salts” sample a) at t0; b) at t3: SEM image in secondary electrons at 500x magnification

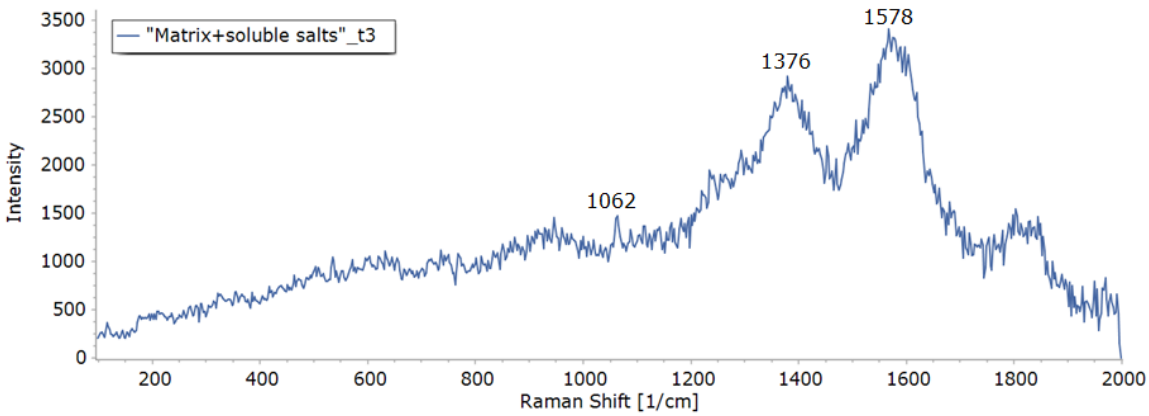

Fig. 4.3.41: Raman spectrum recorded on “matrix+salts” sample at t3

4.3.3 Natural PM

The sample where natural PM was applied by using a high volume sampler, presented a homogeneous distribution of residues from t0 to t3 (see Fig. 4.3.42 (a) and (b)). From the EDX analyses, it was not straightforward to make assignments, while morphologies were useful to discriminate residues like pollen ones. From the Raman analyses just carbon and calcite were recognizable at both t0 and t3, as a too much strong fluorescence was hiding further signals.

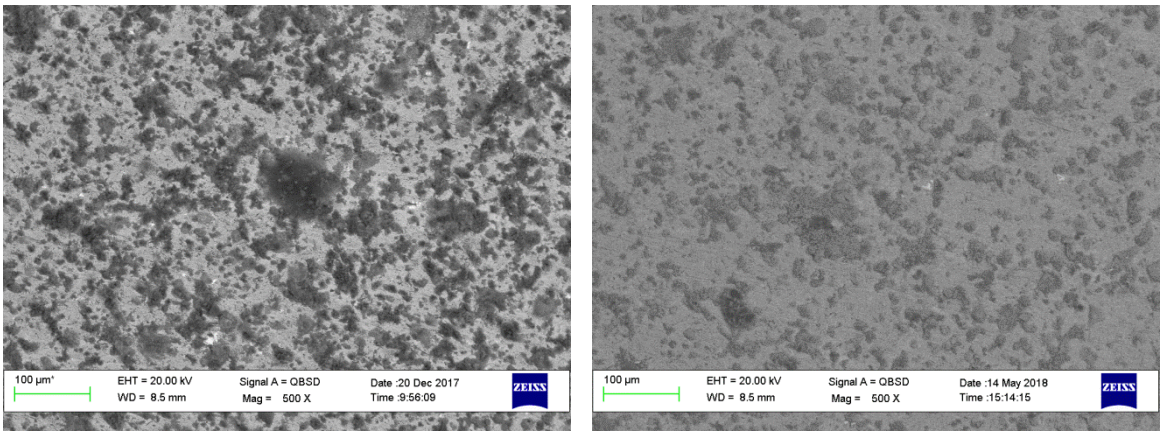

(a) (b)

Fig. 4.3.42: “Impacted PM” sample, SEM images in backscattered electrons at 500x magnification a) at t0; b) at t3

The specimen covered with natural PM was not submitted to destructive procedures yet (as pickling, removal of residues and successive profiling and Raman analyses); at the moment the microscopic aspect of the sample is similar to the one of the “matrix+salts” specimen.

4.4 Analyses on pickled samples and pickling solutions

Beside surface analyses in order to investigate the formation and the evolution of corrosion products, an attempt to performe some quantitative comparison among aged specimens was done. Specifically, all specimens were pickled and for the “wet” ones weight losses together with the metals in pickling solutions were determined, while for the “dry” ones profile analyses were performed.

According to data reported in Table 27, concerning weight losses corresponding to equal areas, the highest weight losses concerning the “wet” samples were displayed (in decreasing order) by: $(NH_4)_2SO_4$ > NaCl ~ NH_4NO_3 > Na_2SO_4 ~ blank “wet” > $NaNO_3$. Further data on the metals that were involved in corrosion products formation are reported in Table 28, concerning AAS data. From the AAS data it appears that the most of copper, zinc and tin were involved in corrosion products on the NaCl “wet” sample, in amounts of one order of magnitude higher than in the case of the other specimens; according to the Cu/Sn ratio in the alloy around 4 : 1, NaCl results to have mobilized mainly copper. Regarding lead, the most of it was found in the pickling solution of $(NH_4)_2SO_4$ “wet”, even though it has to be reminded that the Pb distribution in the bronze cast is not uniform and therefore, because of the poor statistics given by the small size of the samples, the Pb data have to be considered just qualitatively. Comparing the weight losses and the AAS data, NaCl and $(NH_4)_2SO_4$ fit in both the cases as the samples that were more corroded, even though in reverse order. The fact that NaCl “wet” results the sample that involved the most copper in corrosion products is in agreement with bronze cancer and its implications; its lower weight loss with respect to $(NH_4)_2SO_4$ “wet” can be explained by the formation of products onto the specimen which adhere better to the bronze surface: in fact, a few reddish residues were left onto the NaCl “wet” after pickling, while no residues were visible onto the other specimens.

From the SEM-EDX analyses, it was observed on some specimens, in particular on “dry” ones, the occurrence of pitting since early stages of the ageing, therefore profiling analyses were performed in order to understand the depth of the formed holes. Concerning the profiling analyses onto the pickled specimens,

almost flat profiles were encountered on the “wet” specimens, showing that the pitting that was observed by SEM was not particularly pronounced. On the other hand, “dry” specimens display some peculiar features in their profiles: NH_4NO_3 “dry” presents the highest Rt evaluated by profiling analyses (22,9 μm), which corresponds also to Rmax; these values correspond to the hole formed under the biggest residue onto the specimen at t3 (see Fig. 4.4.1). Other interesting specimens for the pitting are NaCl “dry”, which presents Rt and Rmax equal to 14,1 μm, and $(NH_4)_2SO_4$ “dry”, which displays Rt equal to 12,0 μm. NH_4NO_3 “dry” results to be the salt that has interacted more in depth with the bronze substrate, considering the depth of holes left by the removal of corrosion products (see comparison of profiles in Fig. 4.4.2).

Table 27: Weight losses associated with “wet” samples

Sample	Weight loss (g)
Blank “wet”	0,0002±0,0001
NaCl “wet”	0,0003±0,0001
$NaNO_3$ “wet	0,0001±0,0001
Na_2SO_4 “wet”	0,0002±0,0001
NH_4NO_3 “wet	0,0003±0,0001
$(NH_4)_2SO_4$ “wet”	0,0004±0,0001

Table 28: AAS data on pickling solutions

Sample	Cu (μg/cm^2)	Zn (μg/cm^2)	Sn (μg/cm^2)	Pb (μg/cm^2)
Blank “wet”	10,4±1,0	1,3±0,1	0,6±0,2	0,7±0,1
NaCl	263±29	10,3±1,0	1,3±0,2	0,27±0,03
$NaNO_3$	24±2	3,4±0,3	1,5±0,2	0,08±0,02
Na_2SO_4	14,6±1,5	1,5±0,2	0,5±0,1	0,18±0,02
NH_4NO_3	18,7±1,9	2,1±0,2	0,7±0,1	0,30±0,03
$(NH_4)_2SO_4$	52±5	2,4±0,2	0,8±0,1	1,8±0,2

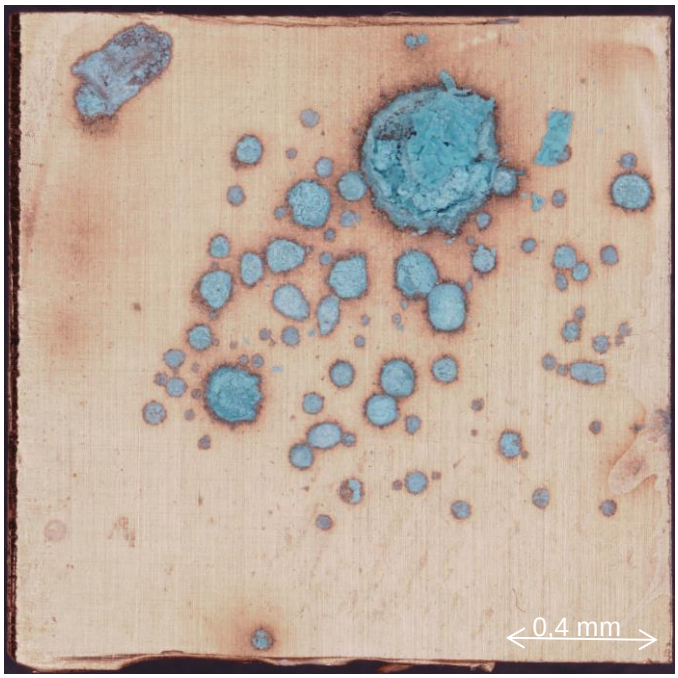

Fig. 4.4.1 : NH_4NO_3 “dry” at t3, image recorded at the HIROX 3D microscope

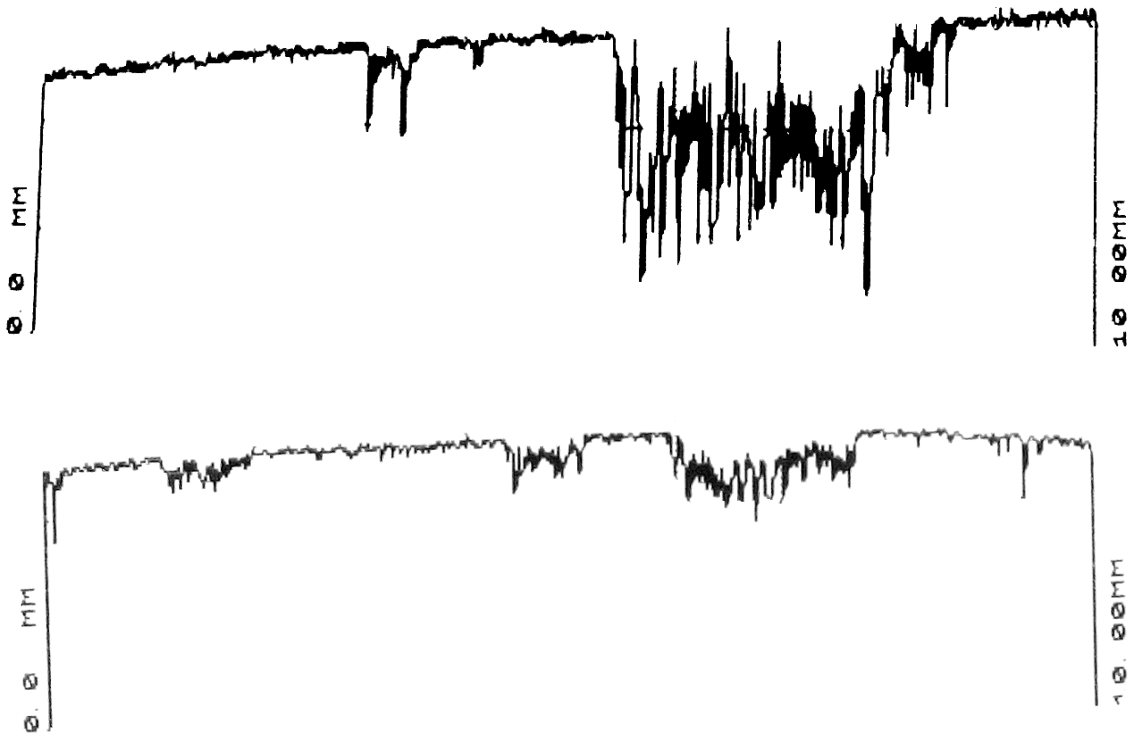

Fig. 4.4.2: Profiles associated with a) NH_4NO_3 “dry” , b) NaCl “dry” after pickling

5 Conclusions

The accelerated aging cycle and procedure that was planned and tested allowed to check periodically the evolution of the samples in terms of different parameters (colorimetry, morphology of residues, mineralogical phases) and to simulate outdoor exposures taking into account T, RH and aerosol composition in the Rimini zone. Two modalities of deposition ("wet" and "dry") of synthetic PM were set, both with their peculiar advantages and disadvantages. Using the "wet" deposition mode, the salts react rapidly with the substrate forming corrosion products typical of long periods of time, in the months and years ranges, while the "dry" deposition allows to better investigate the initial states of bronzes that interact with PM. Moreover, the "dry" deposition mode provides also easier residues to remove from the bronze substrate, allowing the analysis of the bronze under the corrosion products before pickling; in all the specimens, below the corrosion products, cuprite was found. Viceversa, the "wet" deposition mode offers adherent patinas homogeneously distributed. It was observed that localized corrosion, in the form of pitting, was better simulated using the "dry" deposition mode, although even using the "wet" deposition mode it could be observed, but at further stages of ageing.

The usage of single salts on different specimens has allowed to follow the evolution of corrosion products that were promoted by each salt. In addition to cuprite, at the end of the ageing NaCl "dry" produced mainly atacamite, while NaCl "wet" malachite, that is rarely found on outdoor exposed bronzes and which is not easily simulated in other "wet&dry" experiments. Nitrates resulted the compounds that reacted less with the substrate, except for the initial formation of Pb nitrates, which are uncommonly encountered on patinas because of their high solubility. The ammonium cation plays a role in the formation of products as gerhardite (found on samples treated with NH_4NO_3) and antlerite (found on samples treated with $(NH_4)_2SO_4$), while sodium salts do not induce the formation of such phases. Sulphates hydrate themselves during the ageing and form, after three weeks, brochantite in case of Na_2SO_4 "dry" and "wet" specimens, posnjakite and antlerite in case of $(NH_4)_2SO_4$ "wet" and brochantite and antlerite in case of $(NH_4)_2SO_4$ "dry".

Thanks to the previous studies on samples treated with single salts, it was possible to interpret more complex systems: ternary mixtures of salts spread in a “wet” manner did not allow the observation of further corrosion products than hydrocerussite, while the “dry” deposition modality slowed down the process of reaction and allowed to investigate the phases evolution over time; sulphates were found to be more prone to react against the substrate than the other salts, especially the nitrates, whose behaviour confirmed theoretical data evaluated by means of the E-AIM model.

The formulation of a matrix containing organics, minerals and carbon allowed to estimate the salts effect variations in a realistic PM mixture and to recognize the contribution of the single component by comparison with previous cases. In particular, it was observed that nitrates and sulphates tended to recrystallize together after deliquescence, while chlorides recrystallized preferentially by their own, somehow similarly to what was observed on the sample treated with a ternary mixture of salts in “dry” mode. Even though phases identification by Raman was difficult because of the fluorescence related to the spread organic fraction, macroscopically it was possible to retrieve greenish residues on the sample containing soluble salts in addition to the matrix, while no similar residues were encountered on the sample where the matrix only was deposited: according to results obtained by the “dry” specimen treated with salts only, these modifications were associated to the reaction of the salts with the substrate and to the formation of corrosion products; similar features were observed onto the sample treated with natural PM. In order to better establish the identity of the formed products and their evolution, further studies will be needed, possibly involving an extension of the accelerated ageing period.

The methodology for the preparation of artificial PM and the accelerated aging cycles performance that was established results to be promising to simulate years of exposure in an outdoor environment for bronze manufacts. In addition to contributions to the theoretical understanding of corrosion mechanisms and patinas evolutions, these studies on accelerated ageing methodologies can provide a useful contribution to develop new materials or effective conservation strategies (e.g. by testing protective coatings) to prevent cultural heritage from damages related to atmospheric particulate matter.

6 Legend

AAS	Atomic Absorption Spectroscopy
ATR-FTIR	Attenuated Total Reflectance – Fourier Transform InfraRed
BSE	Backscattered Electrons
CCD	Charge-Coupled Device
DTGS	Deuterium TryGlicine Sulphate
DRH	Deliquescence Relative Humidity
EDL	Electrodeless Discharge Lamps
EPA	Environmental Protection Agency
F	Flame
GF	Graphite Furnace
HDL	Hollow cathode Discharge Lamps
HDPE	High Density PolyEthylene
IUPAC	International Union of Pure and Applied Chemistry
PM	Particulate Matter
RH	Relative Humidity
SE	Secondary electrons
SEM-EDX	Scanning Electron Microscopy – Energy Dispersive X-rays
TSP	Total Suspended Particulate

7 Bibliography

[1] Dillmann, Philippe, et al., eds. *Corrosion and conservation of cultural heritage metallic artefacts*. Elsevier, 2013.

[2] Syed, S. "Atmospheric corrosion of materials." *Emirates Journal for Engineering Research* 11.1 (2006): 1-24.

[3] Dorsen, L. *The Classic Little Mermaid- Hans Christian Andersen*, <http://mermaidnews.net/den-lille-havfrue-hans-christian-andersen/>, [last consultation on 2018-05-14]

[4] Tzanis, C., et al. "Nitric acid and particulate matter measurements at Athens, Greece, in connection with corrosion studies." *Atmospheric Chemistry and Physics* 9.21 (2009): 8309-8316.

[5] Ferm, Martin, et al. "Deposition measurement of particulate matter in connection with corrosion studies." *Analytical and Bioanalytical Chemistry* 384.6 (2006): 1320-1330.

[6] Bassini, Serena. *Bronzi e bronzi dorati esposti all'azione della pioggia: corrosione ed inibizione*. PhD Thesis.

[7] Charola, A. Elena. "Salts in the deterioration of porous materials: an overview." *Journal of the American institute for conservation* 39.3 (2000): 327-343.

[8] Chiavari, C.; Bernardi, E.; Ospitali, F.; Robbiola, L.; Martini, C.; Morselli, L. "Monumenti in bronzo: prove di invecchiamento artificiale." *La metallurgia italiana* (May 2009): 45-54.

[9] De la Fuente, D., et al. "City scale assessment model for air pollution effects on the cultural heritage." *Atmospheric environment* 45.6 (2011): 1242-1250.

[10] Camuffo, Dario. *Microclimate for cultural heritage: conservation, restoration, and maintenance of indoor and outdoor monuments*. Elsevier, 2013.

[11] Rodriguez-Navarro, C. et al. “Role of particulate matter from vehicle exhaust on porous building stones (limestone) sulfation” (1996)

[12] McNaught, Alan D., and Alan D. McNaught. *Compendium of chemical terminology*. Vol. 1669. Oxford: Blackwell Science, 1997.

[13] Birleanu, Corina, et al. "Relative humidity effect on pull-off forces in MEMS flexible structures measured by AFM." *Design, Test, Integration and Packaging of MEMS/MOEMS (DTIP), 2017 Symposium on*. IEEE, 2017.

[14] F. Mazza, G. Bianchi, *Corrosione e protezione dei metalli*, AIM (2000).

[15] Van Grieken, Rene, and Koen Janssens, eds. *Cultural heritage conservation and environmental impact assessment by non-destructive testing and micro-analysis*. CRC Press, 2014.

[16] Kucera, Vladimir. "The effect of acidification on corrosion of structures and cultural property." *Acidification in tropical countries*. John Wiley & Sons, 1988. 167-194.

[17] C. Leygraf, T. Graedel, *Atmospheric Corrosion*, Wiley Interscience, New York (2000).

[18] T. E. Graedel, K. Nassau, J. P. Franey, *Copper patinas formed in the atmosphere 1: an Introduction*, Corrosion Science 27 (1987) 639-657.

[19] Nassau, K; Gallagher, P. K; Graedel, T. E. (1987). The characterization of patina components by X-ray diffraction and evolved gas analysis. Corrosion Science, Vol. 44, pp. 425 – 450

[20] D. De la Fuente, J. Simancas, M. Morcillo (2008). Morphological study of 16-year patinas formed on copper in a wide range of atmospheric exposures. Corrosion Science, Vol. 50, pp. 268 – 285.

[21] A. Krätschmer, I. Odnevall Wallinder, C. Leygraf (2002). The evolution of outdoor copper patina. Corrosion Science, Vol. 44, pp. 425 – 450.

[22] Gouda, V. K., G. I. Youssef, and N. A. Abdel Ghany. "Characterization of Egyptian bronze archaeological artifacts." *Surface and Interface Analysis* 44.10 (2012): 1338-1345.

[23] Rapp, George. *Archaeomineralogy*. Springer Science & Business Media, 2009.

[24] Ospitali, F., Chiavari, C., Martini, C., Bernardi, E., Passarini, F., & Robbiola, L. (2012). The characterization of Sn-based corrosion products in ancient bronzes: a Raman approach. *Journal of Raman Spectroscopy*, *43*(11), 1596-1603.

[25] Santana, J. J., et al. "Characterization of the corrosion products formed on zinc in archipelagic subtropical environments." *Int. J. Electrochem. Sci* 7 (2012): 12730-12741.

[26] US Environmental Protection Agency. “Particulate Matter (PM) Pollution”, <https://www.epa.gov/pm-pollution>, [last consultation on 2018-05-30]

[27] Grau-Bové, Josep, and Matija Strlič. "Fine particulate matter in indoor cultural heritage: a literature review." *Heritage science* 1.1 (2013): 8.

[28] Seinfeld, John H., and Spyros N. Pandis. *Atmospheric chemistry and physics: from air pollution to climate change*. John Wiley & Sons, 2016.

[29] Muhlfeld, Christian, et al. "Interactions of nanoparticles with pulmonary structures and cellular responses." *American Journal of Physiology-Lung Cellular and Molecular Physiology* 294.5 (2008): L817-L829.

[30] Morales, H. “Atmospheric corrosion of quaternary bronzes (Cu-Sn-Zn-Pb): Laboratory tests (accelerated ageing in wet & dry conditions) and field studies (the Bottego monument in Parma, Italy)”. Master Thesis.

[31] Whalley, Jacqueline, and Sara Zandi. "Particulate Matter Sampling Techniques and Data Modelling Methods." *Air Quality-Measurement and Modeling*. InTech, 2016.

[32] Wilson, Michael Lee, et al. "APTI course 435, Atmospheric Sampling. Student Manual." (1980), chapter 5.

[33] Epa, N. S. W. "Approved methods for the sampling and analysis of air pollutants in New South Wales." (2000).

[34] Raffo, S; Nobili, L; Guenoden, L; Bernardi, E; Vassura, I; Ferrero, L; Bolzacchini, E. “Particulate matter and material decay: analysis of dry deposition on horizontal and vertical surfaces exposed through the *Deposition Box* system”.

[35] Marco Casati, M. “ Interactions between atmospheric particulate matter and stone surfaces by means of laboratory and in field studies”**.** PhD thesis.

[36] Laura Guenoden, L. “PM and material decay: Analysis of dry depositions on horizontal and vertical surrogate surfaces through a Deposition Box system”. Master Thesis.

[37] Spurny, Kvetoslav R., ed. *Aerosol chemical processes in the environment*. CRC Press, 2000.

[38] Baietti, F. “Messa a punto di un metodo di deposizione accelerata di particolato atmosferico su provini metallici per studi di corrosione”. Bachelor Thesis.

[39] Sleiman, Mohamad, et al. "Soiling of building envelope surfaces and its effect on solar reflectance–Part II: Development of an accelerated aging method for roofing materials." *Solar Energy Materials and Solar Cells* 122 (2014): 271-281.

[40] Chang, Tingru, et al. "The golden alloy Cu5Zn5Al1Sn: Patina evolution in chloride-containing atmospheres." *Corrosion Science* 133 (2018): 190-203.

[41] Chan, Hak-Kim. "Dry powder aerosol delivery systems: current and future research directions." *Journal of aerosol medicine* 19.1 (2006): 21-27.

[42] Rolin, T. D., et al. "Salt Spray Test to Determine Galvanic Corrosion Levels of Electroless Nickel Connectors Mounted on an Aluminum Bracket." (2014).

[43] UNI – Ente italiano di normazione. *EN ISO 9227:2017*, <http://store.uni.com/catalogo/index.php/uni-en-iso-9227-2017.html?josso_back_to=http://store.uni.com/josso-security-check.php&josso_cmd=login_optional&josso_partnerapp_host=store.uni.com>, [last consultation on 2018-06-08]

[44] International Organisation of Standardization. *ISO 17752:2012*, <https://www.iso.org/standard/53503.html>, [last consultation on 2018-06-08]

[45] Wallinder, Inger Odnevall, et al. "Corrosion and runoff rates of Cu and three Cu-alloys in marine environments with increasing chloride deposition rate." *Science of the Total Environment* 472 (2014): 681-694.

[46] Cordier, Marie. *Outdoor bronze conservation: assessment of protective treatments by accelerated aging and of treatment removal procedures by laser cleaning*. Diss.

[47] Ghali, Edward. *Corrosion resistance of aluminum and magnesium alloys: understanding, performance, and testing*. Vol. 12. John Wiley & Sons, 2010.

[48] Buccolieri, Giovanni, et al. "Portable EDXRF investigation of the patinas on the Riace Bronzes." *Nuclear Instruments and Methods in Physics Research Section B: Beam Interactions with Materials and Atoms* 343 (2015): 101-109.

[49] Ascott. *Corrosion Testing Standards*, <https://www.ascott-analytical.com/test_standard/iso-6270-2-ch/>, [last consultation on 2018-06-08]

[50] International Organisation of Standardization. *ISO 11507:2007,* <https://www.iso.org/standard/37489.html>, [last consultation on 2018-06-08]

[51] Sutter, Florian et al. “Life time analysis and accelerated aging tests”. *SFERA* (2013)

[52] Ferrari, Angelo. *PROCEEDINGS 4th International Congress on “Science and Technology for the Safeguard of Cultural Heritage in the Mediterranean Basin” VOL. I*. Angelo Ferrari.

[53] Chiavari, C., Bernardi, E., Martini, C., Passarini, F., Ospitali, F., & Robbiola, L. (2010). The atmospheric corrosion of quaternary bronzes: the action of stagnant rain water. *Corrosion Science*, *52*(9), 3002-3010.

[54] Clegg, L. S; Brimblecombe, P. Extended AIM Aerosol Thermodynamics Model <http://www.aim.env.uea.ac.uk/aim/aim.php>, [last consultation on 2018-06-02]

[55] S. L. Clegg, M. J. Kleeman, R. J. Griffin, and J. H. Seinfeld (2007) Effects of uncertainties in the thermodynamic properties of aerosol components in an air quality model - Part I: Treatment of inorganic electrolytes and organic compounds in the condensed phase. *Atmos. Chem. Phys.* **8**, 1057-1085.

[56] S. L. Clegg, K. S. Pitzer and P. Brimblecombe (1992) Thermodynamics of multicomponent, miscible, ionic solutions. II. Mixtures including unsymmetrical electrolytes. *J. Phys. Chem.* 96, 9470-9479; 1994, 98, 1368; 1995, 99, 6755.

[57] Tang, Ignatius N., and Harry R. Munkelwitz. "Composition and temperature dependence of the deliquescence properties of hygroscopic aerosols." *Atmospheric Environment. Part A. General Topics* 27.4 (1993): 467-473.

[58] MMM Group. “Climacell 111, cooling incubator with controlled humidity – Instructions for use” (2015).

[59] Arpae Emilia Romagna, <https://www.arpae.it/>, [last consultation on 2018-07-01]

[60] C. Chiavari, A. Balbo, E. Bernardi, C. Martini, M. C. Bignozzi, M. Abbottoni, and C. Monticelli, *Protective silane treatment for patinated bronze exposed to simulated natural environments*, Mater. Chem. Phys., 2013, vol. 141, no. 1, pp. 502–511.

[61] Schanda, János, ed. *Colorimetry: understanding the CIE system*. John Wiley & Sons, 2007.

[62] Figure from: Singh, Babita, D. V. Parwate, and S. K. Shukla. "Radiosterilization of fluoroquinolones and cephalosporins: Assessment of radiation damage on antibiotics by changes in optical property and colorimetric parameters." *AAPS PharmSciTech* 10.1 (2009): 34-43.

[63] AZO Materials <https://www.azom.com/article.aspx?ArticleID=14791>, [last consultation on 2018-06-12]

[64] Figure from: Perissi, Ilaria. (2009). Study of Ionic Liquids as innovative fluids in Material Science applications.. 10.13140/RG.2.1.4501.9288.

[65] Colthup, Norman. *Introduction to infrared and Raman spectroscopy*. Elsevier, 2012.

[66] Figure from: Raman Spectroscopy (Wikipedia) < https://en.wikipedia.org/wiki/Raman_spectroscopy>, [last consultation on 2018-06-11]

[67] L. Nasdala, D.C. Smith, R. Kaindl, M.A. Ziemann (2004). EMU notes in mineralogy, Vol. 6, Chapter 7, p. 286.

[68] Figure from: The Raman Spectrophotometer, <https://www.sas.upenn.edu/~crulli/TheRamanSpectrophotometer.html>, [last consultation on 2018-06-11]

[69] Glassford, Stefanie E., Bernadette Byrne, and Sergei G. Kazarian. "Recent applications of ATR FTIR spectroscopy and imaging to proteins." *Biochimica et Biophysica Acta (BBA)-Proteins and Proteomics* 1834.12 (2013): 2849-2858.

[70] Figure from: Ausili, Alessio, Marina Sánchez, and Juan C. Gómez-Fernández. "Attenuated total reflectance infrared spectroscopy: A powerful method for the simultaneous study of structure and spatial orientation of lipids and membrane proteins." *Biomedical Spectroscopy and Imaging* 4.2 (2015): 159-170.

[71] Poon, Chin Y., and Bharat Bhushan. "Comparison of surface roughness measurements by stylus profiler, AFM and non-contact optical profiler." *Wear* 190.1 (1995): 76-88.

[72] Chappard, D., et al. "Image analysis measurements of roughness by texture and fractal analysis correlate with contact profilometry." *Biomaterials* 24.8 (2003): 1399-1407.

[73] Welz, Bernhard. *Atomic absorption spectroscopy*. Verlag Chemie., 1976.

[74] Bhanot, D. “Introduction to AAS component parts”, <http://lab-training.com/2013/05/08/introduction-to-aas-component-parts/>, [last consultation on 2018-05-15]

[75] Yang, Lietai, Roberto T. Pabalan, and Miriam R. Juckett. "Deliquescence relative humidity measurements using an electrical conductivity method." *Journal of Solution Chemistry* 35.4 (2006): 583-604.

[76] Supporting information to the following article: Debbichi, L., et al. "Vibrational properties of CuO and Cu4O3 from first-principles calculations, and Raman and infrared spectroscopy." *The Journal of Physical Chemistry C* 116.18 (2012): 10232-10237.

[77] Aibéo, Cristina L., et al. "Micro-Raman analysis for the identification of pigments from 19th and 20th century paintings." *Journal of Raman Spectroscopy: An International Journal for Original Work in all Aspects of Raman Spectroscopy, Including Higher Order Processes, and also Brillouin and Rayleigh Scattering* 39.8 (2008): 1091-1098.

[78] Kaminskii, Alexander A., et al. "Cerussite, PbCO3–a new Stimulated Raman Scattering (SRS)-active crystal with high-order Stokes and anti-Stokes lasing." *Laser & Photonics Reviews* 7.3 (2013): 425-431.

[79] Brooker, Murray H., et al. "Infrared and Raman spectra and X-ray diffraction studies of solid lead (II) carbonates." *Canadian Journal of Chemistry* 61.3 (1983): 494-502.

[80] Canepa, Pieremanuele, Piero Ugliengo, and Maria Alfredsson. "Elastic and Vibrational Properties of α-and β-PbO." *The Journal of Physical Chemistry C* 116.40 (2012): 21514-21522.

[81] Martens, Wayde, Ray L. Frost, and Peter A. Williams. "Raman and infrared spectroscopic study of the basic copper chloride minerals–implications for the study of the copper and brass corrosion and." *Neues Jahrbuch für Mineralogie-Abhandlungen: Journal of Mineralogy and Geochemistry* 178.2 (2003): 197-215.

[82] Castro, Kepa, et al. "Noninvasive and nondestructive NMR, Raman and XRF analysis of a Blaeu coloured map from the seventeenth century." *Analytical and bioanalytical chemistry* 391.1 (2008): 433-441.

[83] Sunagawa, Ichiro. *Crystals: growth, mor*ph*ology, & perfection*. Cambridge University Press, 2005

[84] Scott, David A. *Copper and bronze in art: corrosion, colorants, conservation*. Getty publications, 2002.

[85] Dedera, Sebastian, et al. "On-line Raman spectroscopy of calcite and malachite during irradiation with swift heavy ions." *Nuclear Instruments and Methods in Physics Research Section B: Beam Interactions with Materials and Atoms* 365 (2015): 564-568.

[86] Rousseau, D. L., R. E. Miller, and G. E. Leroi. "Raman spectrum of crystalline sodium nitrate." *The Journal of Chemical Physics* 48.8 (1968): 3409-3413.

[87] Zaffino, Chiara, et al. "Exploiting external reflection FTIR spectroscopy for the in-situ identification of pigments and binders in illuminated manuscripts. Brochantite and posnjakite as a case study." *Spectrochimica Acta Part A: Molecular and Biomolecular Spectroscopy* 136 (2015): 1076-1085.

[88] Hamilton, Andrea, and Robert I. Menzies. "Raman spectra of mirabilite, Na2SO4· 10H2O and the rediscovered metastable heptahydrate, Na2SO4· 7H2O." *Journal of Raman Spectroscopy* 41.9 (2010): 1014-1020.

[89] Figure from: Wikipedia, “Brochantite” page < https://upload.wikimedia.org/wikipedia/commons/thumb/3/35/Brochantite-207226.jpg/260px-Brochantite-207226.jpg>, [last consultation on 2018-07-03]

[90] Kettle, S. "The Raman spectra of Phase III ammonium nitrate." *Air Force Office of Scientific Research (AFSC) USAF* (1982).

[91] Kosec, Tadeja, Polonca Ropret, and Andraž Legat. "Raman investigation of artificial patinas on recent bronze–part II: urban rain exposure." *Journal of Raman Spectroscopy* 43.11 (2012): 1587-1595.

[92] Ishizaka, Shoji, Kunihiro Yamauchi, and Noboru Kitamura. "In situ Quantification of ammonium sulfate in single aerosol droplets by means of laser trapping and Raman spectroscopy." *Analytical Sciences* 29.12 (2013): 1223-1226.

[93] Salt lake metals, <https://saltlakemetals.com/solubilityproducts/> [last consultation on 2018-07-04]

[94] Somasundaran, P., and Dianzuo Wang. *Solution chemistry: minerals and reagents*. Vol. 17. Elsevier, 2006.

[95] Dresselhaus, Mildred S., et al. "Raman spectroscopy of carbon nanotubes." *Physics reports* 409.2 (2005): 47-99.

[96] [<dateandtime.info>], [last consultation on 2017-10-25]

APPENDIX A

Plots of mean hourly Temperature and Relative Humidity at 2 m height from ground (Rimini Urbana station)

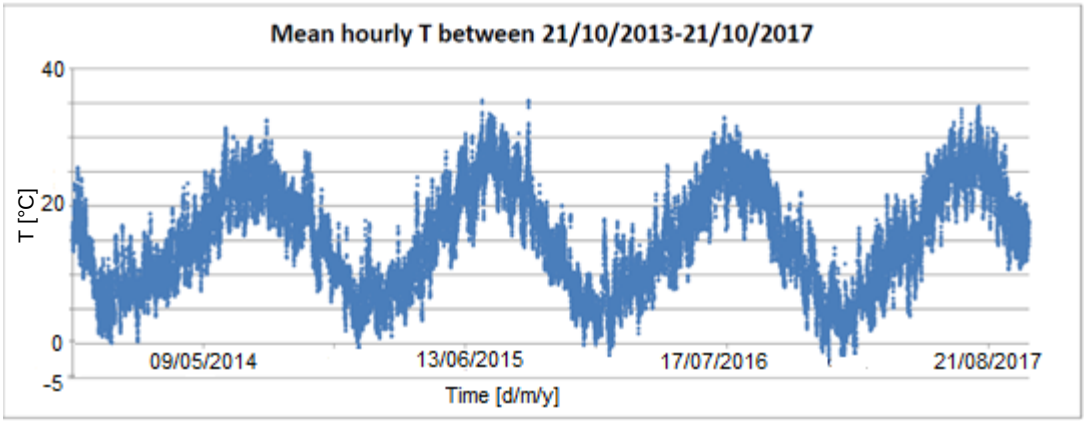

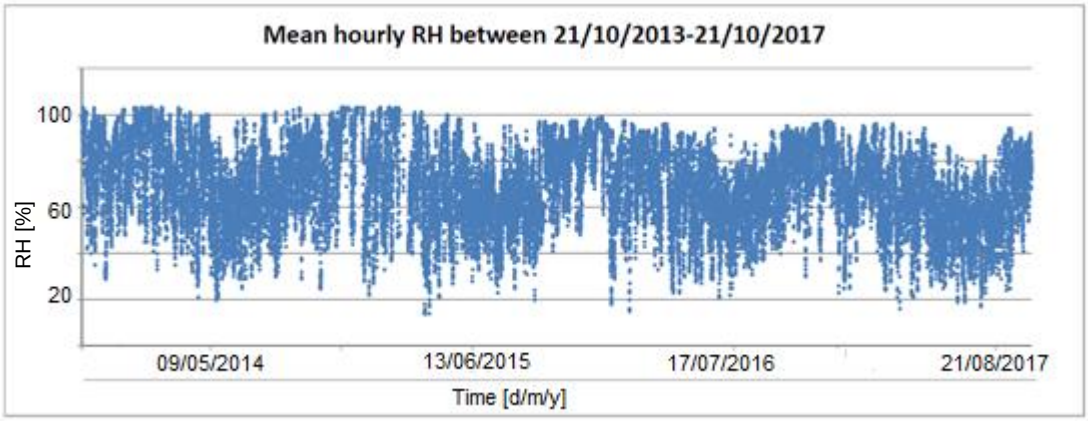

APPENDIX B

Plots of mean hourly Temperature at 2 m height from ground (Rimini Urbana station)

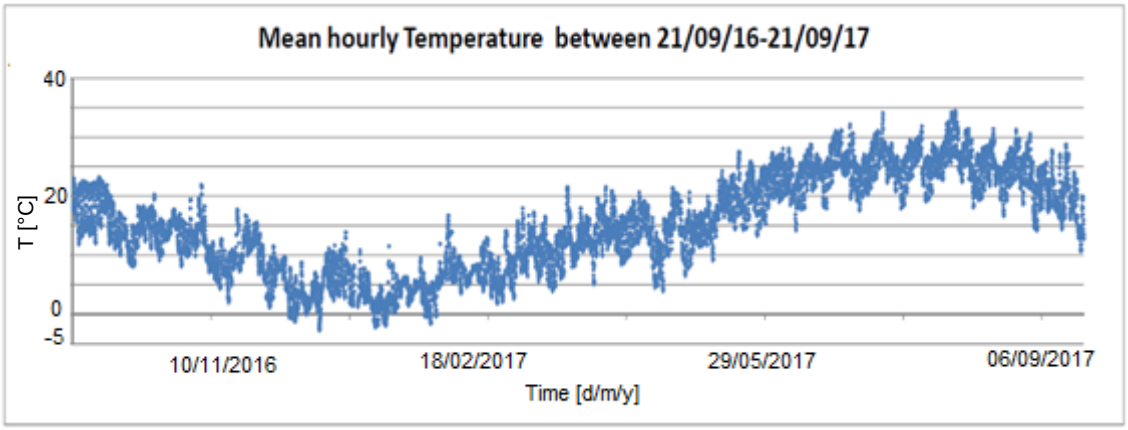

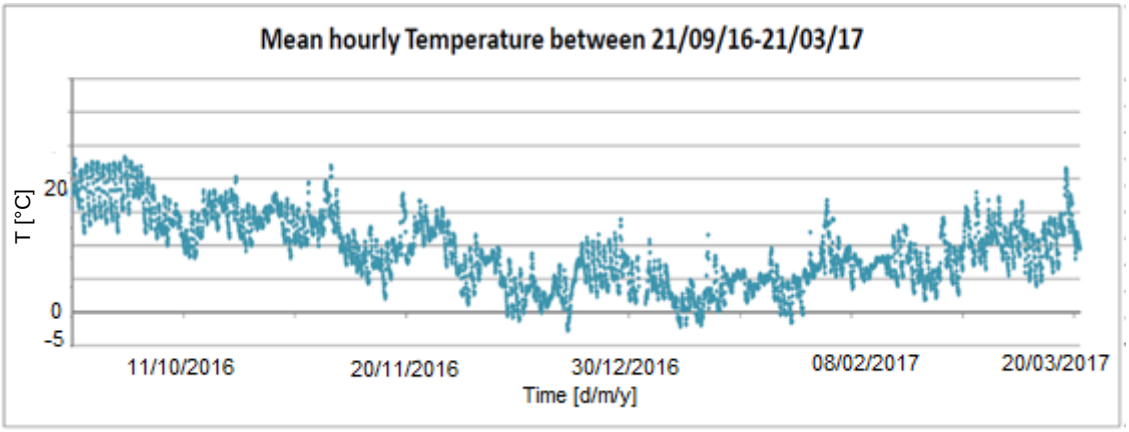

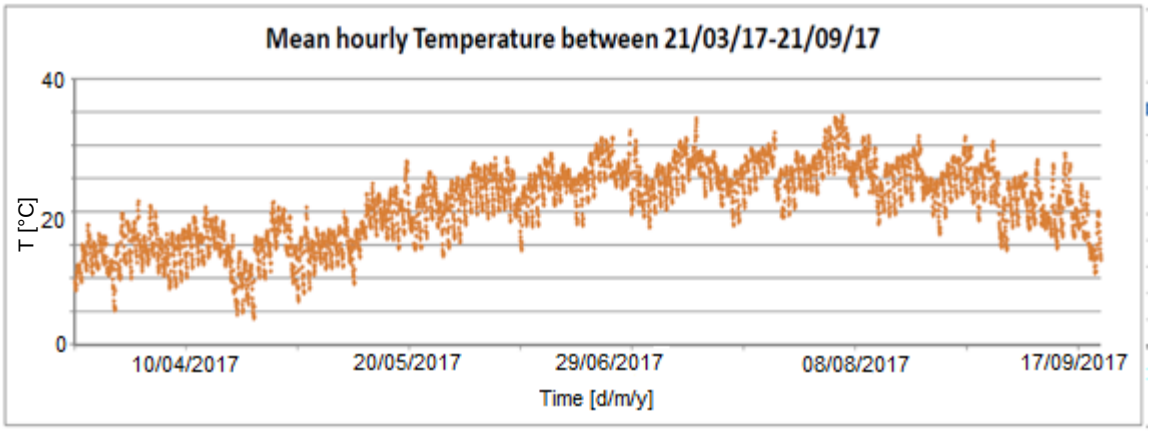

Plots of minimum hourly Temperature at 2 m height from ground (Rimini Urbana station)

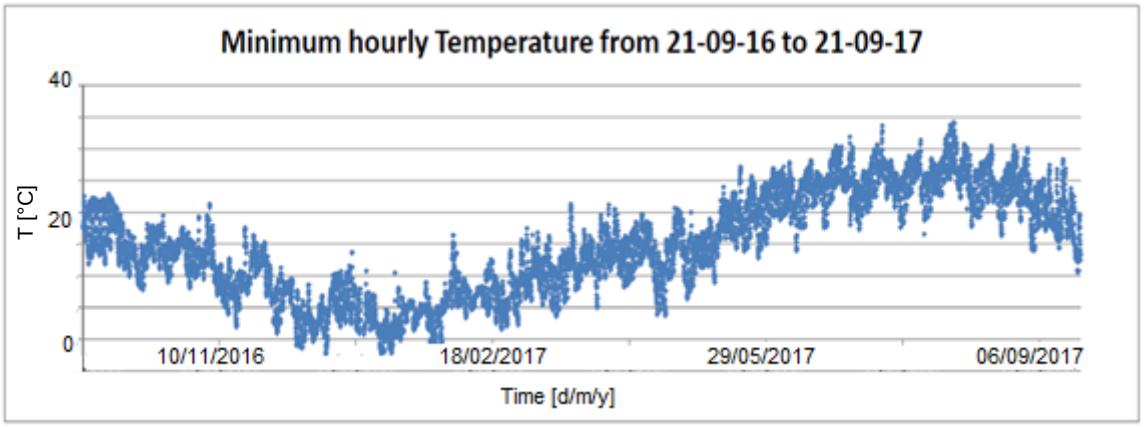

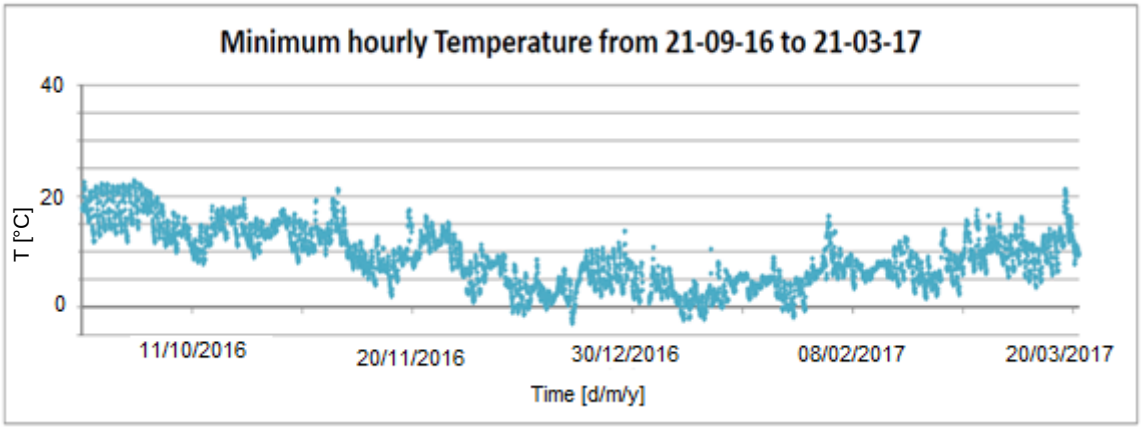

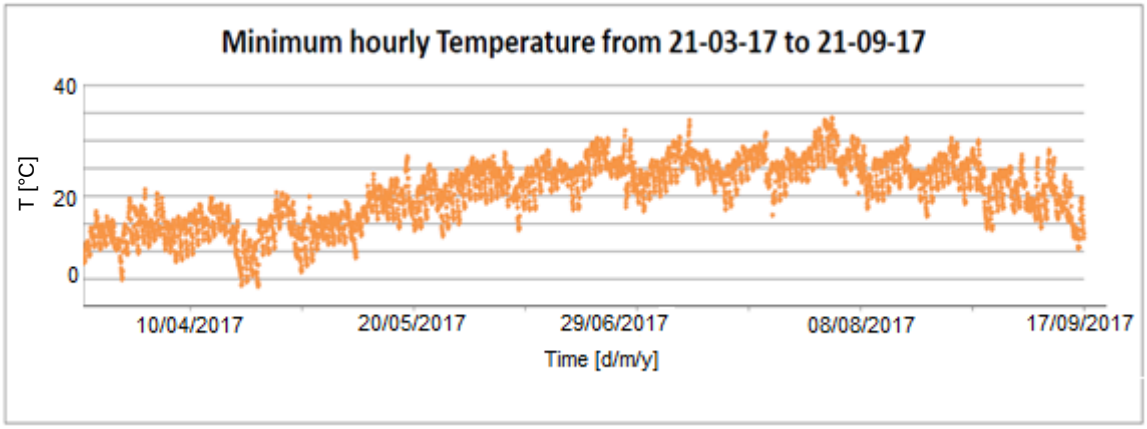

Plots of maximum hourly Temperature at 2 m height from ground (Rimini Urbana station)

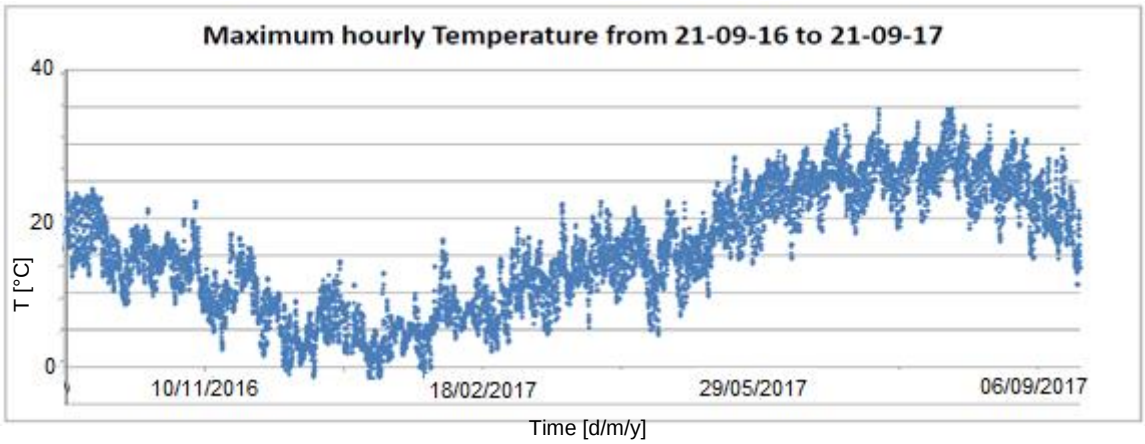

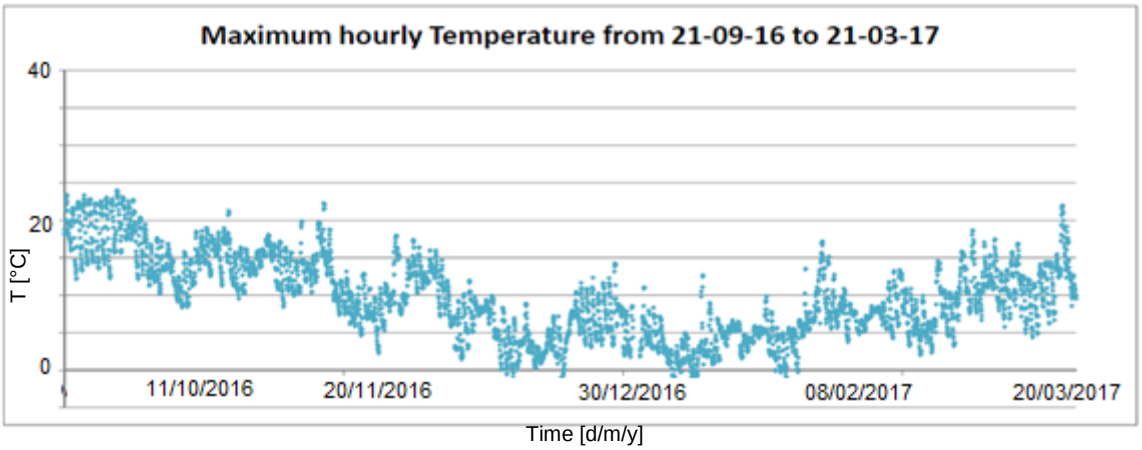

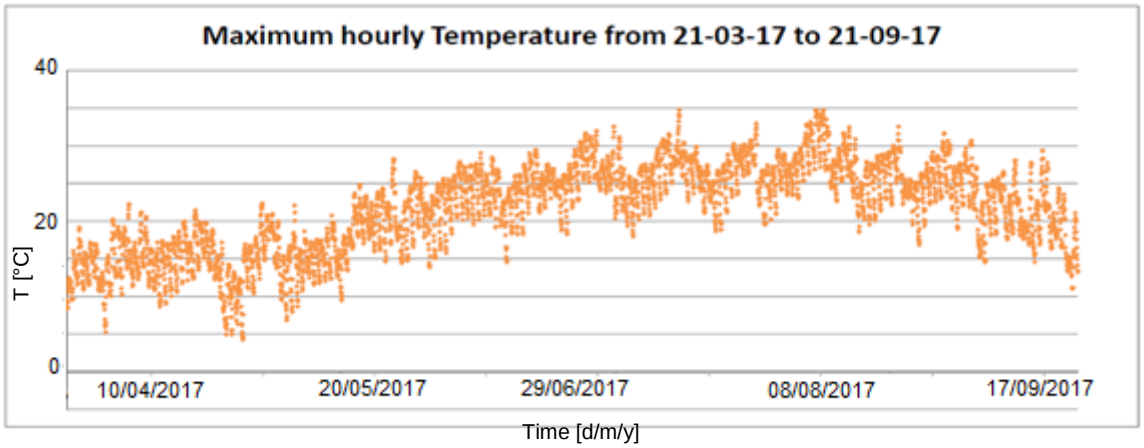

Plots of mean hourly Relative Humidity at 2 m height from ground (Rimini Urbana station)

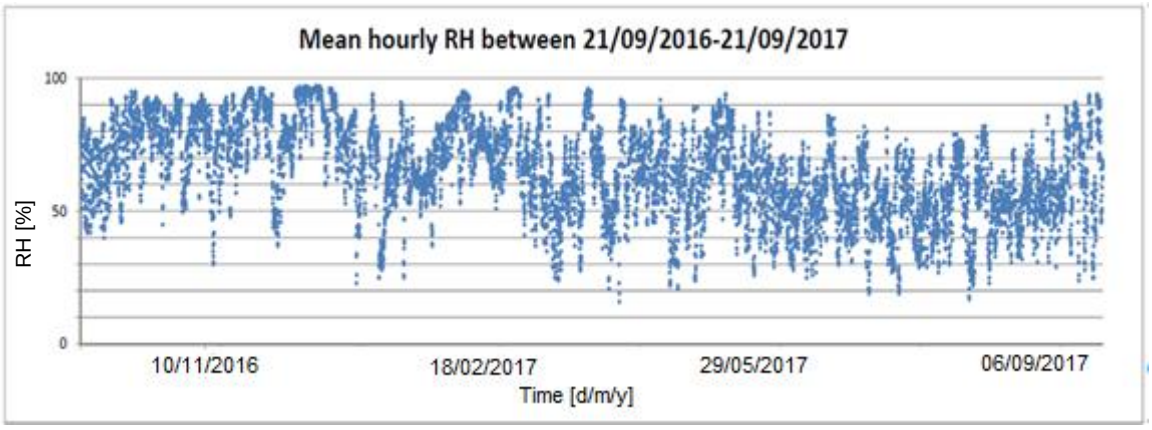

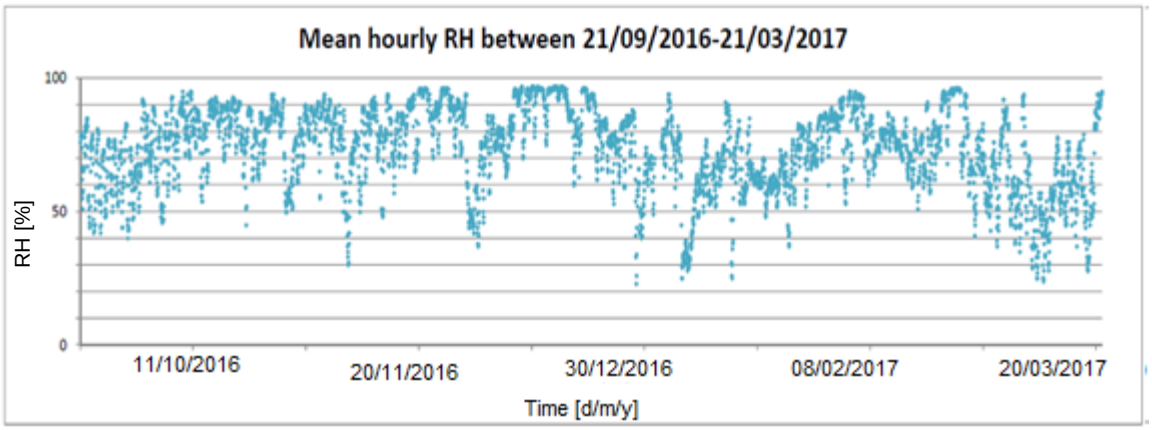

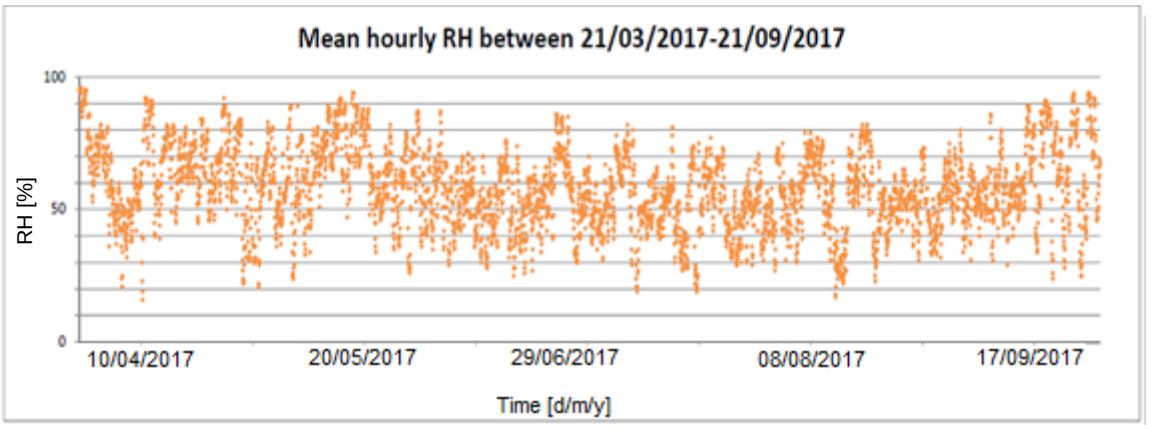

Plots of minimum hourly Relative Humidity at 2 m height from ground (Rimini Urbana station)

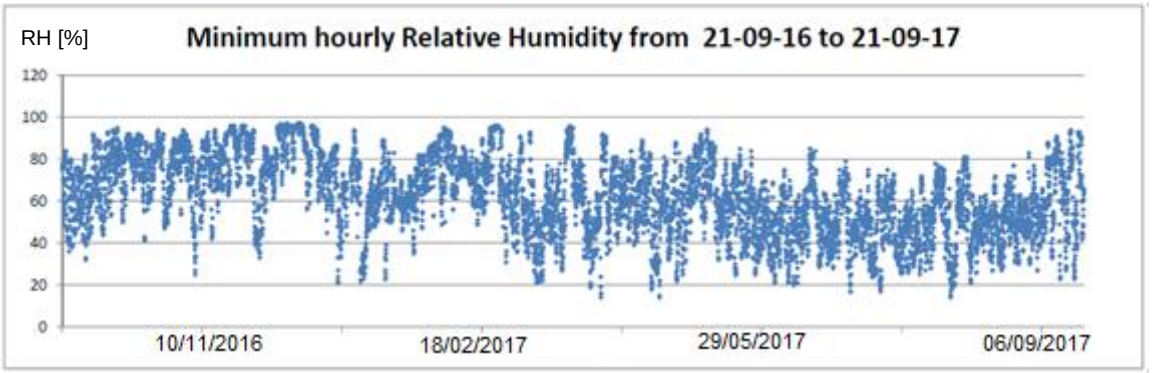

Time [d/m/y]

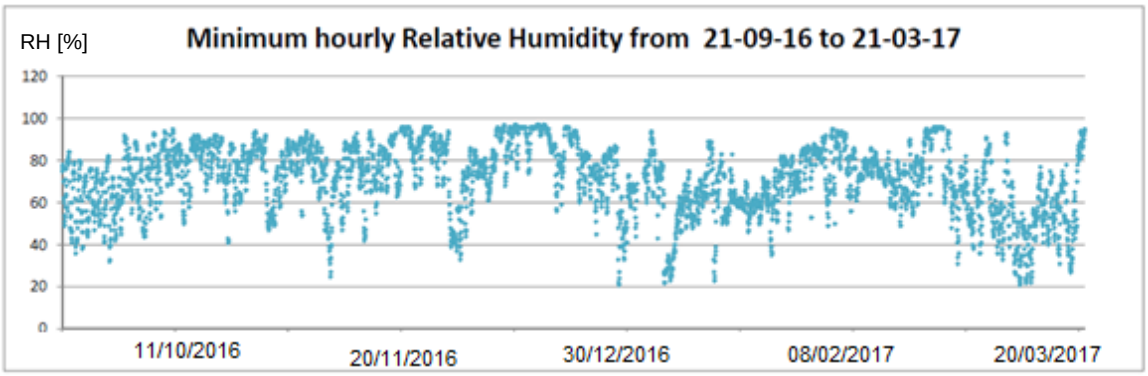

Time [d/m/y]

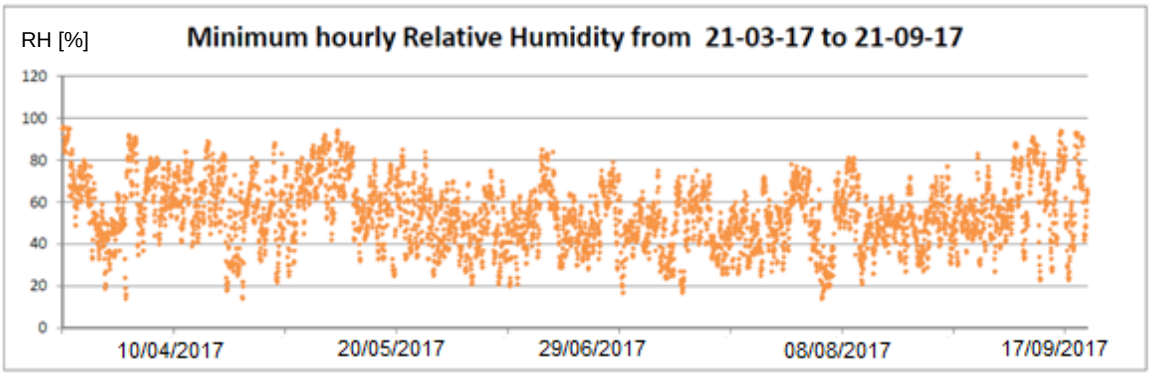

Time [d/m/y]

Plots of maximum hourly Relative Humidity at 2 m height from ground (Rimini Urbana station)

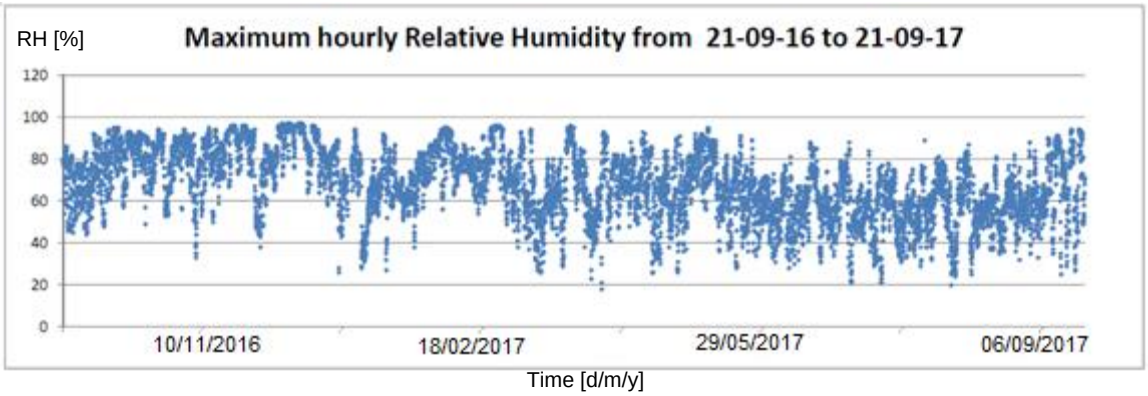

Time [d/m/y]

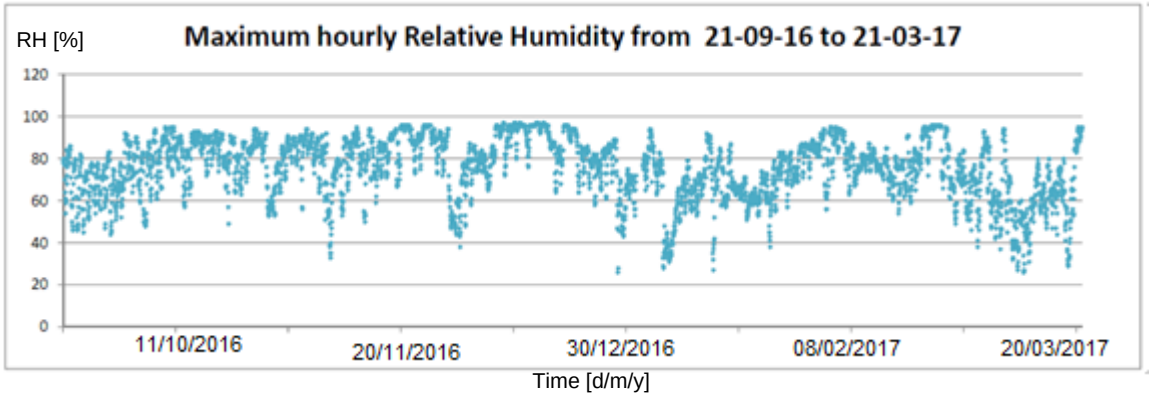

Time [d/m/y]

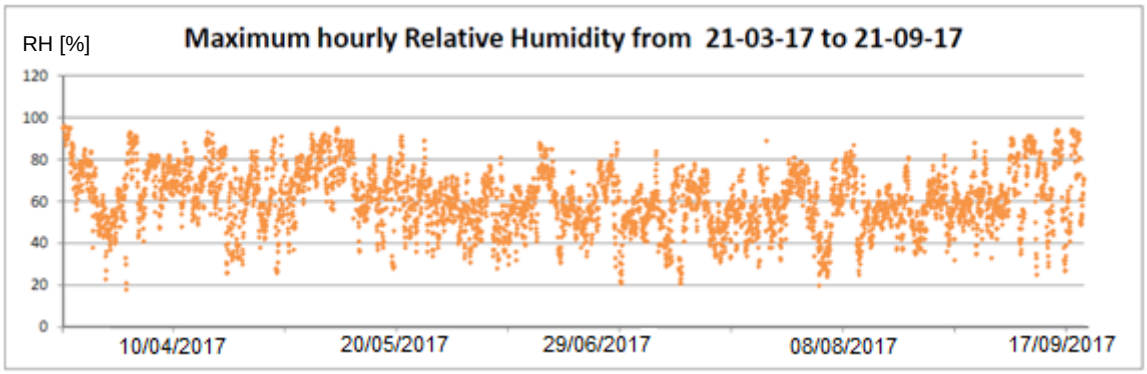

Time [d/m/y]

APPENDIX C

Plots of mean hourly Temperature and Relative Humidity at 2 m height from ground (RN Urbana station)

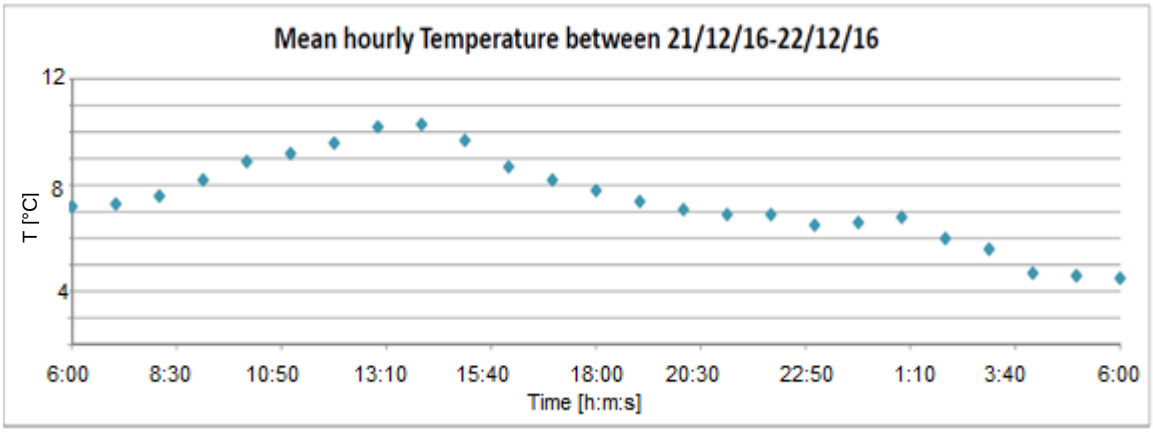

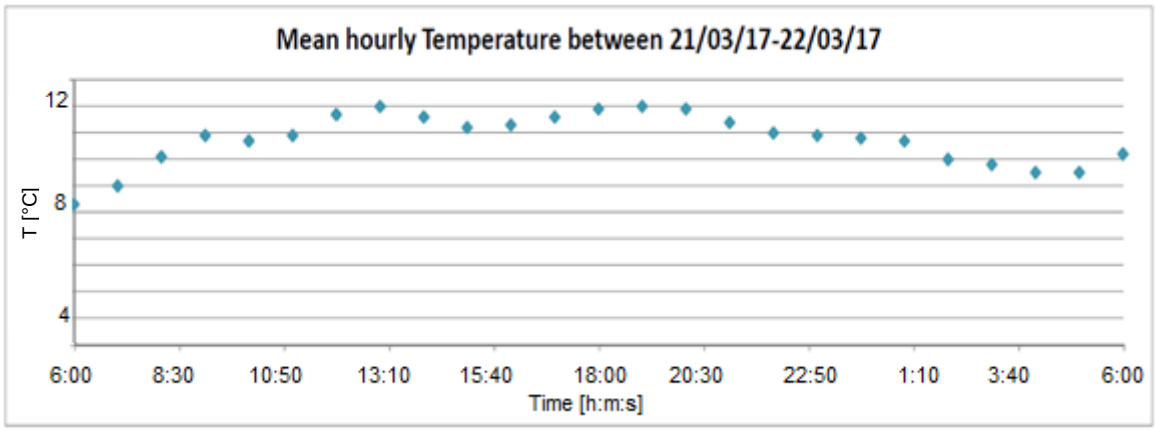

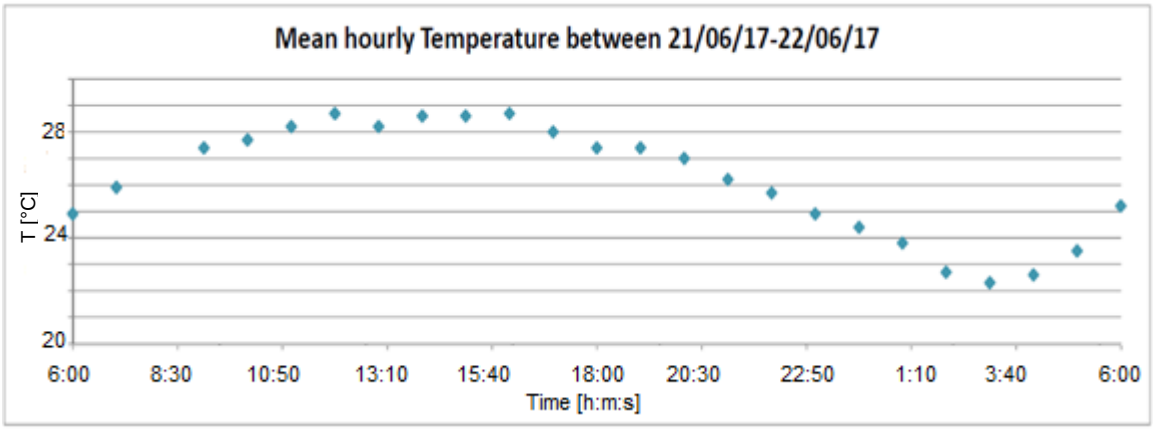

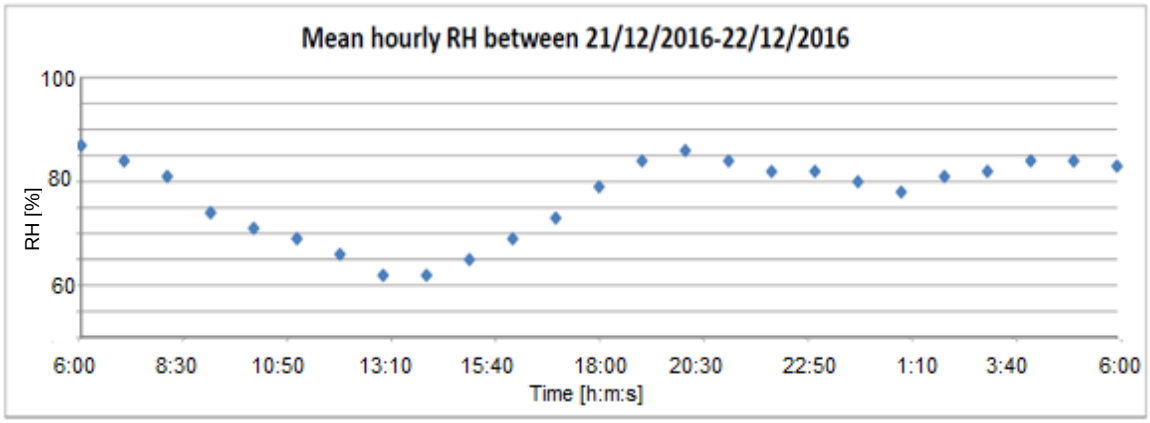
Mean hourly RH between 21/12/2016-22/12/2016
100
80
60
RH [%]
6:00
8:30
10:50
13:10
15:40
18:00
20:30
22:50
1:10
3:40
6:00
Time [h:m:s]

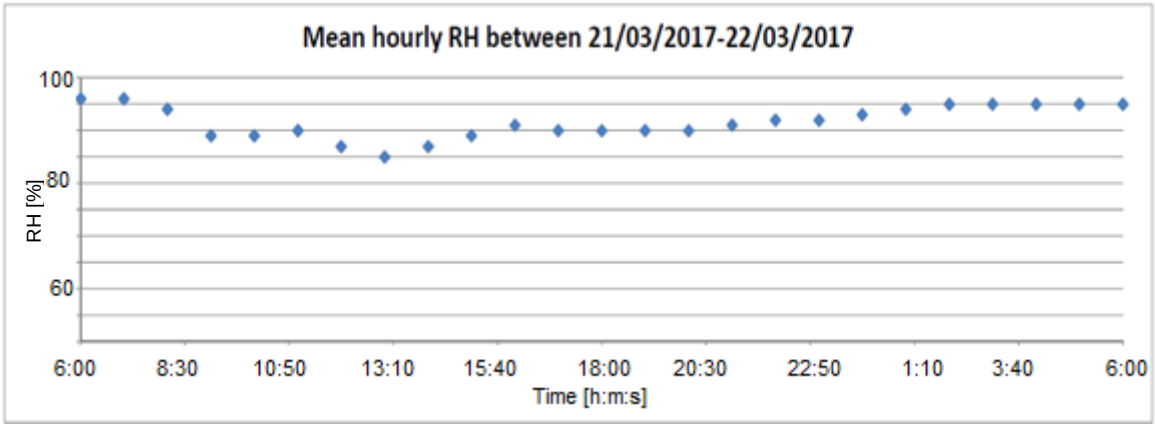
Mean hourly RH between 21/03/2017-22/03/2017
100
80
60
RH [%]
6:00
8:30
10:50
13:10
15:40
18:00
20:30
22:50
1:10
3:40
6:00
Time [h:m:s]

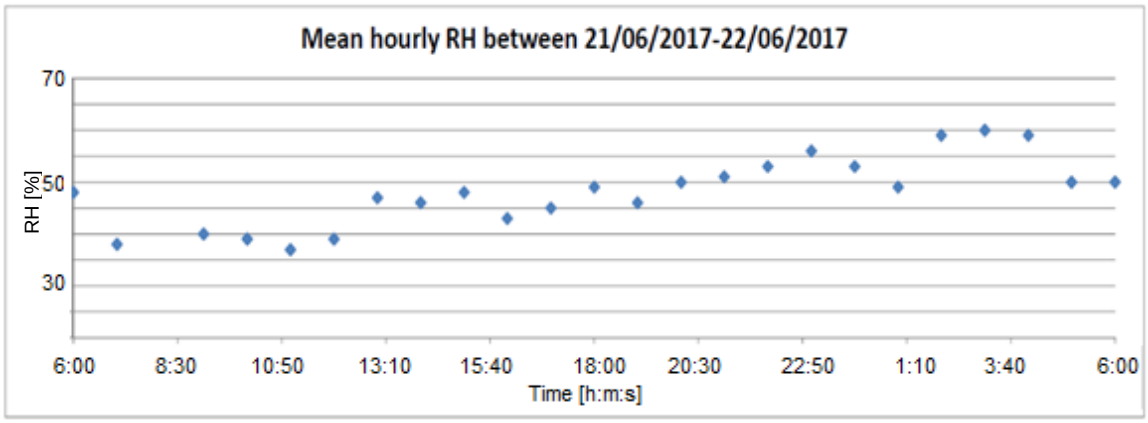
Mean hourly RH between 21/06/2017-22/06/2017
70
50
30
RH [%]
6:00
8:30
10:50
13:10
15:40
18:00
20:30
22:50
1:10
3:40
6:00
Time [h:m:s]

APPENDIX D

General cycle with frosting

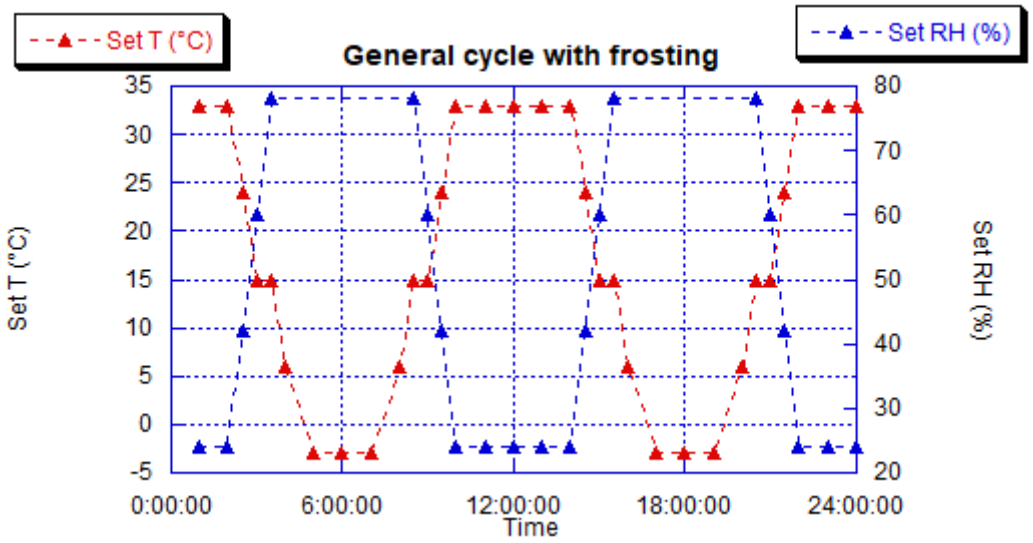

T and RH oscillations in the general cycle with frosting

- 2 h at T -3 °C, RH not controlled
- 1 h ramp to reach T 6 °C, RH not controlled
- 30 min ramp to reach T 15 °C, RH 78%
- 30 min at T 15 °C, to reach RH 60%
- 1 h ramp at T +9 °C / 30 min, RH -18% / 30 min
- 4 h at T 33 °C, RH 24%
- 1 h ramp at T -9 °C / 30 min, RH +18% / 30 min
- 30 min at T 15 °C, to reach RH 78%
- 30 min ramp to reach T 6°C, RH not controlled
- 1 h ramp to reach T -3 °C, RH not controlled
- Repetition of the cycle from the first step

Concerning light exposure, illumination can be performed using UVA lamps. For a general cycle, UVA lamps can be switched on for 6 h, corresponding to the raising T ramp and to the plateau of T max; then UVA lamps can be switched off for 6 h, corresponding to the decreasing T ramp and to the plateau of T min. These two steps have to be alternated in each cycle. Considerations on the influence of sunlight were done according to sunlight exposure data taken from the website “dateandtime.info”. The figure below illustrates briefly the duration of

daylight and night for San Marino in the current day (25/10/2017, dotted line), on the 21/06/2017 (red line) and on the 21/12/2017 (brown line) [96].

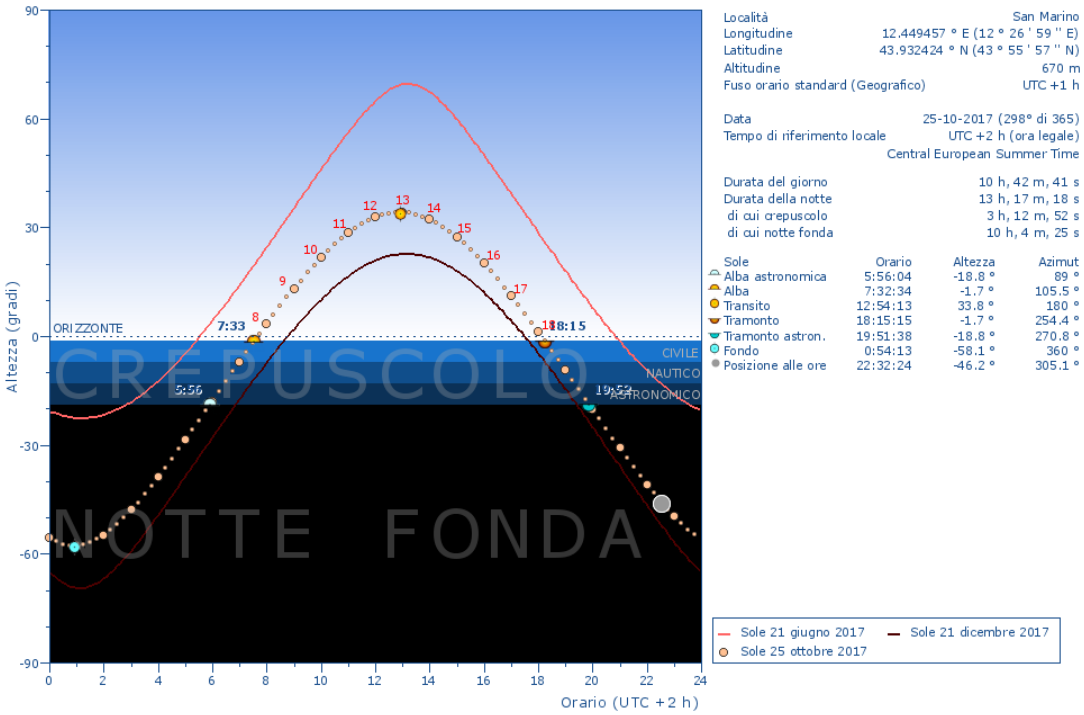

Daylight hours by dateandtime.info [96]

Acknowledgements

To my thesis supervisor Dr. Elena Bernardi and to her research group, for supporting me during this study and letting me discover further scientific topics I wish to keep on investigate.

To Dr. Francesca Ospitali, who has followed me during most of the analyses giving precious contributions to the outcome of this work.

To Prof. Martini and Prof. Chiavari, for their suggestions and their collaboration for these investigations.

To Dr. Elisa, for her support in the laboratories in Rimini.

To ASC teachers, who gave me hints on spectroscopies that allowed me to get more and more interested in understanding and applying them in my studies.

To Dr. Alessio Milanesi, who has encouraged me since I was abroad to do my best and who has given me one reason more to come back.

To all my family, who struggled but let me leave to join the ASC adventure all around Europe.